A GATE Monte Carlo dose analysis from Varian XI conebeam computed tomography

Luke Gilling

A thesis submitted in partial fulfilment of the requirements for the Degree of Master of Science in Medical Physics

Physics and Astronomy

University of Canterbury

New Zealand

May 2019

Abstract

Cone-beam computed tomography (CBCT) is a commonly used imaging technique in radiation therapy. Images are acquired prior to radiation therapy treatment to assess changes in patient anatomy and correct any errors in patient positioning. CBCT is an x-ray modality and its use for imaging includes a dose to the patient. This study aims to calculate the dose of ionizing radiation received during conebeam computed tomography (CBCT) imaging. Monte Carlo (MC) methods were used to perform these dose calculations. The CBCT scanner examined in this study was the Varian Truebeam X-ray Imager (XI). The present study is comprised of two main parts:

- Construction and validation of a MC model of a CBCT imager. The scanner was modelled using the GATE MC simulation toolkit. The results simulated by the model were compared with experimental measurements. Precise dose measurements were then made to convert the simulated dose into experimental dose for a given x-ray tube potential.

- Estimation of organ doses and effective dose in a human phantom. The GATE CBCT model was used to perform MC dose calculations in a population-based computational phantom. The absorbed dose calculations were converted into effective dose to evaluate the risk of developing secondary cancers due to CBCT imaging. Patient organ doses were analysed by dose-volume histograms (DVHs) and expressed using the minimum dose delivered to 50% and 10% of the organ volume, $D_{50\%}$ and $D_{10\%}$.

For the latter part of the study simulated and measured percentage depth doses (PDD) and profiles were compared. PDDs matched within 2% while profiles matched within 10%. Experimental measurements were performed in an anthropomorphic phantom using thermoluminiscent dosimeters (TLDs). Simulated and experimental results from the anthropomorphic phantom were compared to calculate an energy-specific MC calibration

factor. The average difference between simulated and experimental results was 13.7% for pelvis CBCT and 6.4% for head CBCT.

Effective doses were measured for the three main CBCT scan protocols: head and neck, thorax, and pelvis. The pelvis effective dose was the highest at 3.91 mSv ± 0.11 mSv. Thorax CBCT imaging, which uses an identical beam energy and geometry to pelvis imaging but lower mAs, had an effective dose of 1.72 mSv ± 0.07 mSv. Head CBCT imaging uses a lower beam energy and varying beam arrangement to the other sites. The effective dose for head CBCT was 0.289 mSv ± 0.020 mSv.

DVHs were evaluated for six different sites using the three main CBCT imaging protocols. The $D_{50\%}$ and $D_{10\%}$ were calculated for radiosensitive OARs. For pelvis CBCT imaging, centred on the prostate, the dose at the centre of the scan was 16.9 mGy. For selected radiosensitive organs the bladder ($D_{50\%}$=18.7 mGy, $D_{10\%}$=22.4 mGy), rectum ($D_{50\%}$=17.8 mGy, $D_{10\%}$=18.7 mGy) received the highest absorbed dose. For thorax CBCT imaging, centred in the mid-lung region, the centre dose was 5.1 mGy. For selected radiosensitive organs the heart ($D_{50\%}$=3.58 mGy, $D_{10\%}$=4.85 mGy) and lungs (right: $D_{50\%}$=3.89 mGy, $D_{10\%}$=5.27 ; left:$D_{50\%}$=2.22 mGy, $D_{10\%}$=3.59 mGy) received the highest absorbed dose. For head CBCT imaging, centred on the brain, the highest doses were received when the partial gantry rotation was through the anterior structures of the head. DVH analysis of the eyes showed $D_{50\%}$ was around 6 mGy while the $D_{50\%}$ of the brain and spinal cord were 2.45 mGy and 1.87 mGy.

The intention of this study was to provide dose detriment and treatment planning data for CBCT imaging using the XI scanner. The DVH data is intended to provide estimates to be used during radiation therapy treatment planning.

Acknowledgements

This project was made possible due to the support of a number of key people. Firstly I would like to extend a thank you to my supervisors Dr Steven Marsh and Dr Omer Ali. They were a constant source of guidance during this project and provided a lot of insight in their feedback.

I would like to thank my colleagues at Waikato Regional Cancer Centre. Their support, both practical and moral in nature, was instrumental in completing this study. Most notably I would like to thank Dr Omer Ali and Dr Felix Wong. These two introduced me to the Ubuntu operating system and provided steps to help me configure the GATE software. I would also like to thank them for their continued support for the experimental component of this work. They spent many hours, both during their busy work week and in the weekend, to help me complete this work. For their support I am truly grateful.

I would like to extend a special thank you to Tom Egan for his help with programming solutions in Python. He saved me a lot of time by writing a script for some of the modelling performed. Lastly, I want to thank to my friends and family. These people are unknowingly the most instrumental part needed to finish a piece of work of this size.

Table of Contents

List of Figures

List of Tables

1 Introduction

X-rays are used extensively in clinical procedures for the diagnosis and treatment of disease. The use of x-rays in the treatment of cancer is the predominant application of radiation therapy. Radiation therapy uses treatment modalities that produce high doses of focal radiation to disrupt tumourous tissue, increasing the probability of cell death or halting its proliferation. By stopping the progression of tumour cells the likelihood of spread into surrounding healthy tissue is reduced.

Over the years, radiation therapy has developed greatly. A pivotal addition to the field was the introduction of linear accelerators (linacs), a high energy x-ray modality that treats tumours with a beam that originates outside of the patient. linacs are one of the most common methods for radiotherapy treatment as the high energy x-rays can be used to treat deep seated tumours that are often surgically inoperable. To treat a tumour while avoiding damage to healthy tissue structures the x-ray beam is conformed to the shape of the tumour. The need for accuracy in radiation therapy necessitates the use of individualised patient treatment plans. These plans are based on computed tomography (CT) image studies acquired before the beginning of treatment. Through the use of advanced treatment planning software, the dose deposition in individual patient anatomy can be accurately simulated. Recently technologies that improve the utility of radiation therapy include. Techniques such as intensity modulated radiotherapy (IMRT) and stereotactic radiotherapy (SRT) are employed by linacs to improve their ability to deliver highly conformal therapies. These radiation therapy delivery methods, in combination with 3D volumetric patient imaging and treatment planning software, have vastly improved the conformality of x-ray delivery to tumours while minimising the dose received by healthy tissue.

The use high doses of conformal radiation leads to the potential of a geometric miss for a tumour volume. These delivered doses have steep dose dropoffs outside of the targeted tumour and missing the target will result in significant underdoses to tumour volumes while overdosing healthy tissue. Image guided radiotherapy (IGRT) is technique applied to verify patient setup prior to radiation treatment. Images are acquired directly prior to treatment delivery while a patient is lying on the treatment couch. By delineating the tumour volume and surrounding anatomical landmarks clearly the patient's position relative to the intended dose distribution of the delivery can be clearly visualised. Set-up corrections may be made in an attempt to eliminate these misalignments and provide geometric verification of a tumour volume.

In order to delineate bone and soft tissue in IGRT cone-beam CT (CBCT) can be used. CBCT is an imaging technique used in diagnostic scanners that are integrated into a linear accelerator. CBCT acquires a 3D volumetric image set of a patient over a large imaging area, eliminating the need to move a patient through a scanner to attain an image. The 3D volumetric images are compared to the patient's original CT image and any changes in the patient anatomy can be evaluated as the treatment proceeds.

The use of CBCT imaging does involve a concomitant dose to the radiotherapy patient. The imaging doses from CBCT devices are largely excluded from the treatment planning dose calculation due to their relative magnitude to the therapeutic dose. The doses are typically around two orders of magnitude smaller than the delivered treatment dose. However, CBCT imaging involves a wide field of view and the dose distribution is not targeted to the tumour volume. This means that a homogeneous dose is delivered across the field, to both tumour and healthy tissue.

CBCT images may be acquired every day of a patient's treatment or once every week. For some of the most frequently imaged tumours, such as prostate cancer, CBCT imaging has been found to cause doses exceeding 5% of the therapeutic dose.[5] Based on current

radiobiological models for radiation-induced cancer risk doses of these magnitudes may not be negligible in the development of secondary cancers. Many believe that these doses should therefore be quantified and incorporated into radiotherapy treatment planning.

The ability to simulate the dose from low energy x-rays in treatment planning systems has been studied in the past with some success.[6,7] Although due to limiting assumptions for the modelled energy spectra and x-ray interactions the accuracy of these methods is questionable for routine patient dosimetry. For the most accurate assessment of treatment planning doses Monte Carlo methods can be used. Monte Carlo can be used to simulate the elementary particles of x-rays and track their transport through space, calculating the energy deposited from elemental interactions with matter. Monte Carlo methods are considered the gold standard of radiation therapy dose calculation and are widely used.

1.1 Thesis objectives

This thesis is split into two main objectives:

- To develop and validate a Monte Carlo model for CBCT dose calculation
- To perform Monte Carlo dose calculations for site-specific CBCT imaging protocols

To achieve the former of these two objectives the GATE Monte Carlo toolkit will be used. The CBCT scanner examined is the Varian x-ray imager (XI) which is Varian Truebeam integrated device. The model will be validated using experimental measurements. Once validated the doses calculated by simulation will be converted into absorbed dose by deriving a Monte Carlo calibration factor.
For the latter objective, the calibrated dose calculations will be used to simulate dose in an anthropomorphic phantom. Analysis of these dose calculations will enable the determination of organ doses and the estimation of radiation-induced cancer risk from effective dose. Finally dose-volume histograms (DVH) will be evaluated for site-specific CBCT imaging.

2 Theory

2.1 Radiation Biology

When treating a tumour volume with ionizing radiation the objective is the death of all tumour cells. The death of all the cells can be considered synonymous with the death of the tumour as a whole. It is known, however, that during a delivery of radiation not all cells will be killed. The survival probability of cells in an irradiated volume decreases exponentially with increasing radiation dose.[8,9] Mathematical radiobiological models are used to describe the relation between physical quantities of radiation and biological response. The survival fraction probability for large cell populations can be calculated using a Poisson probability distribution and the linear-quadratic (LQ) model of radiobiological response.[8,10]

$$SF = \exp^{-\alpha D - \beta D^2} \tag{2.1}$$

where SF is the surviving fraction of the cells, D is the dose delivered to the tumour and α and β are empirical constants characteristic to the cell. The relationship in equation 2.1 is used to plot cell survival curves such as that shown in figure 2.1. The curve plots the

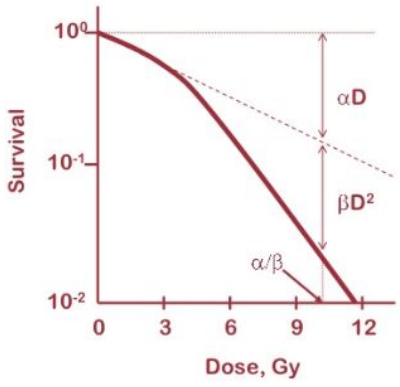

Figure 2.1: Linear-quadratic cell survival curve

surviving portion of a cell population on a logarithmic scale against dose on a linear scale. From equation 2.1 and figure 2.1 it is seen that the shape of the curve depends on only

the linear (α) and quadratic (β) parameters. In fact, the ratio (α/β) of the parameters turns out to be pivotal in estimating the radiation response of a given cell population. For example a low α/β value is observed for normal tissues that have a delayed death response to increasing doses of ionizing radiation. By contrast, high α/β values are seen in early responding and tumourous tissues.[11]

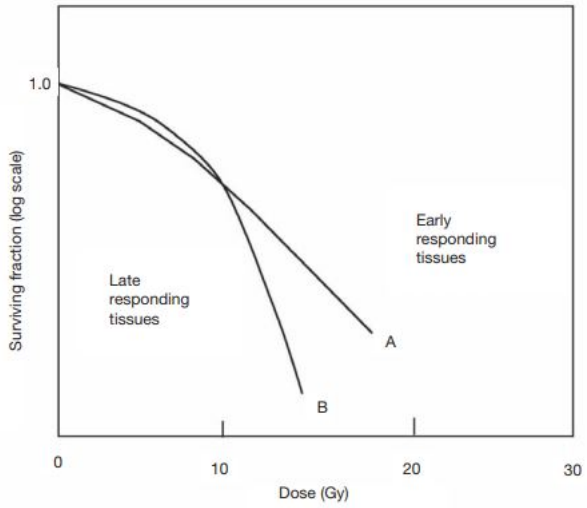

Figure 2.2: The linear-quadratic model is used for modelling cell survival curves. demonstrating a) The linear and quadratic components are marked b) Cell survival curves for early responding (curve A) and late responding (curve B) tissues.

By observing the cell survival curves in figure 2.2 it can be seen that late responding normal tissues (low α/β ratio) are preferentially spared over early responding tissues (high α/β ratio) at low doses. α/β ratios vary for different tissue types and choosing the best pattern of dose deliveries for radiation treatment will depend on their values. The benefits of low dose fractionation on normal tissue survival is seen in the theoretical model shown in figure 2.3. The figure displays the early response of tumourous tissue at low doses. As radiation dose increases, both tumour control and normal tissue toxicity increase. To improve the probability of controlling the tumour while minimising the normal tissue complications the early sensitivity of tumours can be exploited. The desired outcome

from radiation therapy is to maximise the dose effect relationship for tumour control and minimise the relationship for normal tissue toxicity.[8] The difference between the two curves is referred to as the therapeutic index, which is a distribution which measures the therapeutic effect of radiation against the toxicity caused. To achieve the desired outcomes of radiation therapy the therapeutic index should be maximised.

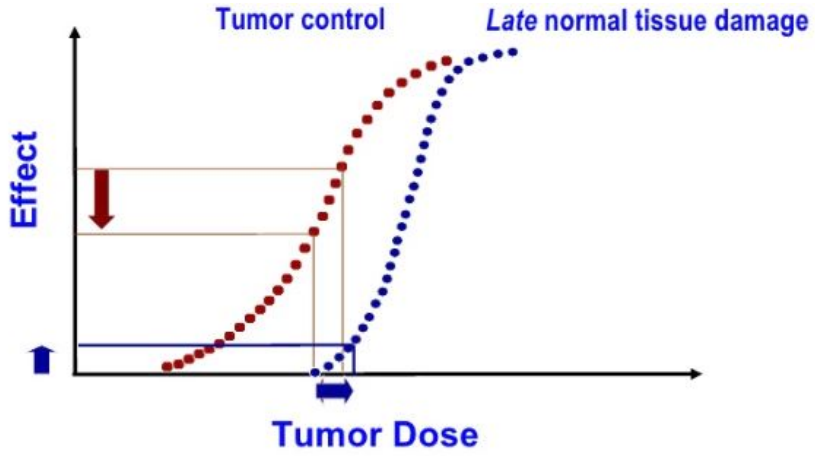

Figure 2.3: A theoretical model showing the sigmoidal dose response of both tumorous tissue and healthy tissue to ionizing radiation. As shown the damage response of tumorous cells is activated at a lower dose threshold than that of normal cells. The difference between the two dose response curves is known as the therapeutic index (TI). The TI compares the therapeutic effect from a given dose to the amount of toxicity it causes.

2.2 Radiation therapy

Radiation therapy is the treatment of cancer with ionizing radiation. External beam radiation therapy is a method of radiation therapy delivery in which radiation is delivered to a tumour from a source external to the patient. EBRT is commonly delivered with a linear accelerator (linac - figure 2.4). A linac is a high energy x-ray modality that can be used to treat deep seated tumours that would otherwise be unable to receive surgical intervention. The x-ray beam produced by a linear accelerator is shaped to conform closely

Figure 2.4: A Varian Clinac linear accelerator

to the shape of a tumour. In this way a therapeutic dose may be delivered to the tumour volume while sparing the healthy surrounding tissue. A linac is capable of delivering a conformal x-ray beam from a number of static or moving positions to a tumour volume. The linac rotates around a central position in 3D space known as the isocentre. This point is a fixed distance of 100 cm away from the x-ray beam source at all angles. The isocentre is used to mark the centre position of a treatment. For the purposes of this study radiation therapy can be divided into three main steps: Imaging and delineation, planning, and verification and treatment

2.2.1 Imaging and delineation

Delineation of a tumour volume is vital in radiation therapy. By accurately identifying a tumour volume a therapeutic dose can be planned to cover the entire extent of the disease. CT imaging is vital during this step. A CT scan is the first step in planning radiotherapy. An image is acquired of the patient over an area containing the tumour volume. The image visualises the internal anatomy and the position of the patient on the treatment couch. Reproducible positioning of the patient relative to the treatment couch is important as it needs to be replicated when the patient is later treated with a linac. Immobilisation devices are used to hold the patient's position throughout the procedure. An external laser system that is aligned with the centre of the imaging plane

of the CT is also used for patient setup. Before a scan marks are drawn on the patient's skin to aid in relating the patient position to the imaging plane. The marks on the patient are later tattooed to the patient's skin and are used for setup relative to the linac isocentre.

The CT image is a volumetric image set of the tumour and its surrounding anatomy. As part of the treatment planning process the following volumes are defined on the image set:

- The gross tumour volume (GTV) is the volume that consists of the visible extent of the tumour and any metastatic disease. This volume is often defined by prior clinical examination. For tumours that do not have well defined boundaries other imaging techniques, such as MRI and PET, can be superimposed on to the CT image to identify the extent of disease.

- The clinical target volume (CTV) is an expansion margin around the GTV. In some cases lymph nodes or other tissues surrounding tissues may be at risk and require treatment. The CTV is based on the site and biological behaviour of a specific tumour type.

- The planning target volume (PTV) is a margin expansion of the CTV. It is a geometric concept and accounts for an uncertainties in patient setup, anatomical positioning or linac dose deliverability. Dose in radiation therapy is prescribed to this volume.

- Organs at risk (OAR) are normal tissue volumes that are in close proximity with the tumour volume. OARs are radiosensitive structures that are at risk of being damaged by radiation. These structures are given specific dose constraints that should not be exceeded during treatment planning.

The volume that is actually treated during radiation therapy will, in general, be larger than the PTV (figure 2.5). This depends on the treatment technique used. Additional regions of interest (ROI) may also be defined for individualised treatment plans.

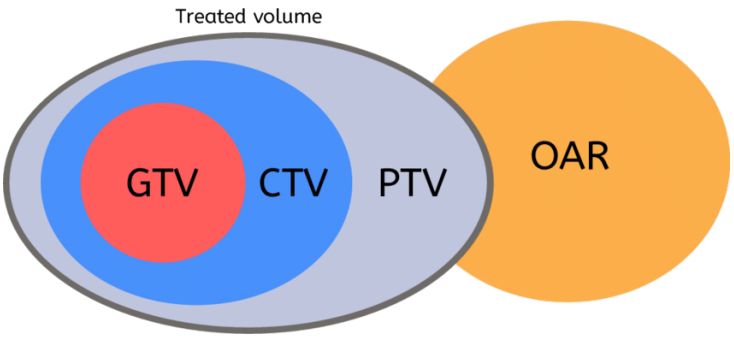

Figure 2.5: Radiotherapy treatment planning volumes. Volume definition is required for 3D treatment planning software to measure accurate dose-volumes. Adapated from Pave[1]

2.2.2 Planning

Once the tumour and OARs are delineated on the image set a treatment plan is developed. At this step decisions are made about x-ray beam geometries and beam arrangements used to treat the PTV. The need for accuracy in radiation therapy dose delivery requires detailed dose calculation capabilities. These calculations are performed on the patient-specific CT image set to maximise the possible therapeutic index of the treatment and improve patient outcomes. A treatment planning system (TPS) is a software system used to develop complex plans based on these image datasets to calculate 3D dose distributions.

Treatment plans will use a beam arrangement that may consist of one to several fields with varying beam energies, angles, movements and intensities. An optimal beam arrangement will ensure that the prescribed dose is delivered to the treatment volumes whilst minimizing the dose to OARs. After the beam arrangement is established, the dose distribution to the patient volume can be calculated. The accuracy of the dose calculation in a TPS is dictated by the accuracy of the underlying dose calculation algorithm. Deficiencies exist in these algorithms and may be effected by patient external contour, x-ray beam shaping and modification, and tissue heterogeneities. It is important to know which scenarios different algorithms can be used in. After the dose distribution is calculated it is displayed on the patient data set.

Dose-volume histogram

A 3D dose distribution contains a lot of data and the dose received by the delineated volumes needs to be displayed in a meaningful way. Dose-volume histograms (DVHs) are generally used for dose evaluation of a treatment plan. Cummulative DVHs (shown in figure 2.6) plot the percentage volume of a structure on the vertical axis against dose on the x-axis. To explain how DVHs are interpreted the critical structure (or OAR) in figure 2.6 is examined. The dose on the x-axis represents the minimum dose that is received by the highest dose exposed portion of that volume. For exampled the minimum dose received over the highest exposed 50% of the critical structure is 22 Gy. The minimum dose received by the structure will increase as the volume becomes smaller. In this case the volume will be receiving at least 44 Gy in the most exposed 10%. The dose progression continues until the smallest examinable volume is measured. At this volume the structure which will be receiving the maximum dose.

For radiotherapy dose reporting DVHs can be annotated in the form of simple dose metrics. In the case of figure 2.6, the minimum dose received over the highest exposed 50% of the critical structure is denoted $D_{50\%}$=22 Gy. The minimum dose received by the highest exposed 10% of the critical structure is $D_{10\%}$=44 Gy. DVHs are used to evaluate how uniformly a prescribed dose is delivered to a PTV and to check the dose received by an OAR is within its dose constraints.

2.2.3 Verification and treatment

When a treatment plan is approved and ready to treat it is transferred to a linear accelerator. Prior to radiation treatment the patient is immobilised on the treatment couch in the same manner as during CT imaging. The tattoos placed on the patient during CT imaging are used for alignment with the in-room laser system. The lasers intersect

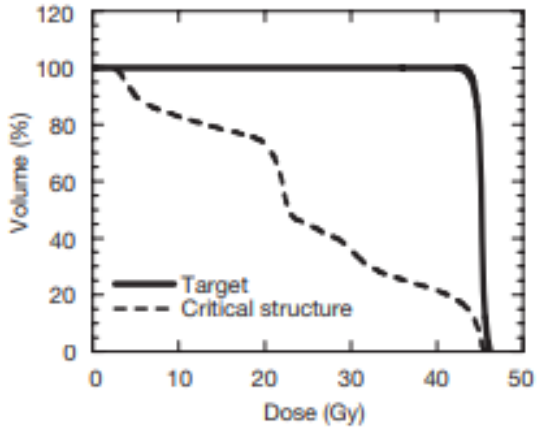

Figure 2.6: A cumulative dose-volume histogram (DVH). The first bin of the histogram contains the volume of the structure that will receive at least 0 Gy (100%). The remaining bins are used to analyse the minimum dose that is received for a given volume of the structure. Adapted from Podgorvsak (2006)[12]

through the isocentre of the linac in the saggital, coronal, and transverse planes of a patient.

Verification of the tumour position is required prior to treatment delivery. A linac is equipped with imaging systems for both kilovoltage (kV) and megavoltage (MV) imaging which are both capable of providing delineation of anatomical structures. These images are taken to align a patient to the centre of the treatment field, using their planning CT image as a reference. Imaging a patient to detect and correct setup errors is a practice known as image-guided radiation therapy (IGRT).[13] Images acquired during IGRT provide visulasation of tumour and normal tissue structures. These structures are used to match the IGRT image to the reference CT image. The best possible fit is indicated by minimising the shift in specific matching structures, which may be soft tissue or bony structures. The image registration parameters given from matching are used to apply corrections to the patients setup.

Accurate and reproducible dose delivery is essential in radiotherapy. The sigmoidal dose-

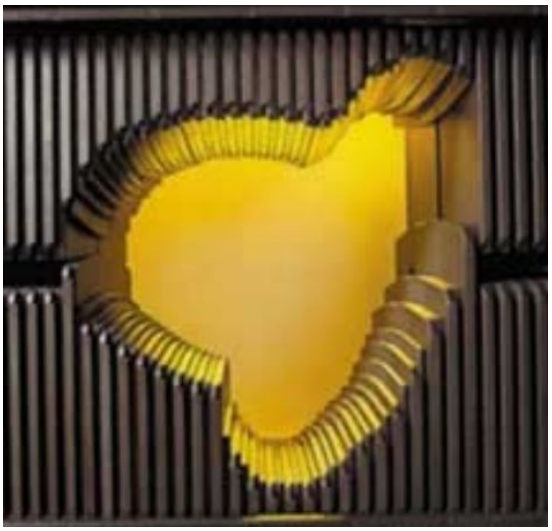

Figure 2.7: Multileaf collimator (MLC). MLCs delivered intensity modulated radiation doses to a tumour volume over time by moving between different control points. Adapted from Jeraj (2004)[2]

response curves shown in figure 2.3 demonstrate that small discrepancies in delivered dose can have large effects on tumour control and normal tissue damage. If a tumour is misaligned to a treatment field prior to radiation therapy this may result in large underdoses for the tumour or overdoses for surrounidng health ytissue. Therefore, geometric verification is of high importance to radiation therapy.

Once the tumour volume has been verified the radiation treatment plan is delivered. Radiation is delivered using the planned beam arrangements. The delivery time will vary depending on the technique used. Intensity modulated radiation therapy (IMRT) uses a static beam with motion controlled tungsten leaves (multileaf collimators (MLC) - shown in figure 2.7) to deliver x-rays with time-varied intensity over the tumour volume. The time to deliver the treatment can be up to 6 minutes for nine static beams.[14] Arc therapies involve modulated beam delivery while the linac gantry rotates around the patient. One full arc (360° rotation) can be delivered in under 2 minutes.

2.3 Imaging modalities

2.3.1 Computed tomography (CT)

CT (or computed tomography) is a commonly used medical imaging device for creating 3D images of the human body. CT scanners are used to acquire images for the purpose of treatment planning in radiation therapy. The geometry of conventional CT scanners is known as fan-beam CT. A fan-beam CT system involves the use of an x-ray tube (source), an opposing ring shaped detector. The source and detector are mounted in a CT bore on a slip ring that allows them to continuously rotate around a patient (Figure 2.8a).

X-rays originate from a focal point in an x-ray tube and spread in a fan beam pattern. A fraction of the these x-rays will pass through a patient and reach the detector. The remaining x-rays will be absorbed and scattered by interactions within the patient. These interactions will be explained in section 3.3.

The detection of modulated x-ray beam profiles is the principle that allows for CT image formation. The differences in x-ray attenuation through a patient produce variations in contrast in the resulting image. Beam acquisitions at each tube angle are stored as a projection image. Projection images are acquired over a large number of angles around the patient (Figure 2.8b). The images are then reconstructed and compiled to provide an estimate of the inner structures.

The reconstructed image matrix is a 3D representation of the human anatomy which is comprised of voxels (Figure 2.9). Each voxel has a value that represents an attenuation value for the x-rays that have passed through the human anatomy. The increase in attenuation coefficients are visually represented as a linear progression in grayscale intensity. The Hounsfield unit (HU) scale is a linear transform of these attenuation coefficients in which the radiodensity of water at standard temperature and pressure is defined as zero. Voxel values in CT images are scaled in terms of this transform. The HU of a material is

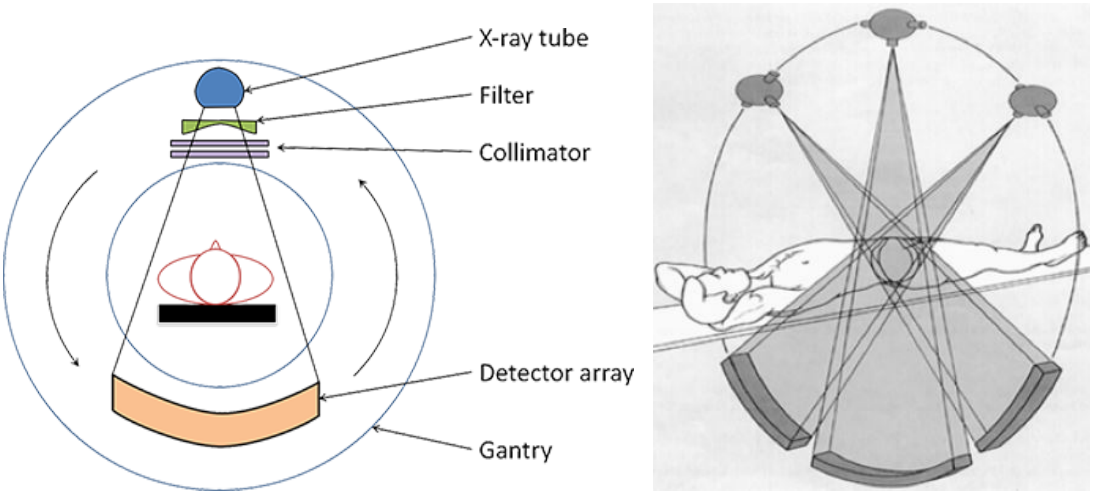

(a) (b)

Figure 2.8: CT scan a) a basic diagram with labelled CT components b) Projection images are acquired from a large number of angles to construct a 3D representation of the patient inner structures. Figure from Kalender, W. A. (2011)[15]

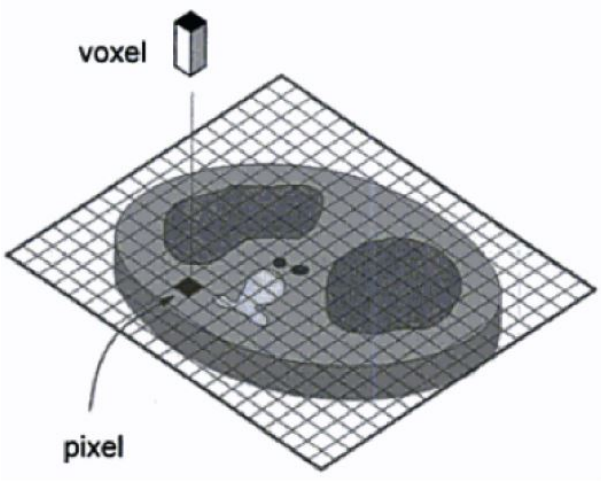

Figure 2.9: A CT image is comprised of transverse slices. Each transverse slice is a voxelised 2D grid. Each voxel contains a gray scale value representing the density of the corresponding anatomy

defined using the following equation

$$HU = 100 \times \frac{\mu - \mu_{water}}{\mu_{water} - \mu_{air}} \tag{2.2}$$

where μ represents the linear attenuation coefficient of the material, μ_{water} is the linear attenuation coefficient of water, and μ_{air} is the linear attenuation coefficient of air.

The collimation of the fan beam and width of the detector elements determines the imaging resolution of anatomy in the superior-inferior direction (Figure 2.8b). The width of the fan beam is typically on the order of 1 cm.[5] To image larger volumes the patient couch is translated through the bore of a CT scanner while images are acquired by the rotating source and detector. If the patient couch is translated in discrete steps and imaged at each stopping point it is known as an axial scan (Figure 2.10a). If the patient couch is translated continuously while imaging it is referred to as a helical scan (Figure 2.10b). To image a large volume, without translating the patient couch, both the fan beam and the detector can be widened in the direction of the couch travel (axial direction). This geometry is known as *Cone beam CT*.

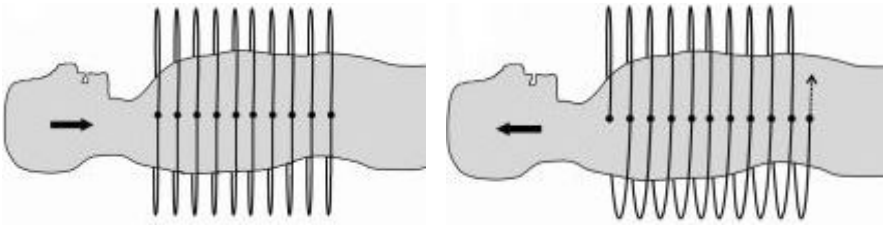

(a) Axial scan (b) Helical scan

Figure 2.10: CT scanning acquisition types

2.3.2 Cone beam CT (CBCT)

Cone-beam CT (CBCT) is a wide fan beam acquisition technique. It can be used for diagnosis, IGRT, and treatment review. CBCT is the most common IGRT modality used in radiation therapy.[5] Unlike fanbeam CT, a cone-beam image is taken in a single gantry

rotation around a patient. The treatment couch is stationary during imaging. Because of this the superior-inferior scanning volume is limited by the extent of the beam collimation. An illustration comparing a fanbeam CT geometry with a CBCT geometry is shown in Figure 2.11. CBCT is offered by most linac-integrated x-ray imaging devices (see Figure 2.12). Unlike the multi ring detectors used for fanbeam CT, CBCT images are acquired with a high resolution 2D amorphous silicon panel detector. The x-ray unit and detector are mounted on opposing sides of the linac.

The treatment couch remains stationary during CBCT acquistion but it is highly susceptible to motion artefacts. A full rotation takes around a minute and during this time any patient movement can effect the quality of the image. Due to the large imaging field scatter received by the detector panel is also significant. This leads to lower image contrast and signal-to-noise ratio (SNR) than in conventional CT. IGRT methods such as CBCT are used for quantifying setup error prior to treatment delivery. The utility CBCT has over other IGRT x-ray methods is the ability to monitor changes in patient anatomy. Changes in patient external contours or internal anatomy occur frequently over the course of radiotherapy. These changes will affect the treatment distances and, subsequently, the organ dose distributions of therapeutic radiation. Large changes in patient anatomy between the patient's planning CT and the CBCT for the present fraction will greatly influence the accuracy of treatment delivery. In some cases the planning CT image is no longer valid for treatment delivery. CBCT alone provides the ability to assess these changes prior to radiation delivery.

There are two vendors that supply CBCT systems for radiation therapy: Elekta and Varian. Elekta produce the X-ray Volumetric Imager (XVI) while Varian produce the On-Board Imager (OBI) and, more recently, the X-Ray Imager (XI).

2.3.2.1 Varian XI

The Varian X-Ray Imager (XI) is a CBCT scanner. It is integrated with the Varian Truebeam linear accelerator (shown in figure 2.12). It consists of an opposing x-ray source

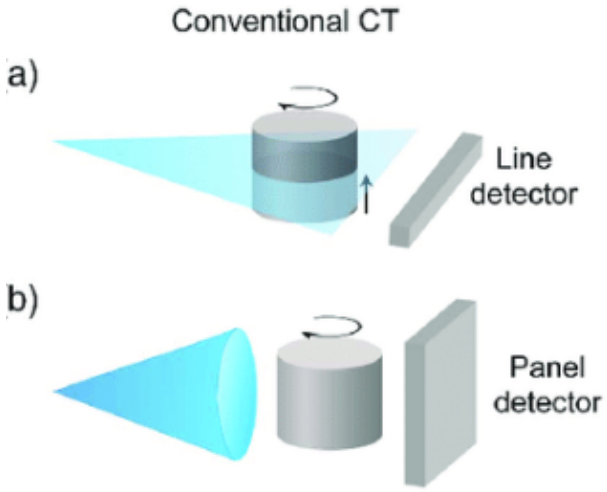

Figure 2.11: A comparison between two CT acquistion techniques. a) Conventional (fan beam) CT. Fan beam CT uses a narrowbeam configuration to capture an image using sub-centimeter slice widths. An object will be translated through the fan beam arrangement until the line detector has acquired data over the volume of interest. b) Conebeam CT (CBCT). CBCT uses a wide beam arrangement to capture an image. CBCT can acquire an image over a much large volume for a stationary object. It is acquired at the expense of image quality.

and detector. The source arm consists of an x-ray tube and a series of collimation materials and filters. These components can be configured to adjust the beam geometry and energy spectrum from the x-ray tube used for imaging. There are two main beam configurations used for CBCT imaging in the XI system. These configurations will be referred to as the head scan protocol and the body scan protocol. The head scan protocol uses a 100 kVp beam and full bowtie filter. It has a smaller FOV for head and neck imaging (Figure 2.13a). The scan arc used for the head scan protocol is 200deg. The body scanning protocol uses a 125 kVp beam and the half bowtie filter. This mode is intended for imaging larger objects. The beam collimation is offset so that only part of the anatomy is imaged in a single projection (Figure 2.13b). As the gantry completes a 360° rotation around the object a full picture of the anatomy is formed. When configured in

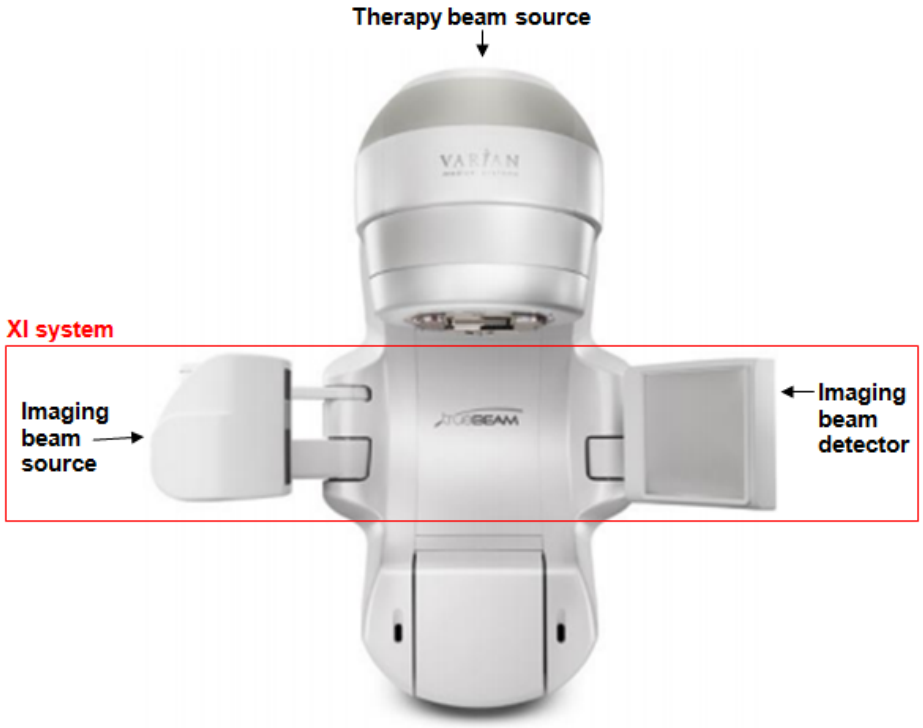

Figure 2.12: A Varian Truebeam linear accelerator. The imaging components (source and detector) are mounted on either side of the therapy beam source (treatment head)

this way, the beam arrangement reduces the skin dose recieved by the patient compared to a full FOV. Scattered radiation is also reduced, which leads to an increase image quality.[17]

The bowtie filters are x-ray beam shaping tools that are mounted in front of the x-ray source. They are made of an aluminium alloy which is thin at the centre of the beam and increases in thickness towards the edge of the beam. The increasing thickness provides increased x-ray attenuation towards the edge of the beam. The filter is shaped in this way to increase the homogeneity of the dose over the patient volume.[18] As there is less tissue to pass through at the periphery of the patient less x-rays are required to pass through. Additional benefits of the bowtie filter is an overall improvement in CT number accuracy, image unifomrity, and contrast detectability.[18]

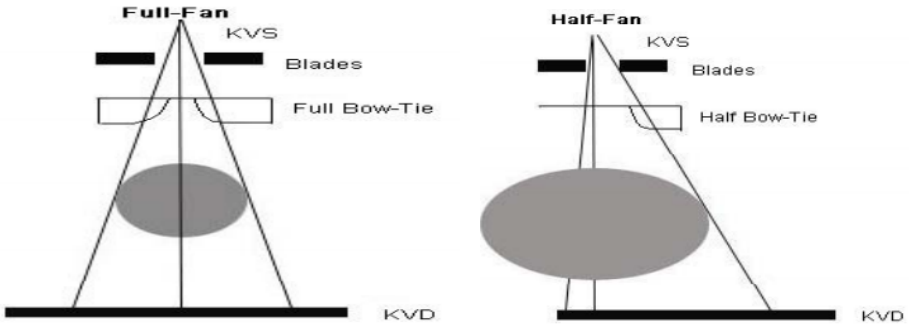

(a) Head scan beam arrangment (b) Body scan beam arrangement

Figure 2.13: The XI scanner includes a source and opposing detector. The following illustrations depict the geometry used in both a) full bowtie filter setup (employed in head CBCT acquisition) and b) half bowtie filter setup (employed in both pelvis and thorax CBCT acquisition). Both bowtie filters are used to selectively attenuate x-rays at the edge of the field. Figure adapted from Wen et al. (2007)[16]

There is an additional filter in the head of the XI scanner for CBCT imaging. A titanium beam hardening filter is placed immediately before the bowtie filter and preferentially absorbs x-rays at the lower end of the beam's energy spectrum. Low energy x-rays are attenuated to decrease the number of x-rays attenuated in the patient, which decreases the imaging dose recieved by the patient.

2.4 Radiation quantities

The elementary particle of x-rays and other electromagnetic waves is the photon. Photons undergo nuclear reactions with atoms in which they transfer their energy to orbital electrons. By transferring a sufficient amount energy they can overcome the binding energy between the electron and its atomic nucleus, freeing the electron. The electron will undergo inelastic collisions with neighbouring nuclei and orbital electrons, depositing energy into its surrounding medium.

Radiation dose refers to the energy imparted to a medium per unit mass from ionizing

radiation. Using The International System of Units (SI) absorbed dose from ionising radiation is defined in joules per kilogram (J/kg). In radiation dosimetry this relationship is denoted with the unit Gray (Gy). Another quantity used in radiation dosimetry is Kerma. Kerma (or "**k**inetic **e**nergy **r**eleased per unit**ma**ss") is the initial energy deposited in a mass due to interactions from ionizing radiation.[19] Energy transferred from x-rays to electrons is deposited in a medium by collisional and radiative interactions (bremstrahlung). This results in two components of kerma: collisional kerma and radiative kerma. This quantity is important in the dosimetry of low energy photons, such as those used in diagnostic procedures, as the range of liberated electrons is short. Electrons with kinetic energies below a few hundred kilovolts will deposit their energy within a sub-millimeter distance of the photon interaction site. The radiative component of kerma is negligible. So in this scenario the energy deposition is assumed to be local to the primary interaction site and the value of kerma is numerically equivalent to absorbed dose.

Radiation dosimetry is the practice of measuring radiation quantities. In radiation therapy dosimetric measurements from a radiation source are performed under a wide range of beam configurations. Theses configurations use different measurement points, detectors, and mediums. In a clinical environment it is necessary to perform dose measurements so that a relationship between the radiation source and a human body can be established. Absorbed dose measurements typically fall into two categories: absolute and relative.

2.4.1 Absolute dosimetry

Aside from using a calorimeter, dose can not be measured directly. However, a number of detectors can be used to relate a measurement of ionising radiation to absorbed dose in Gy. Absolute dose measurements are standardised measurements that can be used as baseline data and reported across radiotherapy departments. Absolute dose is measured under controlled reference conditions, termed *reference dosimetry*.[20] Reference dosimetry is an accurate dose measurement performed under conditions stipulated in published guidelines. The measurements are performed under conditions that are practical to relate

the radiation source to the position of a tumour. The reference conditions are given from published guidelines and stipulate measurement geometries, choice of detector and correction factors to apply to measurements. The set conditions are used to accurately measure a point dose in Gy. Measurements are often made in objects known as phantoms that are specially designed measurement objects that mimic human anatomy. The phantoms are often water-based as the radiation scattering and absorption properties of water are similar to human tissue.

A calibration factor is used to convert the chamber's response to dose in Gy. The calibration factor may be given in terms of either absorbed dose or kerma. The factor is traceable to a primary standard as part of the international measurement system. Accredited Dosimetry Calibration Laboratories (ADCL) develop and maintain primary standards for radiation measurements. These standards are compared with other standards labs worldwide to keep consistency in measured quantities.

2.4.2 Relative dosimetry

Often tumours will be treated under conditions that vary from the conditions used in reference dosimetry. Relative dosimetry measurements are performed to relate reference dosimetry measurements to a range of clinical conditions. The relationship established between the source and a human body from absolute dosimetry can therefore be adjusted for several different exposure scenarios.

One common scenario involves a change in depth of a tumour. If a tumour depth varies from that measured in reference dosimetry the output can be adjusted using a percentage depth dose (PDD) factor. As an x-ray beam traverses a medium it loses energy from attenuation and scattering. A PDD relates the absorbed dose deposited by a radiation beam with depth in a medium. The dose values are normalised by dividing their values by the maximum dose, referred to as d_{max}. A PDD for a 6 Megavolt beam is seen in figure 2.14a. As shown the maximum dose of a 6 MV x-ray beam will be deposited at around

1.5 cm deep in a body of water under a 10 cm x 10 cm field. For kilovoltage x-rays the maximum dose is deposited within a few millimeters from the water surface.[21] This poses problems in reliably determining the d_{max} of kV beams.

Reference dosimetry is performed at a given depth through the centre of a radiation beam. For a completely uniform beam it would be expected that doses measured at a distance off the central axis of the beam would be identical to the centre. However in practice this is not seen. The off axis ratio is quantified to determine the dose at a point off the beam centre relative to the central axis. By plotting the off-axis ratio along length of the radiation field the dosimetric profile of the beam is given (figure 2.14b. Off-axis ratios can be determined for differing field sizes and depths.

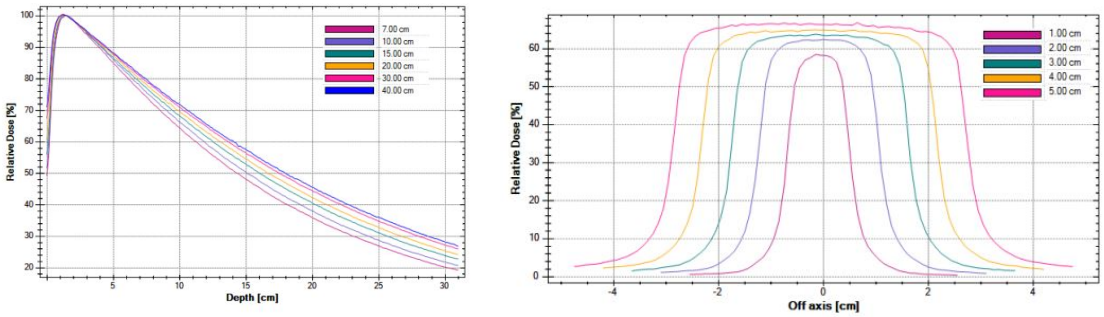

(a) Percentage depth doses

(b) Dosimetric profiles

Figure 2.14: Relative dosimetry data for a 6 Megavolt x-ray beam in water. Different square field sizes for the beam are indicated by the legend

2.5 Radiation detectors

Radiation dosimetry is one of the key areas of application for detectors. Detectors can be used to measure both absolute and relative dose. Some detectors can be used to measure the dose delivered to a patient during radiation therapy treatment.[19]

An ideal radiation detector will produce accurate and precise readings over a range of

setup and source conditions, have a linear response to dose over a range of exposures, have a low detection threshold for low dose exposures, be tissue equivalent, and have high spatial resolution.

This section will explore the principles of operation of the radiation detectors used in this work. Additional theory for dose calculation with these detectors will also be included.

2.5.1 Ionisation chambers

Ionization chambers are one of the most widely used radiation detectors.[19] An ionisation chamber is essentially an anode and a cathode separated by a gas-filled chamber. There is a potential difference applied between the anode and cathode to create an electric field. When a charged particle enters the electric field it interacts with the molecules of the gas. If the particle deposits energy to an atom that exceeds its ionization energy threshold an ion pair will be created. Ion pair creation relates to how much energy has been deposited in the gaseous medium. Positive ions from the ion pair will move towards the cathode while free electrons flow towards the anode. The electrons are registered at the anode as an electronic pulse. These pulses are usually too small to measure directly. The electrons from multiple ion pair creations are allowed to accumulate before a current is measured. The current measured over a discrete time interval is equivalent to the charge measured by the chamber which is related to dose by the use of a ADCL calibration factor.

Ionisation chambers are the primary detector used to perform reference dosimetry in a clinical. Ionisation chambers (Farmer-type) have a small energy dependence over a range of diagnostic and therapeutic energy levels.[21] However, an ionisation chamber's response is sensitive to a number of conditions. Air density, exposure rate, ion recombination losses and electric field polarity will all effect the ion pair collection rate.[22] These factors are accounted for by reference dosimetry protocols.

AAPM TG61 reference dosimetry protocol

The American Association of Physicists in Medicine (AAPM) established a protocol for the reference dosimetry measurement of kilovoltage (kV) energy x-rays. The measurable range for this protocol is 100 kV to 300 kV. The absorbed dose to water is determined at a point 2 cm deep in a water phantom and is evaluated using the following formula.

$$D_w = M_{pl} N_k P_{Q,chamber} P_{sheath} \left[\left(\frac{\overline{\mu_{en}}}{\rho} \right)^w_{air} \right]_{water} \tag{2.3}$$

Where M_{pl} is the chamber reading corrected for ion recombination, polarity, temperature, presuure, and electrometer response (nC), N_k is the air-kerma calibration factor adjusted for the spectrum of the user's beam (mGy/nC), $P_{Q,chamber}$ is the chamber correction factor which accounts for the individual response a chamber, and $[(\overline{\mu_{en}}/\rho)^w_{air}]_{water}$ is the water-to-air ratio of the mean mass energy-absorption coefficients, measured in water.

Each variable in equation 2.3 is derived from the half value layer (HVL). HVL is an important precursor value for TG-61 reference dosimetry. All the variables involved in dose calculation are provided in tabulated lookup tables which are indexed by their HVL value. The HVL is a quantity related to the 'quality' of an x-ray beam. It is defined as the thickness of a specified material that is required to attenuate the air kerma rate of a narrow beam to half its unattenuated value. It is expressed in mm of thickness of high purity aluminium or copper.

2.5.2 Thermoluminescent dosimeters

Thermoluminiscent dosimeters are crystalline materials used for radiation dosimetry. The principle of operation relies on the radiation luminiscnece of the crystalline structure. When undergoing a photon interaction energy is transferred to electrons in the valance band of crystalline atoms. The energy given to the electron elevates it to a higher energy "conduction" band. Due to defects in the crystalline atomic structure the electrons do not recombine with the vacancy in the shell. The electron-hole pair are captured in "traps" between the valance and conduction band. An electron trap represents a metastable

state of the atom (Figure 2.15a). By adding thermal energy to the system trapped electrons can exceed the activation energy required to move back into the valance band (figure 2.15b. In the valance band electrons will recombine with the electron holes. The recombination process results in the emission of a photon of energy equal to the gap between the conduction and valance band. For a TLD this band gap energy (on the order of 1 eV) results in the emission of visible light.

To exceed the activation energy for each electron trap heat is delivered to the system.

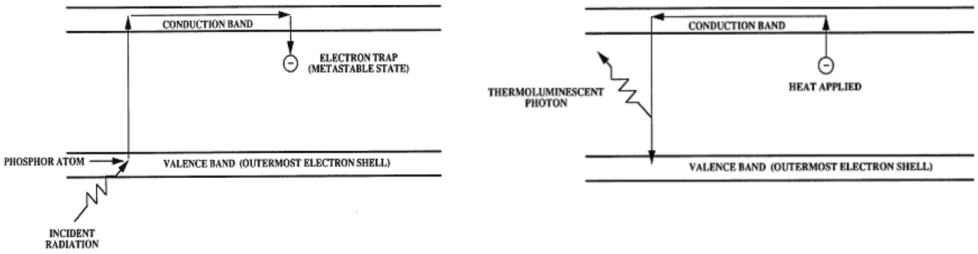

(a) (b)

Figure 2.15: Electron energy level transitions in a TLD material (a) An incident photon interacts with an orbital electron and gives it sufficient energy to move into the conduction band. It is then trapped in a metastable state due to defects in the crystalline structure (b) when sufficient thermal energy is applied the trapped electron returns to the valance band emitting heat and visible light

There may be multiple band gaps in a TLD structure and sufficient thermal energy must be supplied for visible light emission from different trap ”depths”. A TLD reader will supply an increasing amount of heat until emissions are measured from all possible metastable states. A photo multiplier tube is used to amplify the signal from the emissions. The reader will display the intensity of these emissions as a function of temperature. A typical glow curve produced by a TLD reader is seen in figure 2.16

TLD-100

The most commonly used TLD material is Lithium Floride doped with with magnesium and titanium (TLD-100). Lithium floride has similar radiation interaction properties

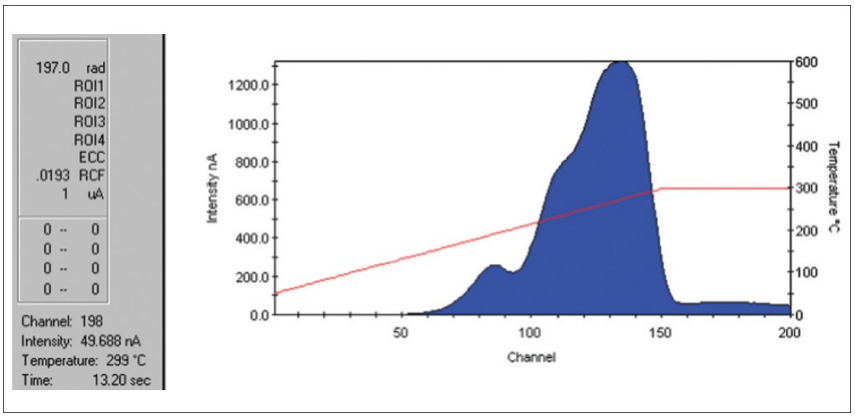

Figure 2.16: A glow curve given by a Harshaw TLD reader. The intensity in nA is a measure of thermoluminscence at a given temperature. There is a fixed rate of heating up until the main thermolumiscence peak. After this the temperature stays fixed and measures any residual emissions.

to human tissue for kilovoltage x-rays.[22–25] This means the material will absorb and scatter photons to the same extent as irradiated tissue. TLD-100s have suitable detection thresholds for low x-ray dose applications. Del Sol Fernández et al. found the minimum detection threshold for TLD-100 dosimeters was below 1 mGy.[25] The group also found that the dose response of TLD-100 dosimeters was linear over a range of diagnostic x-ray doses. However, TLDs have been shown to have large energy responses for kilovoltage x-ray beams.[21] It is therefore recommended that in the range of 20 - 250 kVp beams they be calibrated using the same beam energy they are intended to be applied with.

TLD dose calculation

The light output of a TLD when readout in a TLD reader is measured in charge (C). To relate the reading to an absorbed dose value there are a number of factors that must be accounted for. Absorbed dose is caclulated for an indivdual TLD by the following formula:

$$D_i = M_i S C F_i N_{w,batch} \tag{2.4}$$

where the dose, D_i, is given in mGy, M is the charge measured during TLD readout (nC), SCF is the sensitivity correction factor of the TLD, and $N_{w,batch}$ is the TLD batch calibration factor (mGy/nC).

The SCF is a unique value that is assigned to each TLD. It accounts for the individual variation among a group of TLDs under the same exposure conditions. Applying individual SCFs can reduce the relative standard deviation from a batch of TLDs from around 20% to a few percent.[25] These variations arise due to the difference in crystalline structure of each TLD. For a batch of TLDs irradiated to equal dose the SCF for a TLD in that batch can be evaluated by the following:

$$SCF_{ij} = \frac{\sum_{i=1}^{n} R_{ij}}{nR_{ij}} \tag{2.5}$$

Where R_{ij} denotes the j^{th} readout for the i^{it} chip in a batch. To attain an acceptable relative standard deviation for a chip SCF it should be irradiated multiple times. For a chip in a batch irradiated m times the average calibration factor is as follows:

$$SCF_i = \frac{\sum_{j=1}^{n} C_{ij}}{m} \tag{2.6}$$

$N_{w,batch}$ is an energy-dependent calibration factor. It converts the light output of a TLD to a value in kerma or dose. To measure the calibration factor TLDs must be irradiated under reference conditions with a calibrated instrument that holds a calibration factor traceable to an Accredited Dosimetry Calibration Laboratory (ADCL).

2.6 CBCT dosimetry

The dose from CBCT imaging in radiation therapy is often overlooked due to its small magnitude relative to therapeutic doses of radiation. In most cases the dose is not quantified as part of a radiation therapy treatment plan. However studies of CBCT dose have

shown that these doses may not be insignificant over an entire course of radiation therapy treatment. Some studies have shown that the dose from CBCT can exceed 5% of the therapeutic dose.[5,26,27] Islam et al. measured doses from the Elekta XVI in a cylindrical phantom and reported doses of up to 35 mGy per scan.[28] Studies of the Varian OBI have reported organ doses of up to 100 mGy (for OBI v1.3) and 60 mGy (OBI v1.4) per scan.[29] Studies comparing the two scanners side-by-side have confirmed these values.[30,31]

Many studies have sought to quantify the dose delivered from CBCT imaging. Common methods include the use of indirect measurements such as dose indicies in standardised cylindrical phantoms.[32–34] Other methods involve direct measurement, using TLDs or other dosimeters to measure absorbed dose in-vivo or in an anthropomorphic phantom.[16,30,35,36] To relate absorbed dose to radiation-induced cancer risk radiation protection properties such as effective dose can be used. Monte Carlo simulations have also been used by a number of groups.[5,37–42]

2.6.1 Low dose radiation exposures and secondary cancer risk

With the exception of fluoroscopy perceptible acute effects of radiation (deterministic effects), such as skin reddening and hair loss, are not seen in diagnostic x-ray irradiations. The risk that is posed by imaging radiation dose is the stochastic risk of cancer development. These are long term effects that are not well understood due to a lack of epidemiological evidence.[43,44] However, a number of studies do suggest that low doses of radiation pose a statistically significant increase in cancer risk.[43–46]

Studies of survivors of the atomic bombings in Hiroshima and Nagasaki provide the best data on risk estimates for development of secondary cancers. The studies involve a very large sample size of subjects of varying ages, genders, and received doses. This includes subjects that were present during the bombings but far enough away from the bomb site to have received a negligible to no radiation exposure from it. Long-term follow-up studies on cancer development in these populations discludes the influence of demographic

and lifestyle factors that may be confounding factors.[44] There are limitations in the data due to inaccuracies in dose estimation and tracking of survivors. However, these studies represent the best avialbe data to represent the relationship between dose and cancer risk. The data has been used to form the basis for the dose-risk models that are currently applied in radiation protection practices.

Despite the lack of epidemiological studies there is further difficulty in assessing the long-term risks posed by CBCT imaging due to the concomitant therapeutic dose. The inability to separate these doses results in further limitations for the dose risk posed by CBCT. There are many studies on the risk of secondary cancer development following radiation therapy. After surviving from a primary malignancy, 17%-19% of patients will go on to develop a secondary malignancy.[47–49] These factors will vary due to factors such as the age, genetic predispositions, the anatomical site studied, and the dose and volume of the irradiated site.[50] The most site-specific data comes from Cervical and prostate cancer follow up studies. These studies show a significant link between these patients and the development of secondary cancers in the pelvic region, where the highest dose is delivered.[51] Increases in cancers of the lymphatic system, bone and kidneys were also observed. A controlled study for malignant prostate tumours found 6% increase in secondary cancer onset when treated with radiation therapy compared to surgical intervention.[52]

In light of the lack of follow up data and confounding factors from radiation therapy imaging, risk is generally assessed through the use of radiation induced cancer risk estimation models. These models are based on data from radiation workers and the atomic bomb survival data.[43] This data is controversial for low doses due to the imprecisions mentioned above. This leads to many conflicting findings at low doses. As radiation risks are more readily determined at high doses low radiation dose risks can be determined by means of extrapolating this data. The commonly used linear no-threshold relationship implies proportionality between dose and cancer risk. The approach is based on the premise that damage to DNA from in-vivo studies appears linear between 1 mGy and 100 Gy.[50,53] The

linear no-threshold model is used in radiation protection and assumes that any dose of ionizing radiation can initiate the carcinogenesis. In order to estimate risk based on this model the effective dose descriptor can be used. This quantity will be covered later in this chapter.

2.6.2 Indirect dose measurement

Indirect measurements are output measurements that can be performed to benchmark the radiation output of the CT procedure. They do not represent the dose received by a patient. Indirect measurements generally rely on the use of single parameterised index.

CTDI

The most commonly used index is the computed tomography dose index (CTDI).[5,33] The CTDI is a radiation exposure parameter for conventional CT scanners. It quantifies the average absorbed dose for a single axial slice of a CT scan.[5,32,33,54] The CTDI is quantified using the following equation:

$$CTDI = \frac{1}{NT}\int_{-\infty}^{\infty} D(z)dz \tag{2.7}$$

Where N is the number of transverse slices acquired during a scan
T is the thickness of each transverse slice
D is the radiation dose profile along the z-axis

From observing the integral boundaries in equation 2.7 it is clear that measuring the average dose profile over an infinite range is not practical to measure. The CTDI is typically measured with a 100 mm long ionisation chamber to give the $CTDI_{100}$.[5]

$$CTDI = \frac{1}{NT}\int_{-50mm}^{50mm} D(z)dz \tag{2.8}$$

The $CTDI_{100}$ is measured in an acrylic, cylindrical phantom. The CTDI phantom comes in two sizes: head (16 cm diameter) and body (32 cm diameter). Both phantoms are 15 cm long. Size standardisation is used in these phantoms for reference dosimetry. $CTDI_{100}$ measurements are performed in the centre of a CTDI phantom. But there are a number of orificies which can be used to extend the CTDI index.

2.6.2.1 $CTDI_w$

$CTDI_w$ is a weighted CTDI index. It is calculated using five measurement points in a CTDI phantom, one in the centre and 4 at the periphery. The measurement points are weighted using the following equation

$$CTDI_w = \frac{1}{3}CTDI_{100,centre} + \frac{2}{3}CTDI_{100,periphery} \tag{2.9}$$

Equation 2.9 can be applied to a series of adjoining helical or axial scans.

2.6.2.2 CTDI limitations

The CTDI measurements are made up from both primary and scattered radiation in the CTDI phantom. For conventional CT the primary beam will be measured but scattered radiation is underestimated. The scattered radiation field extends throughout the length of the CTDI phantom and into the surrounding air. The 100 mm length ionisation chamber will therefore underestimate the scattered radiation component. An IAEA report found that using the $CTDI_{100}$ collects only 82% and 63% of the scan dose for the head and body phantoms, respectively.[55] Mori et al. found that, for a 2 cm beam width, the CTDI phantom length needed to be doubled to measure 90% of the dose. When compared to the use of a 450 mm ionisation chamber the $CTDI_{100}$ was found to underestimate dose by as much as 50%, irrespective of beam width.

Extension of the CTDI concept to large field scanning systems such as CBCT provides further limitations for the concept. The CTDI is applied to quantify the integrated dose over a couch translation in the z-axis. A CBCT scan is taken in one rotation around the patient and no couch translation is applied. The beam widths employed in z-axis also exceed the size of the CTDI phantom. This leads to large underestimations in the scatter dose profile when measured with the 100 mm ionisation chamber.[38,56] Studies have shown that as beam width increases, the weighted dose index $CTDI_w$ decreases. Over a large field there is also less uniformity in a beam and CTDI measurement can not provide an accurate representation.

A number of methods have been applied to extend the CTDI concept to cone-beam CT scanners. For example, Amer et. al derived the cone-beam dose index (CBDI) which uses the same pencil ionisation chamber and CTDI phantom but evaluates the dose to the central 100 mm portion rather than the entire beam width. Many alternative configurations have been proposed for CBCT dosimetry. The point that is made in this work, however, is that these indicies are indirect measures and do not provide information on absorbed dose received by a patient.

2.6.3 Direct dose measurement

Direct dose measurements have a number of implementations in radiology and radiation therapy. As they are related to patient doses the measurements should be performed in-vivo. Direct measurements can be performed using a large range of radiation detectors. These includes TLDs, optically stimulatd luminiscent dosimeters (OSLD), or diodes. Given the practical and ethical limitations of performing in-vivo dosimetry, direct measurement studies can be performed in anthropomorphic phantom volumes or by computational simulations.

2.6.3.1 Effective dose

Measuring absorbed dose alone is not sufficient to assess long term development of cancer. The mechanisms of radiation-induced cancer and genetic damage rely on the *type of radiation* depositing the dose and the *type of tissue* being irradiated.

The ICRP protection quantities, equivalent and effective dose, are dose descriptors that sum the absorbed dose to organs to provide a single number for comparing with dose limits and constraints for low dose x-ray procedures. The dose descriptors are intended to provide a correlation between whole-body radiation exposure and stochastic effects.

There are three steps involved in the calculation of effective dose. Firstly, the absorbed dose to organs and tissues is determined in Gy. As different radiation types differ in

their ability to cause biological damage the next step involves calculating equivalent dose. Equivalent dose weights different radiation types in their ability to cause cancer per unit dose. It is derived from the following equation:

$$H = \sum_{R} W_R \times D_R \tag{2.10}$$

Where D_R is the absorbed dose from an exposure to a type of radiation, R multiplied by its biological weighting factor, W_R. The result is expressed in Sieverts (Sv). For x-ray exposures the biological weighting applied to the dose is 1. So for a CBCT exposure the equivalent dose and absorbed dose are numerically equivalent. The final step of calculation invovles the summation of equivalent doses to differnet tissues, multiplying each by a tissue weighting factor.

$$E = \sum_{T} W_T \times H_T = \sum_{T} W_T \times \sum_{R} W_R \times D_{T,R} \tag{2.11}$$

Where W_T represents a weighting factor for a specific tissue of a human organ and H_T represents the equivalent dose received by that organ. The tissue weighting factor represents the cpntribution of each tissue to total detriment from a whole-body irradiation. Effective dose is also determined in the quantity Sieverts (Sv). The concept of effective dose is intended for reference models and not to individual subjects. The atomic composition of anatomy used in anthropomorphic phantoms can be standardised. For a standardised phantom the ICRP tissue weighting factors can be used (figure **??**).

Effective dose has been calculated for the XI scanner in two differnet studies. A study by Pyone et al.[57] determined effective doses for the XI CBCT scanner using cone beam dose index measurements. The imPact CTdosimetry software was used in this study. The software was originally designed for fanbeam CT and characterises CT scanners by the ratio of peripheral to central $CTDI_w$ and central to in-air $CTDI_w$ measured in a CTDI phantom. From these quantities it uses a empirical factors from Monte Carlo calculated data to derive organ doses for an ICRP humanoid phantom. Pyone et al. extended the imPACT software to CBCT by calculating $CTDI_w$ from CBDI measurements. Their

study examined the three main scan protocols for head, thorax and pelvis imaging. The effective doses for head, thorax and pelvis imaging were 0.1 mSv, 2.4 mSv, and 4.9 mSv, respectively (table 2.1). The study makes no mention of the scan parameters used to conduct this analysis.

A small study by Hauri et al. examined the effective dose from different XI pelvis imaging protocols using experimental measurements.[58] They found that the effective dose for standard pelvis CBCT imaging was 5.4 mSv (table 2.2). The study was carried out using TLD measurements at 183 measurement locations in the whole body RANDO phantom. Only the dose to the gonads could not be measured and was instead estimated.

2.6.3.2 Monte Carlo methods

As stated previously organ doses can be difficult to measure in-vivo or by other experimental methods. The use of detectors with resolution and spatial limitations makes some absorbed dose information hard to collected. Monte carlo methods are used to simulate photon transport through space, calculating absorbed dose based on the fundamental interactions of photons with matter. MC simulations possess all the qualities of an ideal radiation detector list in section 2.5. Doses can be measured with effectively unlimited resolution and the dismissal of spatial limitations. The dose deposition can be scored across a region of interest at any location within a simulated environemnt. Computational phantoms can be constructed on CT image datasets to provide retrospective dose analysis. Monte Carlo simulations can be performed accurately if the the transport parameters in the model are akin to reality. Detectors are used to verify the accuracy of the simulation parameters for both relative and absolute dosimetry.
An extensive explanation of Monte Carlo methods and how they are applied in this work is given in chapter 3.

Table 2.1: Organ and effective doses for XI scan protocols. The doses were evaluated by Pyone et al using the ImPACT CT dosimetry software

	Head	Thorax	Pelvis
Organ dose (mGy)			
Gonads	0.01	0.00	19.00
Bladder	0.00	0.00	34.00
Esophagus	0.00	10.00	0.00
Liver	0.00	0.44	0.13
Thyroid	0.42	0.76	0.00
Bone surface	0.95	3.10	6.10
Brain	2.50	0.04	0.00
Salivary glands	2.50	0.04	0.04
Skin	0.23	1.00	4.40
Bone-marrow (red)	0.22	1.60	4.00
Colon	0.00	0.02	9.30
Lung	0.02	5.70	0.01
Stomach	0.00	5.70	0.20
Breast	0.00	6.60	0.02
Remainder	0.25	1.40	3.10
Total effective dose (mSv)	0.1	2.4	4.9

Table 2.2: Hauri et al[58] examined the effective dose from pelvis CBCT imaging from the XI scanner.

	Pelvis
Organ dose (mGy)	
Bone marrow	4.49
Colon	6.09
Lung	0.190
Stomach	0.277
Breast	0.215
Gonads	23.8
Bladder	20.0
Oesophagus	0.135
Liver	0.468
Thyroid	0.0875
Bone surface	4.49
Brain	0.0526
Salivary glands	0.0695
Skin	17.7
Remaining tissues	9.23
Total effective dose (mSv)	5.4 ±0.27

*adrenals, extrathoracic region, gall bladder, heart, kidneys, lymphatic nodes, muscle, oral mucosa, pancreas, prostate, small intenstine, spleen, thymus

Table 2.3: ICRP recommendations for effective dose tissue weightings[59]

Tissue	w_t
Gonads	0.08
Red bone marrow, Colon, Lung, Stomach, Breasts, remaining tissues*	0.12
Bladder, Liver, Esophagus, Thyroid	0.04
Skin, Bone surface, Salivary glands, Brain	0.01

*adrenals, extrathoracic region, gall bladder, heart, kidneys, lymphatic nodes, muscle, oral mucosa, pancreas, prostate, small intenstine, spleen, thymus

3 Monte Carlo beam model of the Truebeam XI system

Monte Carlo (MC) simulation is the gold standard for performing radiation transport calculations.[3,60] MC methods provide capabilities for solving radiotherapy problems that can not be attained by experimental or analytical methods.[60,61]

A MC approach was taken to study the dosimetry of the Truebeam XI scanner. The XI contains multiple components to shape and modify intensity of the x-ray beam of the scanner. Each of these components had to be correctly modelled in order to provide a valid beam model of the system. The x-ray spectrum is the first component that must be validated. The remaining components are then included in constructing a beam model.

This chapter contains a brief introduction to MC simulations before detailing the work performed to model the XI system. This introduction covers fundamental concepts, different packages and techniques for radiation therapy transport problems and the estimation of uncertainty from MC simulations.

3.1 Introduction to Monte Carlo

The MC method is a statistical operation involving the repeated random sampling of a system to obtain numerical results. MC methods are applied to modelling physical and mathematical systems where the probability of different outcomes are not easily predicted due to the intervention of random variables. This makes the MC method suitable in application to radiation transport problems.

3.1.1 Random number generation

The idea of randomness in MC simulation is not entirely in line with the mathematical definition. Sampling in MC calculation is performed using a sequence of randomly generated numbers. MC algorithms use a procedure known as random number generation (RNG). RNG produces uniformly distributed random numbers over a defined interval (usually [0 1]). This process is not truly random as a procedure used by a computer is inherently deterministic.[62] The correct terminology used to describe the process is pseudo random number generation. Pseudo-RNG is a more practical method than using true random number generation for sampling sequences. This is due to reusability and storage considerations for these sequences.[60,62] A sequence must appear *sufficiently* random. As such there must be no evidence of correlation between the numbers. This means that the sequence of numbers must be sufficiently large so as not to be resused. The number of primary photons simulated can be on the order of billions. RNG algorithms must have a sufficiently large generation cycle to far exceed the number of generated primaries.[61]

3.1.2 Probability distribution

Random number sequences are used in MC sampling to draw random variables from probability distribution functions (PDFs). PDFs are weighted functions which represents an underlying physical process in a MC system. They provide a list of possible outcomes of a random variable from a given process. In radiation transport problems these variables may be photon direction or momentum as they traverse a medium. Essentially in MC simulation a sequence of random numbers are mapped to a PDF and are used to obtain the random variables needed to represent particle transport phenomena.

Cross sections

The interaction experienced by a photon in a medium depends on the cross section of the medium. The cross section is a description of the probability of a collision between

two particles interacting under certain conditions. Simulated photon cross sections are based on theoretical calculations and evaluated data.[63] In MC simulation cross sectional data is selected based on the photon energy examined. The data used will determine the probability distribution for photon interactions in a given medium.

3.1.3 Photon transport simulation

After being drawn from PDFs the sampled random variables are used in MC numerical integration. Essentially the results obtained from MC calculations are the outcome of this numerical integration. The MC method is suited to the evaluation of integrals which an analytical solution can not be attained for. MC methods are applied to integrals which model physical and mathematical systems with many coupled degrees of freedom.[64] These integrals have multiple dimensions to solve across and complicated boundary conditions. Radiation transport problems requires numerical integration to solve coupled Boltzmann transport equations (BTE). The degrees of freedom in the coupled BTEs are theoretically unlimited due to infinite number of possible secondary photons and electrons that can be produced. MC methods use a time-independent linear Boltzman transport equation (LBTE) to solve radiation transport problems.[61,64–66] The LBTE is a set of partial differential equations that determine the spatial and energy distributions of photons and electrons. The LBTE for photon transport is represented by the following

$$\hat{\Omega} \cdot \vec{\nabla}\Phi^{\gamma} + \sigma_t^{\gamma}\Phi^{\gamma} = q^{\gamma\gamma} + q^{e\gamma} + q^{\gamma} \tag{3.1}$$

Where Φ^{γ} is the photon (γ) fluence, σ_t^{γ} is the total photon cross section, and $\hat{\Omega}$ is a unit direction vector. The right hand side of equation 3.1 contains the source scatter terms. q^{γ} is the primary photon source term, $q^{\gamma\gamma}$ represents scattered photon-to-photon interactions, and $q^{e\gamma}$ represents scattered photon-to-electron interactions.
Electron (e) transport is given by the following LBTE

$$\hat{\Omega} \cdot \vec{\nabla}\Phi^{e} + \sigma_t^{e}\Phi^{e} - \frac{\partial}{\partial E}(S_R\Phi^{e}) = q^{ee} + q^{e\gamma} + q^{e} \tag{3.2}$$

Where S_R is the restricted collisional and radiative stopping power of electrons.

The LBTE approximation does not model the self interaction of photons and only considers scatter in a medium. Under this approximation photons can be independently simulated one after another. This lowers the computational requirements by decreasing the amount of memory required to perform simulations.[64]

Photons are continuously sampled as they traverse a medium. As the photon interacts both equations 3.1 and 3.2 are used to solve the local electron fluence, Φ^e. Dose is then evaluated by the following integral

$$D = \int_0^\infty \Phi^e S_R dE \tag{3.3}$$

Where ϕ^e is the local electron fluence, S_R is the material specific stopping power, and E is photon energy.
Dose is scored in MC simulations as mean value per incident particle from the primary source. Dose distributions are aggregated as a simulation proceeds and a dose grid is output for analysis.

3.2 GEANT4 Application for Tomographic Emissions

GEANT4 Application for Tomographic Emissions (GATE) is one of the many MC codes available for radiation transport simulation. GATE is an application based off the GEANT4 simulation toolkit. The GEANT4 MC code was originally developed by CERN for high-energy photon physics applications. It is an extensively verified code system for radiation transport.[67] It is a object orientated programming language implemented in C++. For radiation specialists with no background in object orientated programming the time taken to learn this skill set can be prohibitive to using GEANT4. High-level scripting languages that overly GEANT4 can be used as an alternative. One such language is GATE.

GATE was first released in 2003.[67] It was originally intended to be used for positron emission tomography and single photon emission tomography applications. In the years

since its initial release simulation capabilities for CT and radiotherapy have been added.[68] Since then it has been used in a number of studies for imaging and dosimetry applications in medical physics.[40,68,69]

A number of MC codes purposed specifically for radiation therapy applications are available. These include BEAMnrc, TOPAS, and XVMC.[70] GATE possesses a number of features that may favour its use over alternative code systems. GATE inherits a number of these features from GEANT4 that make it useful for not only radiation therapy, but also dosimetry and imaging problems. The code has a high degree of flexibility for the input of simulation geometries. This provides a user with more configurations options when fine tuning a beam model. Dose 'actors' are used to simplify the handling of dose scoring. GATE includes a voxelised source input which is easy to parameterize and eliminates the need to use a phase space file.[67,70,71] An inbuilt virtual clock allows the simple simulation of time-dependent phenomena (e.g. gantry rotation).

A recognised disadvantage when using GATE for radiation therapy is the simulation efficiency compared to other established codes.[70] This is due to a lack of variance reduction techniques (VRTs). VRTs help speed up simulation times without the loss of calculation accuracy. The most recent version of GATE (version 8) includes a number of VRTs that greatly improve simulation efficiency for modelling low energy electromagnetic processes. These techniques will be examined in section 3.4

GATE simulations are run from a primary job file or 'macro'. Smaller macros may be linked to the primary. Each macro contains an ordered list of scripted commands to establish a component of the simulation. For radiotherapy and dosimetry the commands describe the following components: Geometry of the beam model and phantom, dose scoring grids used, physics processes applied, source description and execution options. When a simulation is run a series of messages are relayed to the user to tell them the status of the aforementioned aspects of the simulation. The messages allow a user to

troubleshoot a failing simulation. At the end of a simulation the result from scoring grids and other output variables are stored in individual files for analysis.

3.3 Photon interaction processes

A photon may interact several times before depositing all of its energy. Interacting through a variety of photon interaction processes, the photon transfers its energy to charged particles in the medium. The interactions can be simulated using the total cross section data mentioned in section 3.1.2. The interaction length of a process is the mean distance travelled by a photon during an interaction

$$\lambda = \left(\sum_i n_i \cdot \sigma \right) \tag{3.4}$$

where σ is the cross section of the process for an atomic component n of a medium. The interactions considered in this work are the photoelectric effect, Compton scattering, and Rayleigh scattering. The cross section for Thomson scattering is too small for low energy processes to be considered here.

3.3.1 Photoelectric effect

During the Photoelectric effect a photon is completely absorbed and transfers all of its energy to an orbital electron. If the energy exceeds the binding energy of the electron it is ejected from its shell. The energy of the outgoing electron is

$$E = hv - L \tag{3.5}$$

Where hv is the energy of the photon and L is the binding energy of the electron. The vacancy will lead to a cascade of electron transitions from the outer shells to the inner shells. These transitions will produce a cascade of emissions such as characteristic X-rays, Auger electrons, or Coster-Kronig electrons. The photoelectric effect cross section depends on the photon energy and atomic number, Z, of an atom. The photoelectric cross section is tied to these two variables by the following proportionality:

$$\alpha \frac{Z^3}{E^3} \tag{3.6}$$

As the atomic number, Z, of a material increases and photon energy, E, decreases the likelihood of the photoelectric effect increases rapidly.

3.3.2 Rayleigh scattering

Rayleigh scattering, or coherent scattering, occurs when the binding energy of an electron is similar to the incoming photon energy. During the interaction all the electrons of an atom contribute so that momentum is conserved. The photon is deflected and no energy is transfered to the target. Scatter is mainly forward-directed and coontributes less than 10% to the relative interaction cross sections in tissue and water (Figure 3.1)

3.3.3 Compton scattering

Compton scattering, or incohorrent scatter, will occur when the incoming photon energy is greater than or equal to the binding energy of the electron. The interaction results in the electron being ejected from its atomic shell and the photon being scattered. TThe energy of the scattered photon is the difference between its initial energy and the binding energy and kinetic energy of the ejected electron. The Compton cross section is dependent on the electron density and photon energy. The Klein-Nishina treatment of the Compton differential cross section is based on the assumption that the electron is free and stationary. However this assumption is invalid for low energy processes where binding effects and more significant.[72]

3.4 Variance reduction techniques

Variance quantifies how far a set of numbers are spread out from their average value. The error variance given in a MC simulation is σ^2/N. An insufficient number of generated photons, N will lead to the output data being restricted by noise. The obvious way to reduce statistical fluctuations in the data is to increase the number of photons generated. During MC simulation photons are tracked one at a time which saves memory useage but can lead to long computation times. To avoid excessive computation times for an increased value of N there are techniques to reduce the variance, σ^2 of data output. Variance

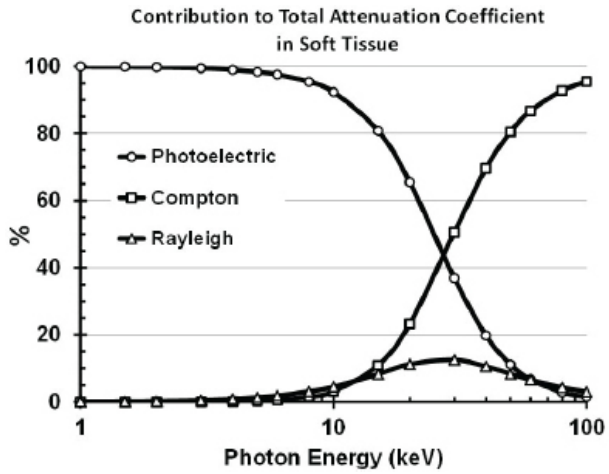

Figure 3.1: Relative interaction cross sections (i.e. attenuation coefficient) for the Photoelectric effect, Compton scattering, and Rayleigh scattering as a function of photon energy. Reproduced from NASEM (2015)[73]

reduction refers to a set of techniques that aid analogous (standard) MC simulations by reducing statistical fluctuations without changing the number of events simulated. Variance reduction techniques (VRT) are used in MC simulation to optimize transport parameters without losing a significant amount of calculation accuracy. In other words, correctly parameterising a VRT will result in a reduction in error variance without varying the validity of the physical processes being modelled. Some common VRTs are photon splitting, range rejection, and kerma approximation.[74]

3.4.1 Photon splitting

During MC simulation a lot of CPU time is wasted tracking photons that have little or no effect on the simulation output. Photon splitting can be applied to place more importance on photons that effect simulation output. In regions of the simulation with photon splitting applied an interacting photon is split into n_{split} subphotons, each carrying a weight of $1/n_{split}$. Subphotons are traced to the next interaction point. The interaction type is sampled and the electron distribution is generated. The output is weighted by n_{split}.

3.4.2 Range rejection

Without VRTs MC simulations will track particles until they leave the system boundary or deposit all their energy in secondary interactions. Range rejection is a technique that can be applied to any particle tracking. If a photon is transported with a range that does not exceed a cutoff parameter it will not be transported further and its remaining energy will be deposited locally. The value for the cutoff parameter selected for photon transport is chosen from one of two circumstances: 1) The range of the photon is small compared to the size of the voxel it is traversing or 2) The photon energy below the cutoff value will have a negligible contribution to the scored dose. Range rejection is one of the most effective VRTs for improving MC efficiency.[74,75] However, setting the range rejection cutoff too high will increase the statistical fluctuations of a simulation. The default range rejection threshold for GATE is 1 mm.

3.4.3 Kerma approximation

Low energy photons produce electrons with very short path lengths in tissue-equivalent mediums. Transport of secondary electrons may not be necessary to simulate for these small path lengths. Kerma approximation switches off electron transport and photons are transported by ray tracing methods through voxels. Kerma approximation techniques are one of the most effective VRTs used to improve MC efficiency for low energy x-ray simulations.[74,75] Kerma approximation VRTs are appropriate to use in a simulation provided the range of electrons released from a photon interaction is much less than the voxel resolution in the scoring plane.

Kerma approximation is implemented in GATE using the track length estimator (TLE) and split-exponential track length estimator (seTLE).[69,76] These are both included as dose scoring options available in GATE, making the TLE and seTLE options a hybrid of both dose scoring and VRT.

TLE assumes a continuous energy deposition from photon tracks. Ray tracing is a light

tracing technique that is used to simulate the average dose distribution expected from a large number of identical photons through the voxelised volume. Photon fluence is estimated in a voxel by the following:

$$\phi = \frac{L}{V} \tag{3.7}$$

Where L is the distance travelled through the voxel between collisions and V is the volume of the voxel. Given the assumption of charged particle equilibrium the absorbed dose is then estimated by:

$$D = \phi E \frac{\mu_{en}}{\rho} \tag{3.8}$$

where $\frac{\mu_{en}}{\rho}$ is the mass-energy absorption coefficient and E is the energy of the photon. The seTLE dose actor combines splitting with the TLE technique. The splitting strategy is carried out as mentioned in the above section. When using seTLE, however, both primary and secondary photons are split into n_{split} subphotons. seTLE provides similar levels of accuracy to the TLE while increasing the efficiency by a factor of between 13 and 15.[76]

3.5 Expression of MC uncertainty

For experimental measurements it is possible to calculate uncertainty based on the methods given in the guide to the expression of uncertainty in measurement (GUM).[77] The methods express an uncertainty $U_c(y)$ in terms of a measurand y. An equation that expresses y is a function of input quantities, x_i. The combined uncertainty is given by

$$u_c(y) = \sqrt{\sum_{i=1}^{N_i} [u(x_i)]^2} \tag{3.9}$$

where $u(x_i)$ represents the standard uncertainties of all input quantities. In practices such as radiation oncology where health and safety are a concern expanded uncertainties can be given for a measurement.

$$U_p = k_p u_c \tag{3.10}$$

where k_p represents the coverage factor corresponding to a confidence level p. NIST primary standards for all dosimetric quantities in medical physics use k=2, corresponding to an interval with a 95% level of confidence.
The standard uncertainty of an input quantity $u(x_i)$ must be represented by a type A or type B evaluation method. Type A uncertainty is evaluated by statistical methods. GATE simulations include a statistical uncertainty value that is scored for each voxel in a scoring grid. These uncertainties are reduced by increasing the number of primary photons generated or employing variance reduction.

Type B uncertainties are evaluated using methods other than statistical ones. There are several sources of type B uncertainty in MC simulations. These include influence from simulation geometry, radiation source, transport parameters used and the specific interaction cross sections used. Their influence is not evaluated in MC simulations.

MC calculations are performed using statistical modelling. A mathematical relationship between the MC result and randomised input variables cannot be easily attained. Evaluating type B uncertainties would require an extensive sensitivity analysis. This analysis is outside of the scope of this work and all MC uncertainties are reported as type A.

3.6 Methods

The GATE MC toolkit (version 8.1 - released 23/4/2018) was used to simulate the head of the Truebeam XI system. GATE v 8.1 was built from the GEANT4 (v 10.03) environment. Simulations were run on a workstation with a single 8 core Intel Xeon E5620 processor with a processor clock speed of 2.4 GHz.

The specification of components of the XI were given from manufacturer documentation. A schematic diagram of the XI head unit can be seen in Figure 3.2. The components that have an impact on patient dose are considered. They include the x-ray tube, collimators and any added filtration.

Voxelised phantoms were modelled using image data and require appropriate image navigation algorithms to determine how the image data is handled in the simulated environment. The ImageNestedParameterisedVolume algorithm was used in this work. The navigation algorithm supports both analyze and MetaImage image file formats.

GATE includes a large variety of physics models which are inherited from GEANT4. For this work the emlivermore package was used. The package uses cross sectional data from atomic shell cross section data rather than empirical cross section data due to the high dependence of the low energy processes on atomic shell structure.[63,78]

Atomic relaxation was also enabled. Atomic relaxation is a component of the emlivermore model which simulates the physics processes of x-ray fluorescence and Auger electron emission.[79]

The RNG algorithm used was the Mersene Twister (MT). the MT algorithm uses a cycle period of $2^{19937}-1$ when generating number sequences.[80] This number greatly exceeds the maximum number of primary photons that can be simulated in GATE, 2.2 billion. The MT algorithm pregenerates random number sequences for sampling rather than generating them on-the-fly. This leads to a reported 3 to 4 times reduction in total computation time.[61]

3.6.1 Benchmarking the GATE installation

It is difficult to create a reproducible benchmark test for MC simulations due to statistical fluctuations from random sampling. As stated in the previous chapter absorbed dose is scored as mean value per incident photon in MC simulations. For experimental measurements the number of photons generated are generally unable to be counted. Without the ability to count photons experimentally other methods are needed to validate a MC application.[81]

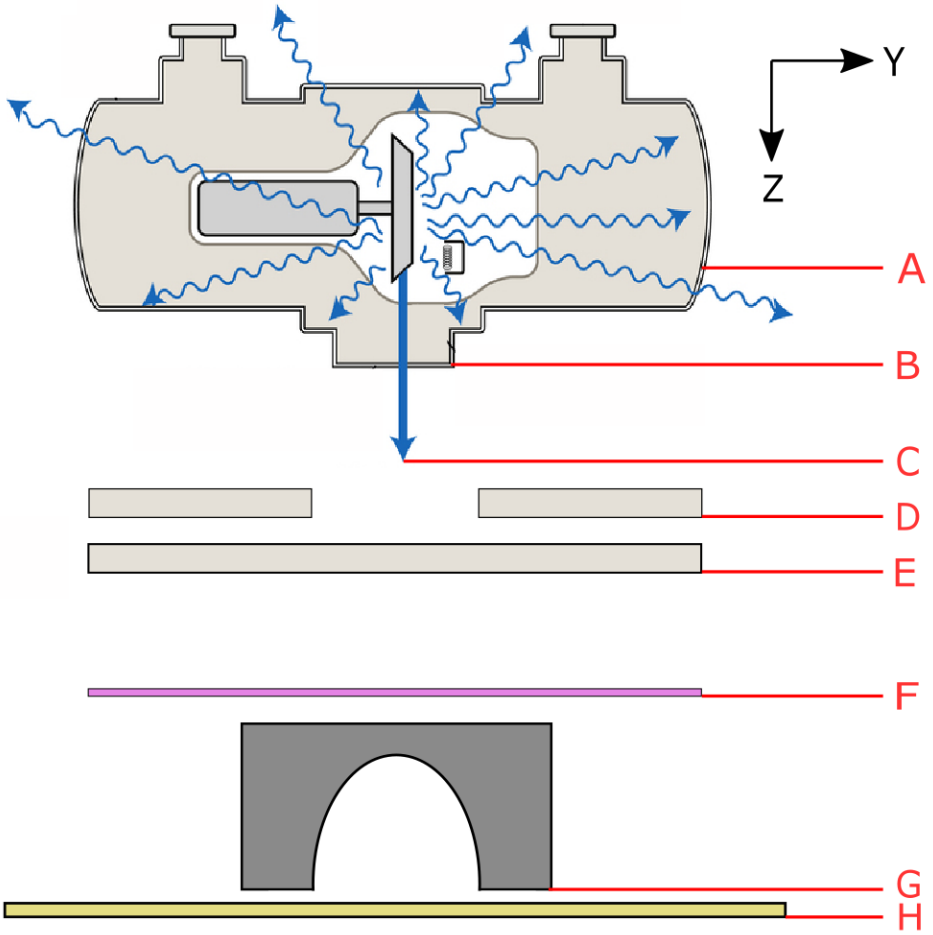

Figure 3.2: The internal components of the Varian Truebeam XI head unit. The major components are labelled A) x-ray tube B) x-ray tube window C) direction of beam travel D) upper (Y-axis) collimators E) lower (X-axis) collimators F) beam hardening filter G) Bowtie filter (representation only) H) detection cover

To assess the low energy dose scoring capabilities of GATE and verify correct installation a simple benchmark test was used. The test provides a theoretical dose scoring calculation benchmark for MC applications.

$$D = \left(\frac{E \times E_{electron} \times N}{m} \right) \tag{3.11}$$

Where E is the x-ray potential (V), $E_{electron}$ is the elementary charge of an electron

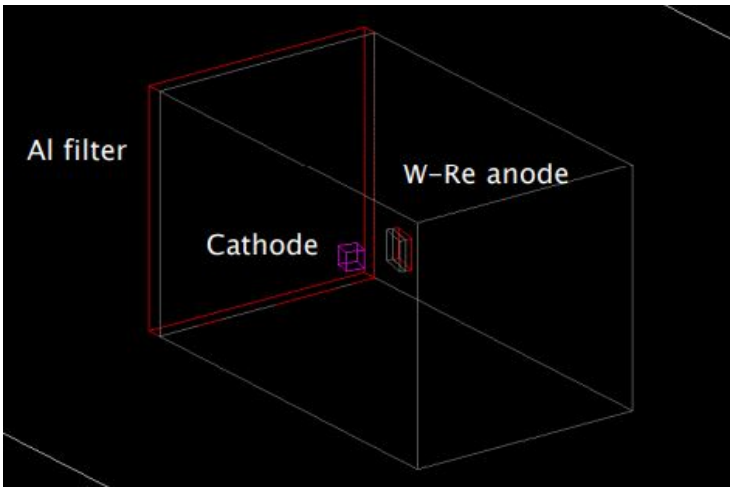

Figure 3.3: An OpenGL visualisation of the simulated x-ray tube.

(1.60×10^{-19}. J), N is the number of primaries and m is mass of the scored medium (kg). The density of water used to calculate the mass was 1000 kg/m^3. This is the value used in the materials list in GATE.

For the GATE simulation a 20 keV monoenergetic beam was placed at the centre of water medium. The dose was scored over a volume 30 cm x 30 cm x 30 cm. The resolution of the scoring plane was set to 1. 1000 primary events were generated and a single dose value was scored.

Both simulated and calculated dose values equated to 1.187x10$^-$13 Gy for the above parameters. The simulation was performed using the standard dose actor and the TLE option in GATE. The difference in values was 2×10^{-4}%.

3.6.2 Modelling the XI spectrum

The GS-1542 is a multi-energy diagnostic x-ray tube. It is used for radiographic imaging, fluroscopy, and CBCT. In this study the x-ray spectra used for CBCT acquisitions were simulated in GATE using manufacturer documentation. The spectr

The simulated environment included a voxelised source attached to a cathode, a Tungsten-

Rhenium anode, aluminium filtration, primary collimator, and an electromagnetic actor (Figure 3.3). A monoenergetic electron source was attached to the cathode. Both energies of 100 keV or 125 keV were used for the monoenegetic source. The position and angle of the voxelised source resulted in beam directed perpendicular to the face of the anode, which was offset at an angle of 14° from the direction of x-ray beam travel. The focal spot size on the anode face was 1 mm diameter to match the nominal focal spot size used for CBCT acquisition. VRTs were applied according to the recommendations given in Mainegra-Hing and Kawrakow.[82] Photon splitting was applied to multiply Bremstrahlung interactions in the anode. Bremstrahlung interactions were split into 1,000 subphotons. Photon and electron production thresholds in the anode material were set to 0.5 μm and 1.0 μm, respectively. Actors that stop photon and electron tracking were placed around the cathode and anode to prevent unnecessary tracking.

The total filtration of the GS-1542 x-ray tube is given as a range in terms of aluminium thickness. This considers both the inherent filtration due to the Beryllium window, tube housing and cooling oil and the physical aluminium filtration present in the tube. The aluminium thickness selected was 2.7 mm.

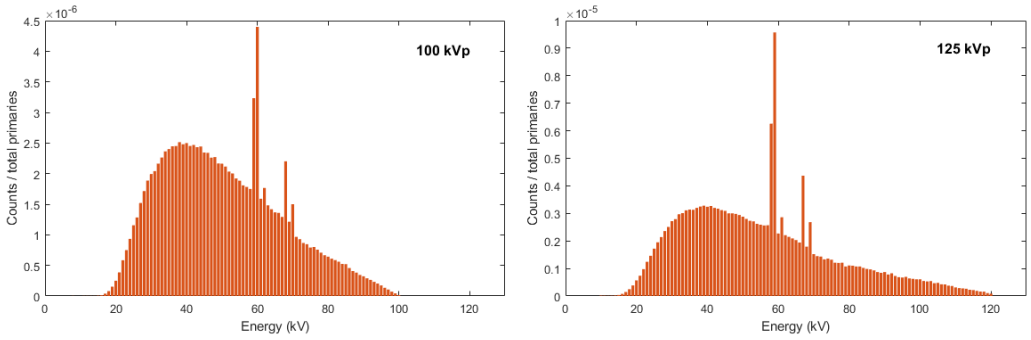

Figure 3.4: X-ray spectra simulated in GATE. The Monte Carlo output is given in total counts per bin divided by the total number of primary photons simulated.

An EM scoring grid was placed 100 cm from the focal spot. This was done to effectively eliminate the scoring of scattered radiation. The number of primaries was set to 2×10^9 for the electron source. The output spectrum was stored as a histogram and the bin width

was set to 1 kV. 2 billion primary photons were simulated to produce the spectra. The simulated spectra for 100 keV and 125 keV sources are shown in Figure 3.4. The x-ray spectra were comparable to those modelled in previous studies.[37] The validation of the x-ray spectra will be covered in the next chapter.

3.6.3 Beam model

All simulations in this study were run using a single, configurable macro. The following components were included in the beam model: source, blades (collimators), beam hardening filtration, bowtie filter, and detection cover. Manufacturer specifications included dimensions, distance from source, and material composition for all components.

The source was specified first in the macro as the position of the remaining components

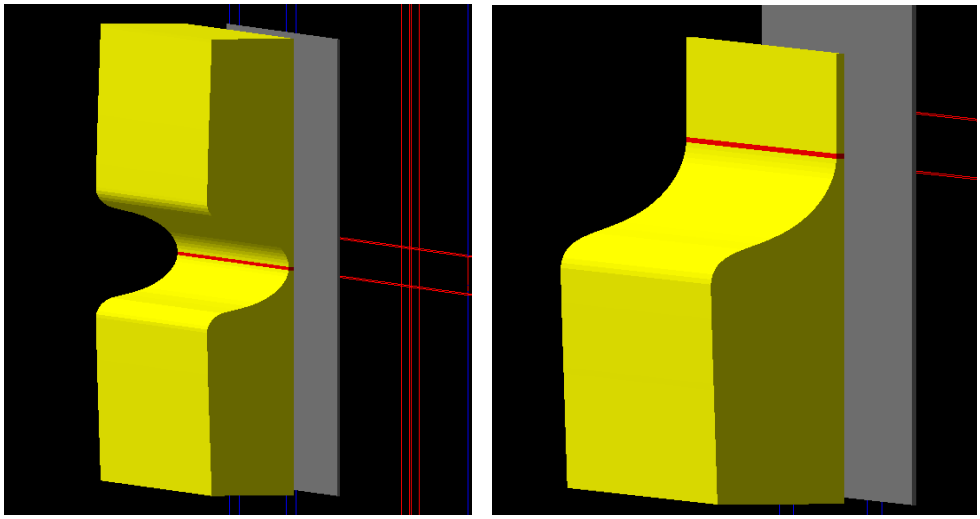

(a) (b)

Figure 3.5: Simulated representations of the bowtie filters used in the kV imager unit. The figure shows (a) the full bowtie filter and (b) the half bowtie filter. The central axis of the radiation beam passes through the red trapezoid. The gray sheet behind the bowtie filter is the titanium filter (otherwise known as the beam hardening filter). The x-ray beam moves from right to left.

are defined relative to its position. The voxelised source option was used to model the

source. The x-ray spectra in figure 3.4 were used to parametrise the voxelised source model. The source size was 1.5 mm by 1.8 mm

Beam collimation is achieved by two sets of adjustable lead blades. The first set defines

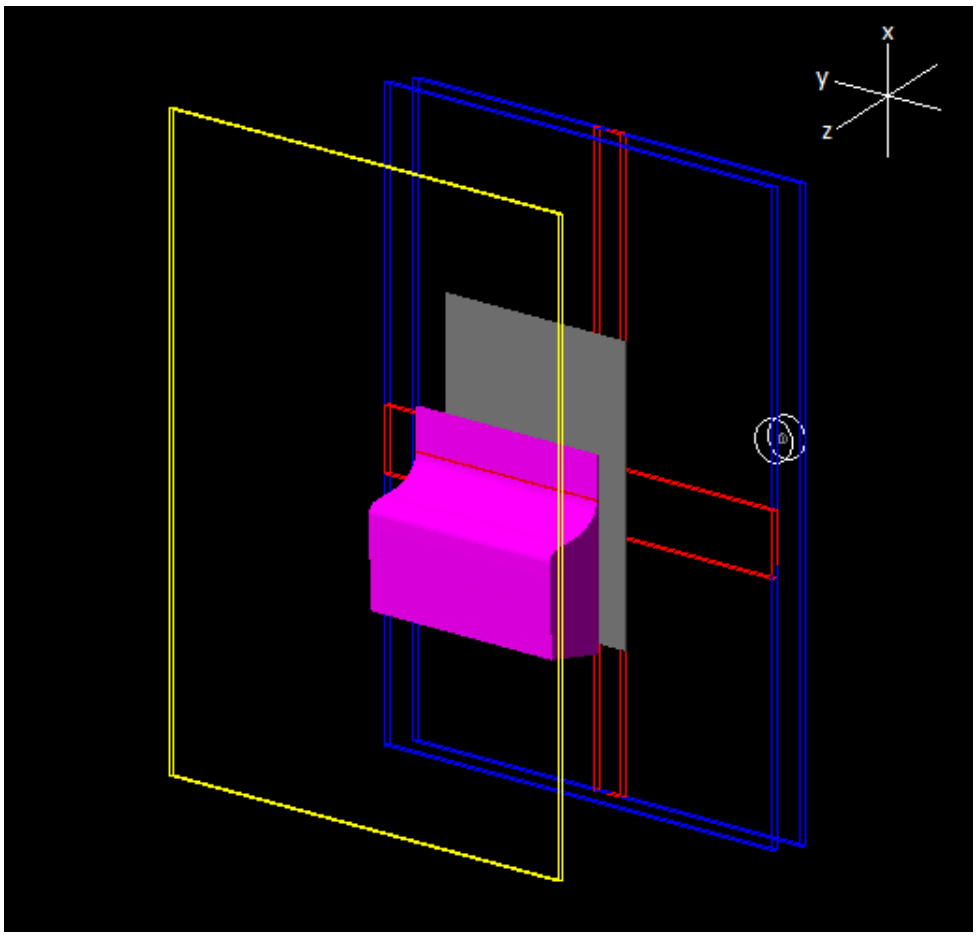

Figure 3.6: A visualisation in OpenGL of the simulated components of the TrueBeam x-ray imager. The axis used for modelling is included in the top right of the figure.

the field size across the anode-cathode direction. The second set defines the field size perpendicular to the anode-cathode direction. Each blade can open to a maximum of 20 cm. As such the largest field size achievable is 40 cm by 40 cm. Blade openings are defined at 100 cm SAD.

Further filtration of the x-ray spectrum takes place downstream from the blades. The

beam hardening filter provides preferential absorption of low energy photons. It is a high purity titanium sheet. Below this is the bowtie filter. The filters are made from an aluminium alloy. The filters are shaped in the direction perpendicular to the anode-cathode direction. Both the half and full bowtie filters, as simulated in GATE, can be seen in figure 3.5. Both filters were modelled as a series of 1 mm long trapezoids.

Below the bowtie filter is the detection cover. The polycarbonate structure makes up part of the plastic housing that protects the mechanical and electrical components of the XI. The entire beam model can be seen in figure 3.6

3.6.4 Gantry rotation

The Varian Truebeam has a 360 degree range of rotation. When the gantry head is up the indicated gantry angle is 0 degrees. Unlike fanbeam CT the rotating gantry of a linear accelerator does not include slip ring technology. Due to this it can only rotate 180° clockwise or counter clockwise from 0° (Figure 3.7). A full 360 degree rotation will start with the gantry head at 180° and end on 180E° (extended), or vice versa. The gantry can rotate up to 2-3° past the stop point for acceleration/deceleration.

Before modelling gantry rotation in GATE it was verfifed that the relationship between gantry angle and time was linear for a CBCT acquisition. A linear relationship is expected as the x-ray beam does not turn on until the gantry has accelerated to a constant velocity. To check the linearity the Sun Nuclear ArcCheck phantom was used. The ArcCheck phantom is a diode array for performing 4D measurements under radiation beams. The phantom includes an inclinometer that records the incidence angle of a radiation beam at each point of an acquisition.

Once the linearity between gantry angle and time was confirmed a model for gantry rotation was easy to implement in GATE. The rotation was modelled for the phantom/target

geometry instead of the beam model. The phantom/target was placed at the centre of the simulated environment and a macro was written to apply 0.5 degrees of rotation per time slice. For a 360 degree rotation 720 time slices were used. For a 200 degree rotation 400 time slices were used.

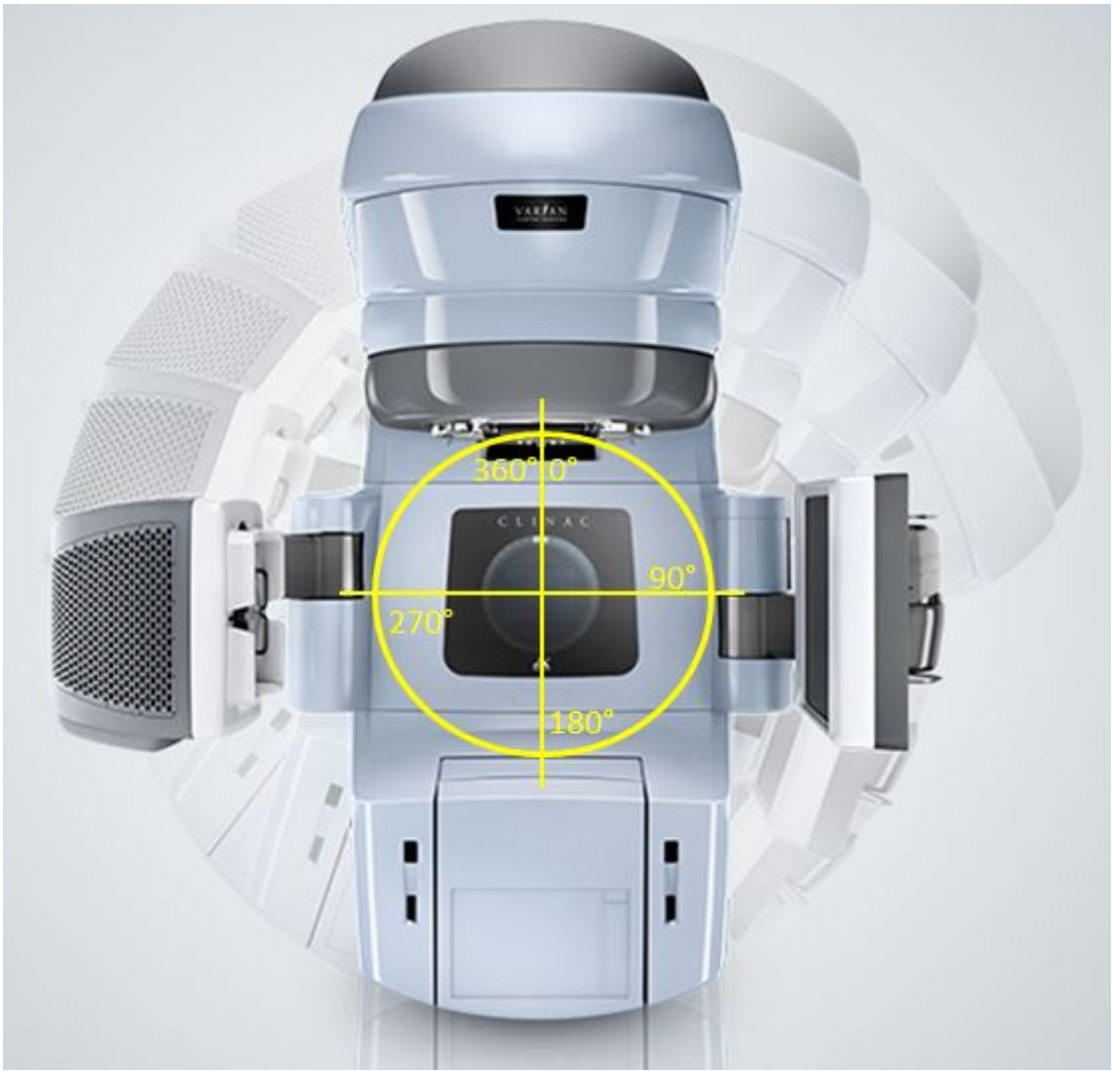

Figure 3.7: The rotation coordinates for a Varian linear accelerator. If 180° is reached through a counterclockwise rotation it is indexed as 180°E (extended).

4 Monte Carlo model validation with experimental measurements

In the previous chapter the a beam model for the XI scanner was constructed in GATE. The Monte Carlo (MC) model can be used to calculate absorbed dose for CBCT imaging. However, in order to validate the GATE model it had to be compared to experimental measurements. This includes comparisons in both simple and complex geometries. These comparisons are made to quantify any discrepancies in the GATE model for CBCT dose calculation. The discrepancies can be used to define limitations on the use of the model and quantify uncertainties on any findings made by simulations.

In this chapter uses experimental measurements to validate and calibrate the GATE MC calculations into absorbed dose. This involved comparing relative dosimetry in a water medium. Following this simulated results are calibrated against TLD measurements in both head and pelvis anthropomorphic phantoms.

4.1 Relative dosimetry comparison

Percentage depth dose (PDD) measurements were performed in a 1D scanning (1DS) water tank (figure 4.2a). Two 0.13 cm^3 CC13 (IBA Group, Louvain-La-Neuve, Belgium) scanning thimble ionisation chamber were used. These chambers have an uncertainty of $<2\%$ over the range of energies investigated.[83] One was placed in a motion-controlled chamber holder and the other was fixed at a point in air to be used as an output reference (figure 4.2b). The thimble chambers were connected to a fluke electrometer (Fluke Biomedical, Cleveland OH, USA).

A simulation was run with both simulated spectra (figure **??**) in a 10 cm x 10 cm field incident on a body of water 100 cm from the source. To verify the simulated spectra these

Table 4.1: Factory scanning parameters used for the anthropomorphic phantom measurements. "CCW" denotes a counter clockwise scan arc from . In this study CCW scans were performed between gantry 90° and gantry angle. Half and full bowtie filters are designated by "HBTF" and "FBTF", respectively. The titanium beam hardening filter is denoted "BHF".

	Head scan	Body scan
Tube voltage (kVp)	100	125
Tube current (mA)	15	15
Pulse duration (ms)	20	20
Exposure (mAs)	147	1074
Scan arc (deg)	200 CCW	360
Filtration	FBTF, BHF	HBTF, BHF
Blade openings:		
X1 (cm)	10.7	24.7
X2 (cm)	10.7	3.4
Y1 (cm)	14.0	14.0
Y2 (cm)	14.0	14.0

results were compared to experimental measurements. A 10 cm x 10 cm, 100 cm SSD depth dose measurement was made in the 1DS tank for both energies. The field size on the water surface was verified using the light projection field from the treatment head of the linac. The light field projected from the treatment head collimators was set to 10 cm x 10 cm. A mechanical front pointer was used to set the water surface to 100 cm from the source. The CC13 chamber was aligned to the central axis of the field. The gantry was then rotated 90 ° so the XI head unit was positioned above the tank. The blade openings of the XI were set to 10 cm x 10 cm. The field sizes for both the XI and the Truebeam treatment head are defined at 100 cm from the source. The bowtie and beam hardening filter were removed from the field.

Surface measurements for the PDDs were performed at the depth of the chamber radius (3 mm).[4,21] Measurements were performed in 2 mm increments for the first five points, after which 10 mm increments were used. PDDs were also measured for the beam arrangements used for CBCT imaging. The scanning parameters are shown in table 4.1.

Profile measurements were performed in a Blue Phantom 2 (IBA Group) 3D scanning (3DS) water tank (figure 4.2c). The tank is usually on a mechanical platform and can be adjusted to ensure the water level is aligned with the direction of chamber travel. Due to the inability to retract the XI detector panel while an x-ray beam is being produced the 3DS tank could not be wheeled in on its platform. Instead it was placed on the IGRT couch. The weight of the tank and the water on the couch could not exceed 100 kg. Due to this weight restriction the tank was filled to a depth of 10 cm. Because of this limitation PDDs could not be measured in the 3DS tank.

The water surface was positioned 100 cm from the x-ray tube focal spot. The XI source unit was positioned above the water tank (gantry at 90°). Static beam acquisitions were performed using the blade openings as seen in figure 4.5. The method used for imaging beam data acquisition is given by Ding et al.[17] Using the scanning parameters seen in

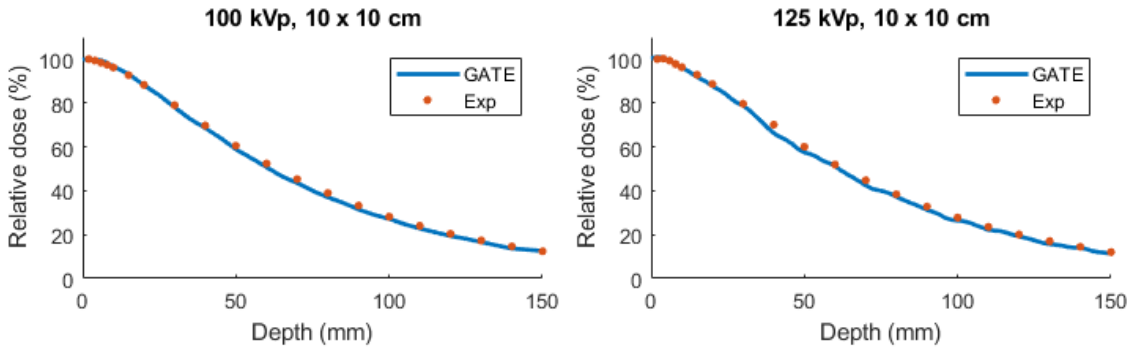

Figure 4.1: 10 cm x 10 cm depth doses and profiles were measured in the 1D scanning tank to verify the simulated x-ray spectra.

table 4.1 measurements were taken for 4 seconds per point. Profiles were measured with a resolution of 4 mm. Ionisation data was not converted into dose for relative dosimetry measurements. Profile measurements were performed with and without bowtie filters in place.

4.1.1 Results

Running simulations for 1×10^9 primary photons took 15 hours using the 8 core processor system. The simulated results were compared against experimental measurements. For the simulated results the statistical uncertainty was <1% at the point of normalisation. Experimental and simulated PDDs compared in a 10 cm x 10 cm field matched within 3% (figure 4.1). This comparison was the intial indication that the simulated spectra had been correctly modelled. PDDs and profiles for the head and body scanning protocols were compared at the reference depth, 2 cm (figure 4.3 and 4.4). Simulated and experimental PDD measurements showed good agreement and matched within 3%. Simulated and experimentally measured profiles matched within 10%.

Figure 4.7 shows the simulated and experimental x-axis profiles at 1 cm and 5 cm depths for the head scan protocol.

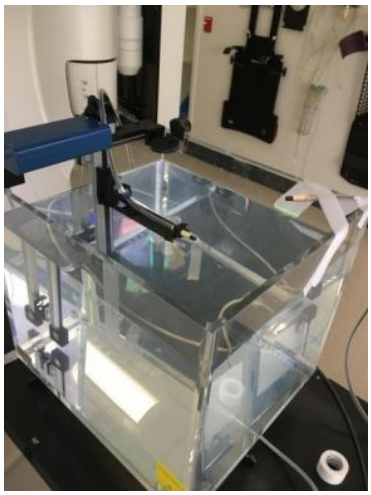

(a) 1DS water tank

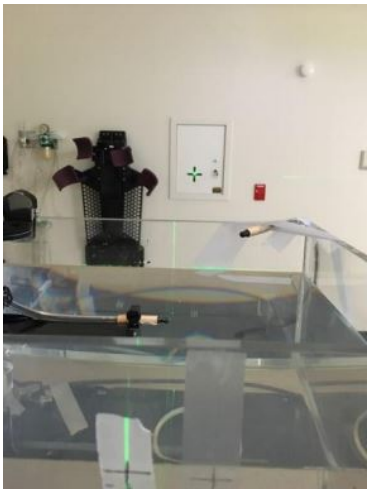

(b) Field and reference detectors

(c) 3DS water tank

Figure 4.2: Relative dosimetry was performed in two water-filled phantoms. Percentage depth doses (PDD) were measured using a 1D scanning water tank. Profiles were measured in a 3D scanning (3DS) water tank. The 3DS tank was placed on the treatment couch so it did not collide with the XI detector when the gantry was rotated. The 3DS tank could be filled to a maximum depth of 8 cm due to the weight restrictions on the treatment couch.

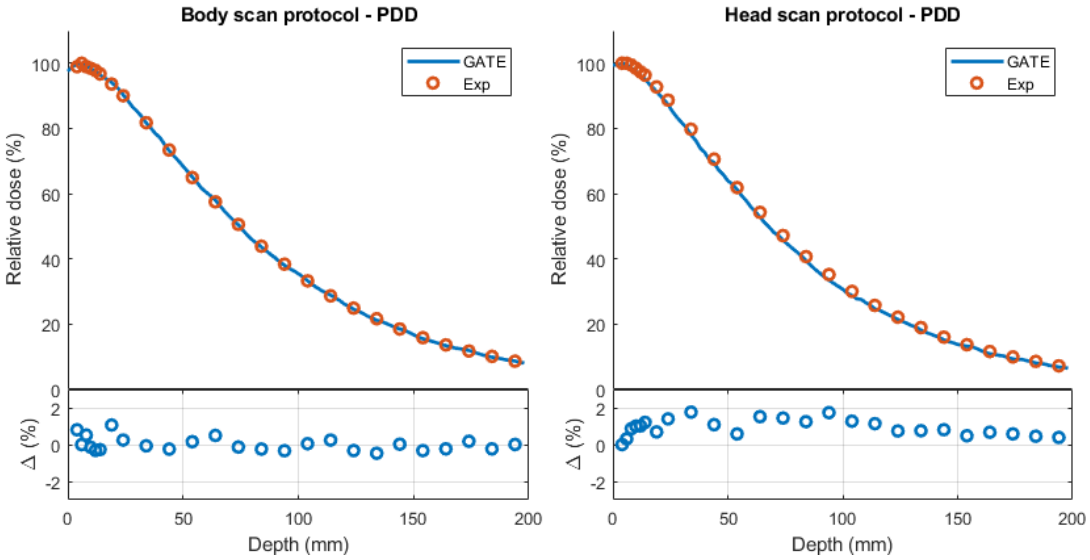

Figure 4.3: A comparison of simulated and measured depth doses for CBCT imaging protocols. Experimental measurements were performed in 2 mm increments until reaching a depth of 10 mm. After this 10 mm increments were used.

4.2 Absolute dose calibration

Dose calculations in GATE were matched with experimental measurements to assess their ability to model the relative dosimetry of dose deposition. The next step was to convert the GATE dose calculations into absorbed dose. To convert the calculations reference dosimetry measurements were performed

Half value layer

Narrowbeam geometry conditions were used to measure the first HVL of the 100 kVp and 125 kVp beam. This is the recommendation of AAPM TG-61. Narrowbeam geometry involves 4 components: an x-ray source, collimation, attenuating material, and an appropriate detector. A typical setup is pictured in Figure 4.8. An in-house acrylic jig was used to perform the HVL measurements. The jig can be seen in Figure 4.9a. A lead diaphragm was used to collimate the x-ray beam. the diaphragm was positioned 72.5 cm from the x-ray source. The collimator opening was a 3 cm diameter circle. Aluminium

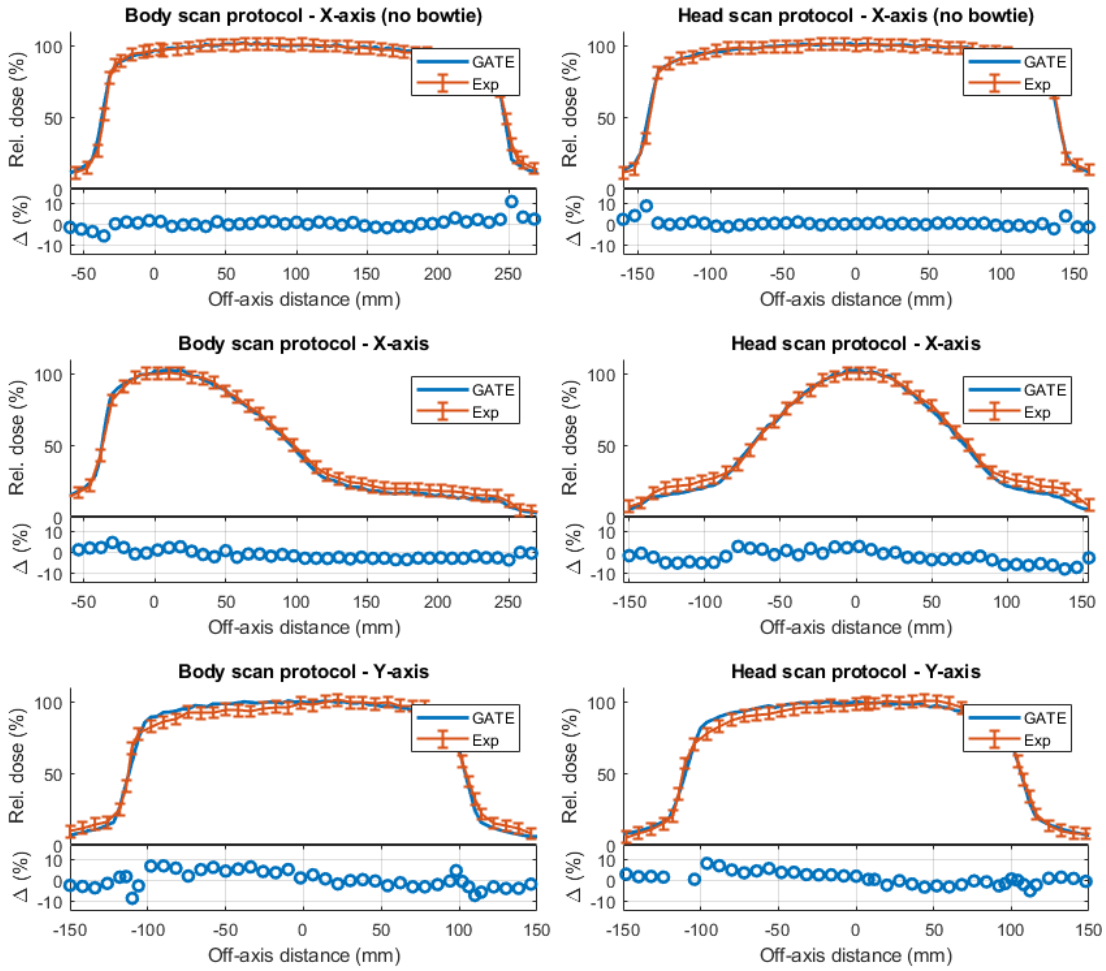

Figure 4.4: Comparison between GATE and experimental measurement dosimetric profiles. Comparisons are made with and without the bowtie filter. Profiles were measured at 2 cm depth. For x-axis profiles: X2 is in the negative direction and X1 is in the positive direction. For y-axis profiles: Y1 is in the negative (anode) direction and Y2 is in the positive (cathode) direction. All the experimental profiles have been re-sampled for clarity.

was used to attenuate the beam. The thickness of aluminium sheets used was 0.25 mm, 0.5 mm and 1.0 mm. The sheets were fixed in place against the lead diaphragm using two screws. The given purity was 99.9%. An FC65-G farmer-type ionisation chamber was used to measure air kerma rate. It was fixed roughly 50 cm from the diaphragm. As per

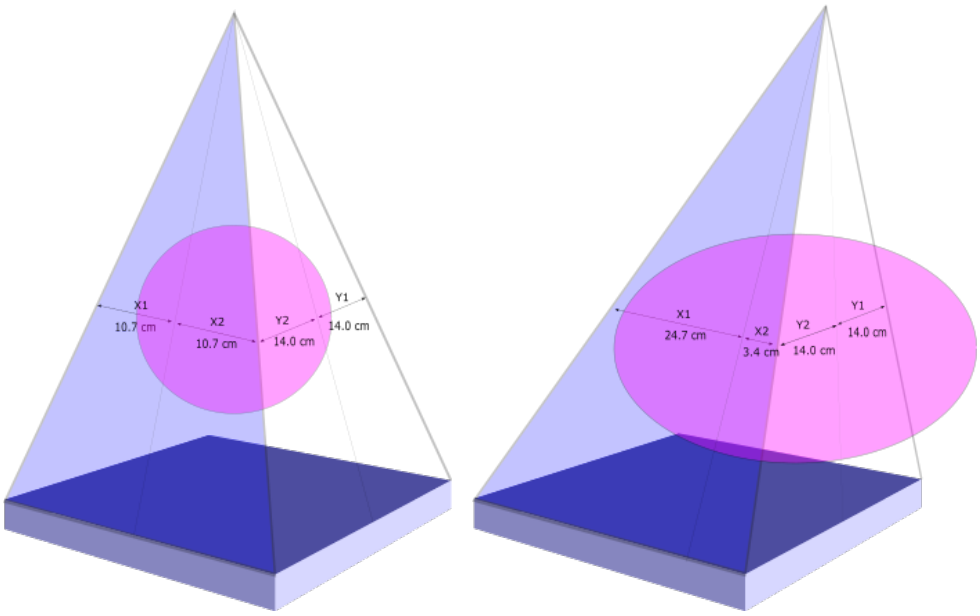

(a) Head scan protocol (b) Body scan protocol

Figure 4.5: The figure above illustrates the collimator positions used for CBCT imaging. The field sizes are defined at a distance 100 cm from the source. The imaged object sits between the source and the flat panel detector. The head scan protocol is used for smaller objects. The entire object is in the imaging field. During the body scan protocl the detector panel is shifted in the x1 direction. The X1 blade opening is increased to 24.7 cm while the X2 blade opening is reduced to 3.4 cm.

TG-61 requirements the chamber has an energy dependent response less than 5% over a tube potential range of 40 kV to 300 kV.

The ionisation chamber and source were aligned down the central axis of the x-ray beam. This was achieved using an external laser system (Figure 4.9b). To confirm the correct positioning of the chamber sensitive volume and anode XR-QA2 radiochromic film was placed behind the chamber. The film was exposed under the x-ray beam. The position of the chamber's sensitive volume and anode can be seen in figure 4.9c.

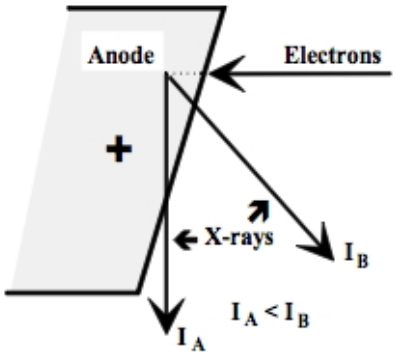

Figure 4.6: The heel effect decreases the intensity of an x-ray beam towards the anode side of the beam. X-rays emitted perpendicular to the anode-cathode axis will travel through a longer length of anode compared to those emitted perpendicular to the face of the anode (i.e. intensity I_A is less than intensity I_B)

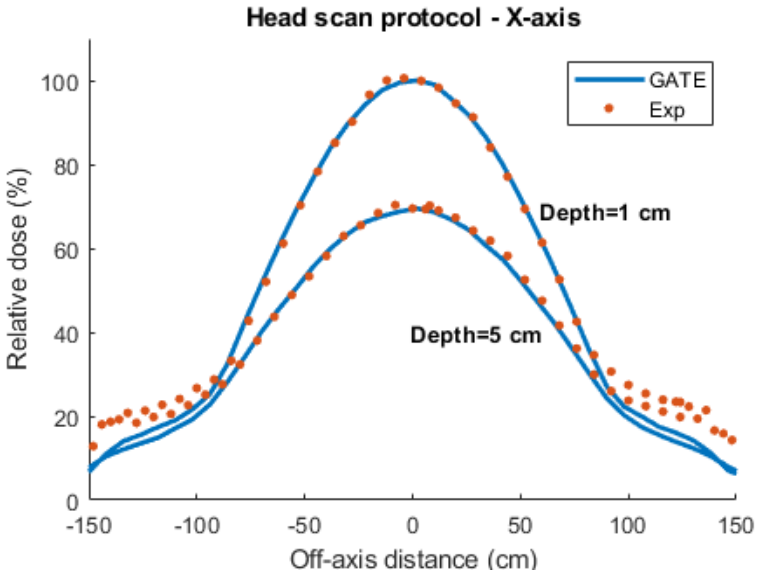

Figure 4.7: Comparison between GATE simulated and experimental results for profiles at 1 cm and 5 cm depth using the head scan beam configuration.

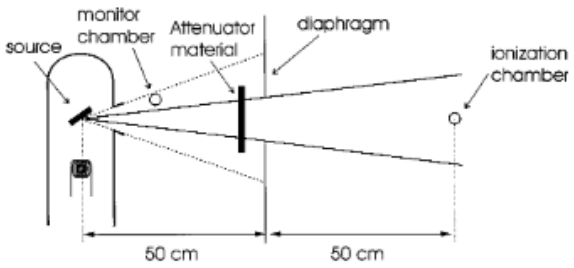

Figure 4.8: A narrowbeam geometry setup for HVL measurement. Included is the recommended spacing between the source, diaphragm, and ionisation chamber.

The exposures performed used 500 mAs and a 2x2 cm^2 field size (defined at isocentre). The beam hardening filter was used. Measurements were performed both with and without bowtie filters in field.
A stable kerma rate was measured from the unattenuated beam. Aluminium sheets were introduced incrementally. Measurements were performed until a sufficient aluminium was introduced to reduce the kerma rate below 50%.
The Black Piranha 455 CT Profiler (RTI Group, Mölndal, Sweden) was used to compare to the narrowbeam geometry values. The piranha can be used to measure a beam HVL in a single exposure without collimation or filtration. It is much less sensitive to scattered radiation than a typical farmer-type ion chamber.[84]

The detector was placed on the IGRT couch at 100 cm SSD. The field sizes used at 100 cm SSD were 4x4 cm^2 and 8x8 cm^2. The XI source was positioned above the detector. A continuous pulsed beam was delivered to the detector and a stable value was recorded. Varying the mAs of the pulsed beam had no effect on the recorded values.

4.2.1 TLD calibration

TLDs should be calibrated in the beam quality under investigation in attempts to eliminate any uncertainty in energy dependence. A batch of TLD-100 chip dosimeters (Harshaw, type TLD-100, Thermo Fisher Scientific Inc., Waltham, MA) were calibrated for both beam energies studied. There were 13 TLDs in each batch. 6 TLD pairs per energy

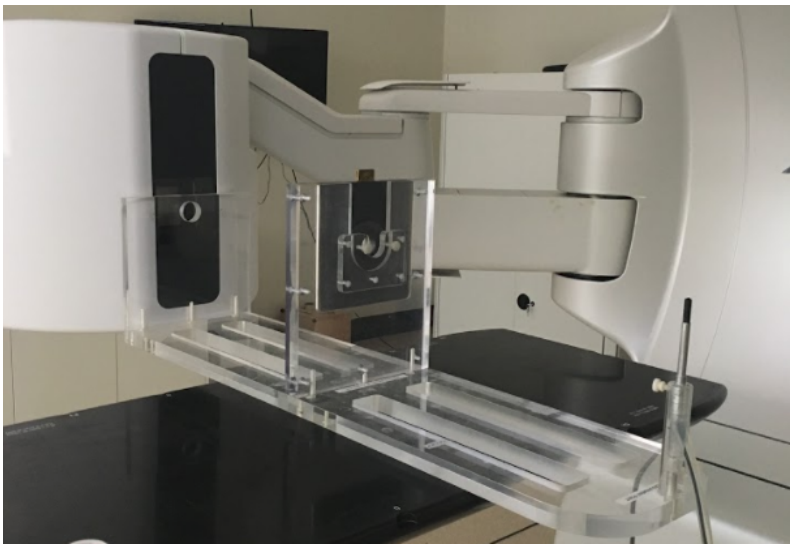

(a)

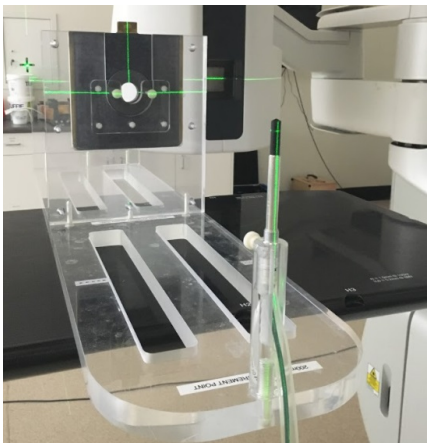

(b)

(c)

Figure 4.9: The setup used to measure beam quality. (a) A one meter long jig for measuring HVLs was used to determine the x-ray tube beam quality (b) external laser (c) radiochromic film

with a spare in each. A standard TLD readout protocol was performed using an automated TLD reader with hot nitrogen heating (Harshaw 5500; Thermo Fisher Scientific Inc.). The TLDs were read out at least an hour after being exposed. Before readout the TLDs are pre-annealed at 165°C. Then constant heating to a maximum temperature of 270°C is applied. This temperature is used to exceed all glow peak positions for TLD-100 dosimeters.

(a) (b)

Figure 4.10: The experimental setup used for determining TLD-100 sensitivty correction factors

TLD sensitivity

The sensitivity correction factors (SCF) were measured for both batches of TLDs. The factor requires TLD response to be based on identical reference conditions. An entire batch of TLDs is not able to be irradiated at the same point in a beam at the same time. To measure all TLDs under the same beam they had to be evenly offset from the central axis. The beam from an x-ray tube is not uniform across its profile. To ensure a uniform

exposure to all the TLDs in a batch they were rotated around the central axis of the beam at a fixed distance. A turntable (Figure 4.10a) was used to provide uniform exposure to the TLDs. An acrylic TLD phantom (Figure 4.10b) was placed on the turntable's rotating stage on top of an additional 5 cm of acrylic. The phantom is 2 cm thick and consists of 50 shallow-drilled holes spaced evenly in a 16 cm diameter circle. The TLDs were placed in the first 13 holes in the phantom. The phantom was aligned with the central axis of the x-ray beam. A mylar film was placed over top of the phantom. the source-to-surface distance was set to 100 cm. The phantom was rotated at 35 rpm. A total exposure of 1000 mAs was delivered for both 100 kV and 125 kV photon beams. A 50 x 50 cm^2 field size was set at the phantom surface. Only the beam hardening filtration was used for this measurement. The TLDs were readout and annealed following the procedure detailed above. Each batch was irradiated five times.

(a) (b)

Figure 4.11: The experimental setup used for determining TLD batch calibration factor, $N_{D,w}$

Determining TLD calibration factors

Each batch of TLDs was cross calibrated with a 0.65 cm^3 FC65-G (IBA Group, Louvain-La-Neuve, Belgium) farmer-type ionisation chamber. This was done to derive a batch conversion factor $N_{w,batch}$, for both beam qualities used. The ionisation chamber had

been calibrated in terms of air kerma at a primary standards dosimetry laboratory. The absorbed dose was measured using the AAPM TG-61 reference dosimetry protocol. To perform the cross calibration with TLDs an in-phantom measurement was performed. The measurement conditions for the experiment are given in Table 4.2.

An in-house acrylic water phantom was used to perform the cross calibration measurements (Figure 4.11a). The phantom includes a 3 mm thick acrylic waterproofing sleeve. A farmer-type ionisation chamber can be inserted into this sleeve. A TLD holder had also been designed to fit in the waterproof acrylic sleeve (figure 4.11b). The acrylic TLD holder can have up to 4 TLD-100 detectors placed into a recessed holding space. The position of the TLDs coincides with the sensitive volume of a Farmer-type chamber. An acrylic cover is placed over top of the TLDs to eliminate movement.
Four TLD chips were selected at random for both beam qualities. TLD exposures were performed directly after ion chamber measurements. A small amount of water was added to the tank to account for the 1.25 mm elevated active area of the TLD-100 detectors.

Table 4.2: Reference conditions used for in-phantom absorbed dose to water for the Truebeam XI system. Both the FC65-G Farmer-type ionisation chamber and TLD-100 detectors were exposed under the same conditions.

Reference condition	
Phantom material	Water
Chamber type	Farmer-type chamber (FC65-G)
Waterproofing	3 mm acrylic
Measurement depth	2 cm
SSD	100 cm
Field size at 100 cm	10 x 10 cm^2
Total exposure	1000 mAs
Filtration	Beam hardening and Bowtie

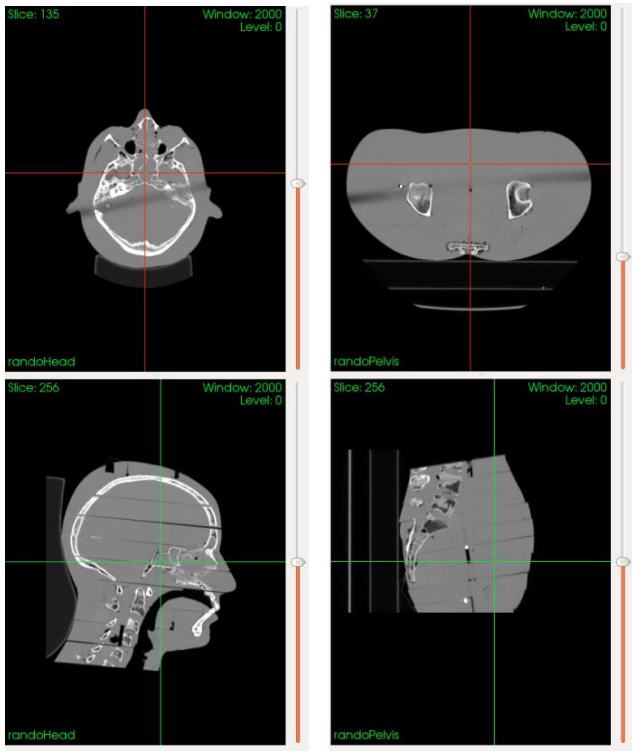

(a) Head phantom (b) Pelvis phantom

Figure 4.12: The RANDO phantom is an anthropomorphic phantom that can be used for the direct measurement of absorbed dose. The phantom is made up of 34 2.5 cm transverse sections. The CT images above show the individual sections of the phantom used in this study. These images were imported into GATE for dose comparison with physical measurements. The crosshairs are aligned to the isocentre of the scan.

4.2.2 Anthropomorphic phantom study

The Rando phantom (Radiation analog dosimetry system: Nuclear Associates, Hicksville, NY) was used to carry out a TLD dose study. The Rando phantom is an anthropomorphic male phantom. It is formed by a skeleton encased in a rubber material with radiological properties of near equivalence to soft tissue.[85] The phantom is shown in Figure **??**. The phantom is divided into 34 2.5 cm sections. These sections have cylindrical orifices which TLDs are placed within.

The phantom replicates a human anatomy from the top of the head to part way through the femoral bones. The volumes of the phantom used in this study were the head and pelvis. The head phantom includes the the portion of the phantom from the neck region and up (Figure 4.12a. The pelvis phantom covers the region of anatomy from the ilium to part way through the femurs (Figure 4.12b.

Firstly tomographic images of the phantom were acquired using a Toshiba CT scanner. The beam width used during CT acquisition was 1 mm for the rando head phantom and 2 mm for the pelvis phantom. The voxel size was 0.5 x 0.5 x 1 mm for the head phantom and 0.8 x 0.8 x 2 mm for the pelvis phantom. Both image sets were imported into the Varian Eclipse work station. TLD positions were contoured on the image set and the DICOM origin position was set to the isocentre of the scanning volume. The image sets were suitably free of artifacts.

The TLD-100 chip dosimeters were placed in the positions seen in Figure 4.13 for both head and pelvis phantoms. The TLDs measure 3 x 3 x 1 mm. Their size allows them to be placed in the orifices in the RANDO phantom. TLDs were irradiated in pairs in order to control for any unexpected variations in single TLD readings. Air gaps were filled with rubber plugs.

The phantoms with embedded TLDs were transferred to the treatment couch and the

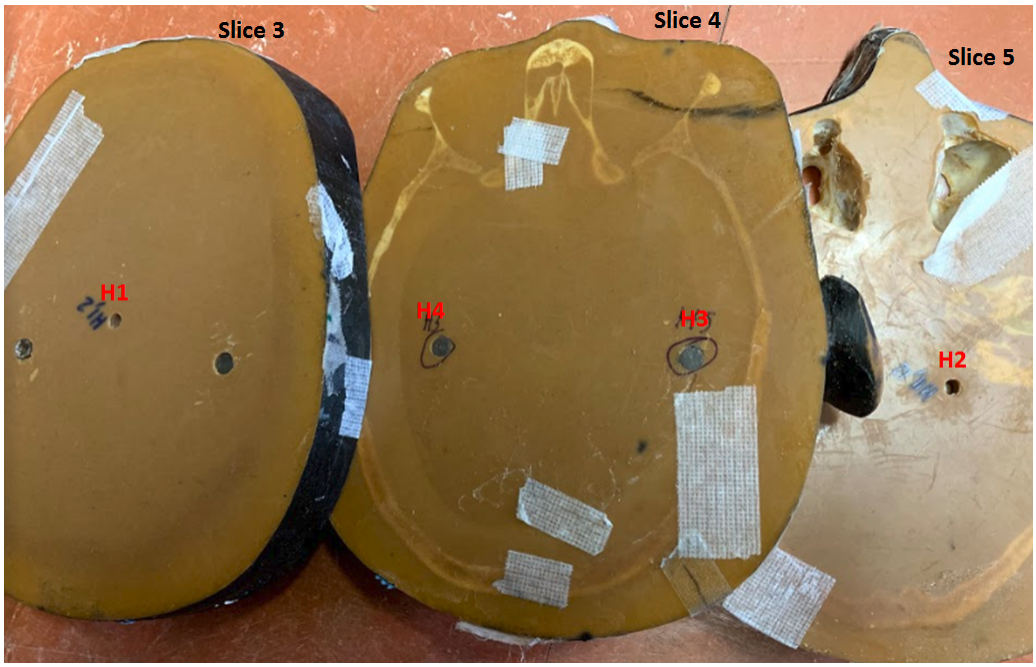

(a) Head phantom

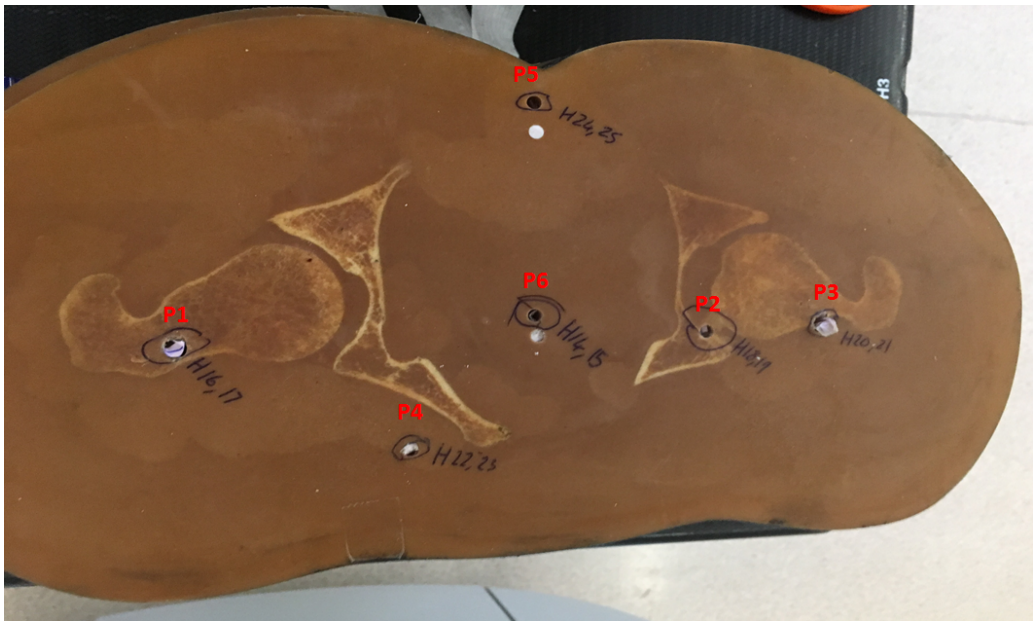

(b) Pelvis phantom

Figure 4.13: TLD dose measurement locations for the RANDO phantom (red text). Three sections of the head phantom were used for TLD measurements. Only one section of the pelvis phantom was used due to the higher number of orifices for TLD placement.

setup from CT imaging was replicated using marks that had been placed on the phantom in the saggital, transverse, and coronal planes. When the machine isocentre was matched with the phantom isocentre the imaging protocol was delivered. The scanning parameters used for scanning of the head and body phantom are shown in table 4.1.

4.2.3 Simulation in GATE

GATE has the ability to import medical image data or STL files to construct voxelised phantoms. Metaimage files are a medical image file format that are compatible with GATE. Metaimage data retains DICOM coordinates and properties important to anatomical representation. It has the advantage over DICOM and STL data of being a stable image.

The DICOM image studies of the RANDO phantom were converted into metaimage files and imported into GATE. Dose actors were attached to the volumes. The resolutions used for the voxelised grids were set to match voxel size of each image study (given above). The output file from the dose grid set to metaimage file to retain the isocentre position used in the simulation. Image grayscales were converted into material definitions using values given from a study by Schneider et al.[86]

After the GATE simulation was complete the metaimage dose grids were simulated in GATE for the two phantoms. The MetaImage dose grid was imported into ImageJ. TLD positions that had been contoured in Eclipse were converted to .roi files that are read into ImageJ's "ROI manager". The dose for each TLD position.

4.2.4 Results

AAPM TG-61 Reference dosimetry for XI CBCT

The HVLs measured for both beam configurations are given in table 4.3. The 125 kVp, half bowtie filter configuration and 100 kVp, full bowtie filter configuration had a HVL of 8.3 mm Al. The 100 kVp, full bowtie filter configuration had an HVL of 7.1 mm Al.

Direct measurements of HVL resulted in an increase of 0.3 mm Al in these values. The increase was assumed to be attributed to back-scatter from the detector panel and the values were discarded.
Reference dosimetry was performed for both the filtered 100 kVp and 125 kVp spectra. Reference conditions are specified in table 4.2. Using the AAPM TG-61 absorbed dose to water protocol at 2 cm depth the dose rate was found to be 90 μGy/mAs and 50 μGy/mAs for the 125 kVp and 100 kVp beams, respectively. The ion chamber measurements were reproducible within 0.2%. A worksheet for for TG-61 reference dosimetry is included in Appendix A.1.

Cross-calibration of point dose to TLDs

TLDs were calibrated under the reference conditions used in table 4.2. From this measurement calibration factors were calculated to convert TLD dose response into absolute dose. Calibration factors of 0.16 mGy/nC and 0.19 mGy/nC were given for the 125 kVp and 100 kVp beams, respectively. The derivation of TLD calibration factors is shown in appendix Figure C.2.

The TLD dose linearity was assessed over a range of exposures from 10 mAs to 1000 mAs. The TLD measured dose against exposure is given in figure 4.14.

Table 4.3: Half value layer (HVL) was measured using the Pirahna CT dose profiler (CTDP). The corresponding air-kerma calibration factor is also given

Tube potential (kVp)	Bowtie filter	HVL (mm Al)	Calibration factor, N_k (mGy/nC)
125	Half	8.34	44.95
100	Full	7.12	45.02

Monte Carlo calibration factors

Simulated and experimental results were gathered in the RANDO anthropomorphic phan-

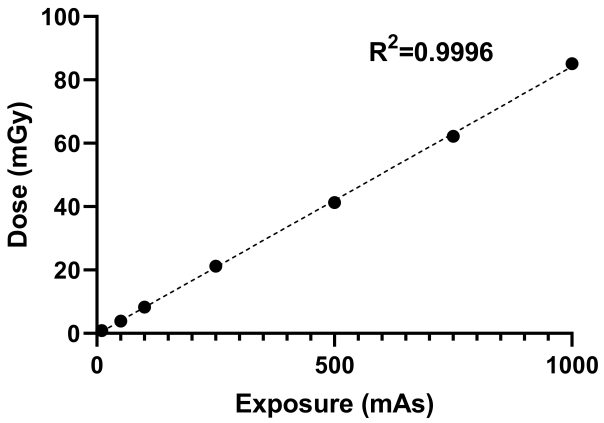

Figure 4.14: TLD dose linearity over the exposure range 10 mAs - 1000 mAs

tom. The statistical uncertainty for MC simulated doses in RANDO was less than 2.5% at all measured points (for 2×10^7 total primaries). Calibration factors were calculated to convert simulated results into valid experimental results. For the head scan protocol (100 kVp, 7.1 mm Al) the calibration factor was $2.46 \times 10^{11} \pm 1.02 \times 10^{10}$ photons/mAs. For the body scan protocol (125 kVp, 8.3 mm Al) the average calibration factor was $4.29 \times 10^{11} \pm 1.26 \times 10^{10}$ photons/mAs.

Table 4.4: Comparison between measured and simulated doses for both pelvis and head phantoms. Figure 4.13 can be used as a reference for the TLD positions. The doses are reported in dose to water

Location	TLD (mGy)	GATE (mGy)	Difference
	Pelvis scan		
Right femoral head (P1)	15.2±1.0	24.9±0.3	48.5%
Left Ischial Spine (P2)	17.5±1.2	16.9 ±0.9	-3.5%
Left femoral head (P3)	19.8±1.0	21.4 ±0.5	8.2%
Right femoral artery (P4)	24.7±1.3	25.4 ±0.3	-3.2%
Sacrum (P5)	25.4±1.3	25.3 ±0.3	0.0%
Centre (P6)	25.3±1.3	20.9 ±0.4	-18.7%
	Head scan		
Superior (H1)	3.1 ± 0.2	$2.8 \pm < 0.1$	-9.2%
Inferior (H2)	3.1 ± 0.2	$3.5 \pm < 0.1$	10.1%
Right (H3)	2.8 ± 0.2	$2.9 \pm < 0.1$	3.2%
Left (H4)	3.2 ± 0.2	$3.1 \pm < 0.1$	-3.1%

5 CBCT population dose analysis

Cone-beam CT technology is widely deployed throughout radiation therapy clinics worldwide. There are numerous studies evaluating indirect measures of dose for these scanners. Patient dosimetry, however, makes up a small portion of CBCT dose studies and scanners, such as the XI, have limited information on the absorbed dose received by patients from their use. In this chapter the ICRP computational phantom is imported into the GATE simulation environment to preform dose calculations. The data gathered is used to evaluate the effective dose and to construct dose-volume histograms from CBCT imaging procedures.

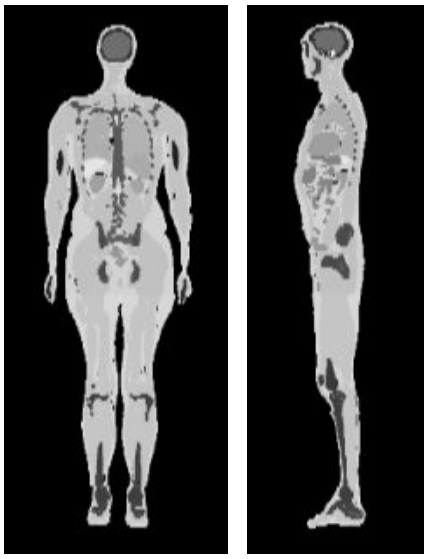

(a) Frontal view (b) Saggital view

Figure 5.1: The ICRP computational phantom is an aggregated anthropomorphic phantom from the medical imaging data of real people. The organs are consistent with anatomical data given by ICRP report 89.

5.1 Method

The ICRP phantom was imported into GATE. The ICRP phantom is a 27.14 cm x 54.28 cm x 177.6 cm (127 x 254 x 222 pixels) volume. The 'ImageNestParameterised' navigation algorithm option was used to translate the phantom in the phantom volume.
CBCT imaging dose were investigated for six common radiation treatment sites:

- Head imaging protocol. 2 sites: Brain and larynx.
- Thorax imaging protocol. 3 sites: Mid-lung, left lung, and right lung.
- Pelvis imaging protocol. 1 site: Prostate.

For each site the ICRP phantom was translated so the anatomy aligned with the isocentre of the model. Simulations were performed using both clockwise and counterclockwise acquisitions. For head and neck scanning, which involves a 200 degree scanning arc, a counter clockwise rotation from 90° and 250° was used.

The seTLE dose actor was applied to the phantom volume. The resolution of the dose actor was set to 0.21 x 0.21 x 0.8 cm to match the resolution of the image set. The primary multiplicity factor was set to 200 and the secondary multiplicity was set to 400. These values were chosen to provide the optimal primary dose vs secondary dose distribution ratios.[76] The total number of primaries generated was 1×10^7

The calibration factors determined in the previous chapter were used to convert the simulated doses to absorbed dose. As pelvis and thorax imaging protocols use the same beam energy, bowtie filter, and collimation, the same calibration factor was used. The simulated doses were divided by the total number of primaries simulated and then multiplied by the total exposure (mAs) and dose calibration factor.

The metaimage dose grids were analysed in imageJ. The ICRP phantom organs were contoured using the inbuilt region of interest (ROI) manager. DVHs were constructed

using a combination of the ROI manager and inbuilt thresholding tools in imageJ.

5.2 Results

5.2.1 Effective dose

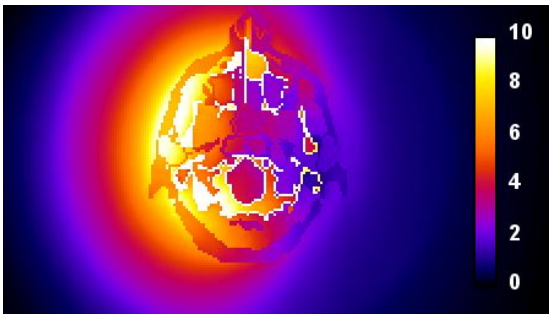

(a) Head and neck

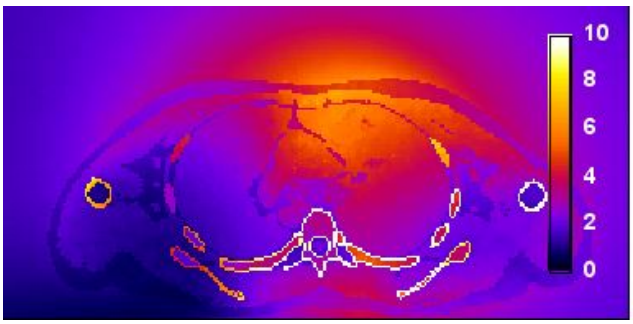

(b) Thorax

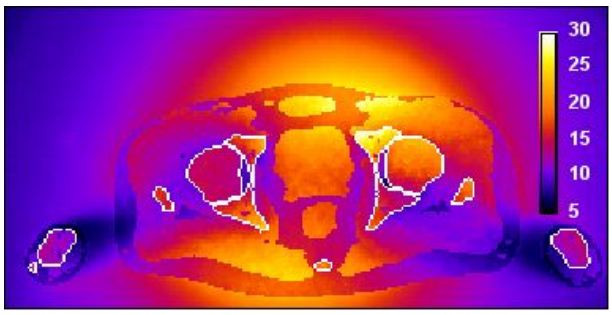

(c) Pelvis

Figure 5.2: Simulated dose distribution grids for the three XI imaging protocols. Doses are given in mGy.

Simulating dose grids for CBCT imaging protocols took between 67 and 84 hours using the Intel 8 core processor. Organ doses and effective doses were simulated for each XI scan procedure. The results are seen in table 5.1. Organ doses are given as average values over the entire organ volume. Repeat simulations showed that total effective doses were reproducible within 1%.

The highest effective dose was calculated for pelvis imaging. The effective dose was 3.91±0.11 mSv when the prostate was at the isocentre of the scan. The highest average organ doses were received by the gonads (24.6 mGy) and the bladder (19.4 mGy). Whole body organs such as bone marrow, bone, and skin received average doses of 3.0 mGy, 7.8 mGy, and 1.87 mGy. The maximum doses of these structures 40.2 mGy, 94.6 mGy and 30.8 mGy (table 5.2).

Thorax imaging had an effective dose of 1.72±0.07 mSv (lung centre at isocentre). The highest average organ dose was received by bone (6.2 mGy). Lung, breast, and thyroid received average doses of 3.2 mGy, 3.2 mGy, and 3.4 mGy. The average skin and bone marrow doses were 0.5 mGy and 1.6 mGy. Maximum doses for bone marrow, bone surface, and skin were 12.4 mGy, 30.1 mGy, and 8.2 mGy.

Head imaging had an effective dose of 0.289±0.020 mSv (brain at isocentre). The highest average organ dose was recieved by the salivary glands (3.9 mGy) and brain (2.3 mGy). Whole body organs such as bone marrow, bone, and skin received average doses of 0.6 mGy, 1.1 mGy, and 0.5 mGy. Maximum doses for these organs were 14.1 mGy, 18.3 mGy, and 7.8 mGy, respectively.

The effective dose for all six scans centres analysed are summarised in table 5.3.

Table 5.1: Organ and effective doses simulated for XI scan protocols. Head scans were performed between gantry angles 270° and 110°

	Head	Thorax	Pelvis
Tube voltage (kVp)	100	125	125
Tube current (mA)	15	15	60
Pulse duration (ms)	20	20	20
Exposure (mAs)	147	264	1074
Scan arc (deg)	200	360	360
Organ dose (mGy)			
Bone marrow	0.616	1.57	2.96
Colon	0.00978	0.260	2.96
Lung	0.0627	3.24	0.0690
Stomach	0.0175	1.67	0.156
Breast	0.0402	3.19	0.0858
Gonads	0.00507	0.0135	24.6
Bladder	0.00405	0.0174	19.4
Oesophagus	0.436	2.75	0.0484
Liver	0.0168	1.85	0.182
Thyroid	0.658	3.42	0.0506
Bone surface	1.10	6.21	7.84
Brain	2.33	0.0422	0.0302
Salivary glands	3.89	0.297	0.0466
Skin	0.474	0.466	1.87
Remaining tissues*	0.639	1.17	2.05
Total effective dose (mSv)	0.289 ± 0.020	1.72 ± 0.07	3.91 ± 0.11

*adrenals, extrathoracic region, gall bladder, heart, kidneys, lymphatic nodes, muscle, oral mucosa, pancreas, prostate, small intenstine, spleen, thymus

Table 5.2: Simulated average and maximum organ doses for XI scan protocols. Critical structures for each site are included as well as the dose to whole body organs (i.e. skin, bone, bone marrow)

Scan	Location	Average dose (mGy)	Maximum dose (mGy)
Head	Isocentre	3.5	-
	Brain	2.3	14.5
	Left eye	5.6	6.3
	Right eye	5.4	6.1
	Left lens	5.9	6.0
	Right lens	6.1	6.2
	Skin	0.5	7.8
	Bone	1.1	18.3
	Bone marrow	0.6	14.1
Thorax	Isocentre	5.1	-
	Left lung	2.5	5.4
	Right lung	4.0	6.4
	Spinal cord	1.4	2.9
	Skin	1.1	7.6
	Bone	6.3	30.6
	Bone marrow	1.6	12.3
Pelvis	Isocentre	16.9	-
	Bladder	19.4	26.5
	Rectum	17.8	20.0
	Gonads	24.6	30.3
	Skin	2.3	30.8
	Bone	7.9	94.6
	Bone marrow	2.9	40.2

Table 5.3: A summary of the effective doses for the scan protocols and imaging centres examined in this study.

Scan protocol	Scan centre	Total effective dose (mSv)
Head	Brain	0.29 ± 0.02
	Larynx	0.89 ± 0.04
Thorax	Mid-lung	1.72 ± 0.08
	Left lung	2.03 ± 0.09
	Right lung	1.53 ± 0.07
Pelvis	Prostate	3.91 ± 0.11

5.2.2 Treatment planning doses

Dose volume histograms were calculated for CBCT imaging. The DVHs are reported for organs at risk and are based on scan protocol and isocentre location. The DVHs for three scan protocols and six scanning isocentres can be seen in figures 5.3, 5.4, and 5.5. $D_{50\%}$ and $D_{10\%}$ metrics are given for the major planning organs at risk and target structures for each anatomical site. $D_{50\%}$ and $D_{10\%}$ are the minimum dose delivered to 50% and 10% of the organ volume, respectively.

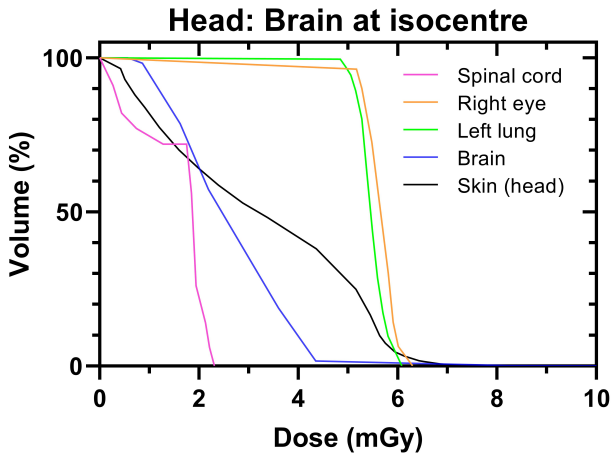

(a) Brain scan DVH

Organ	$D_{50\%}$ (mGy)	$D_{10\%}$ (mGy)
Spinal cord	1.87	2.17
Right eye	5.66	5.96
Left eye	5.46	5.81
Brain	2.46	3.98
Skin	3.19	5.65
Pituitary	3.35	3.56

(b) Brain scan dose statistics

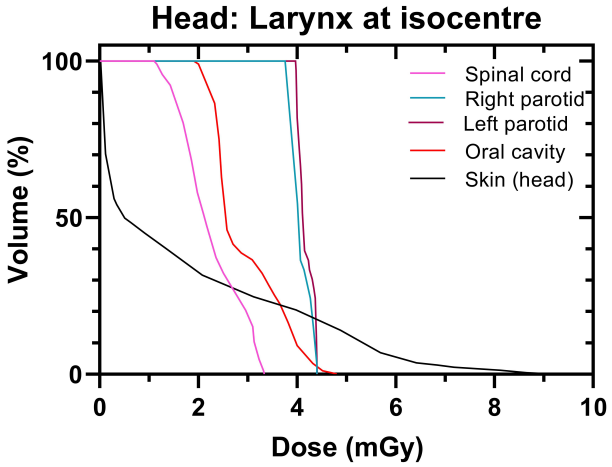

(c) Larynx scan DVH

Organ	$D_{50\%}$ (mGy)	$D_{10\%}$ (mGy)
Larynx	2.38	7.18
Spinal cord	2.12	3.13
Oral cavity	2.56	3.98
Left parotid	4.11	4.39
Brain	0.33	0.78
Skin	0.51	5.33
Right parotid	4.03	4.36
Oral cavity	2.55	3.94

(d) Larynx scan dose statistics

Figure 5.3: Dose-volume histograms (DVHs) (a,c) and tabulated dose metrics (b,d) for radiosensitive organs from XI CBCT imaging. (a,b) Head CBCT imaging is performed with the brain at the isocentre. (c,d) Head CBCT imaging is performed with the larynx at the isocentre

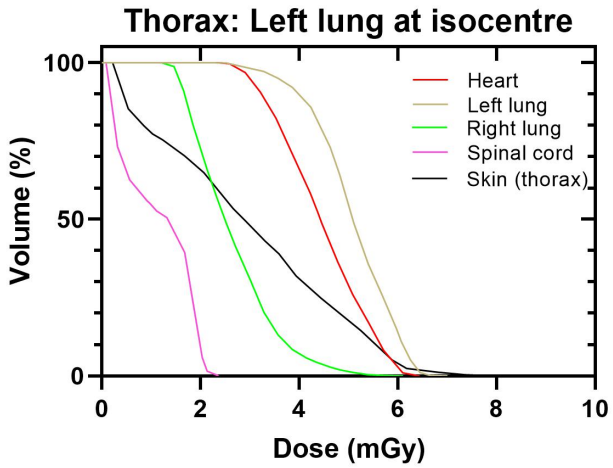

(a) Left lung scan DVH

Organ	$D_{50\%}$ (mGy)	$D_{10\%}$ (mGy)
Heart	4.43	5.66
Right lung	2.49	3.77
Left lung	5.08	6.10
Spinal cord	1.34	1.99
Skin	2.88	6.10

(b) Left lung scan dose statistics

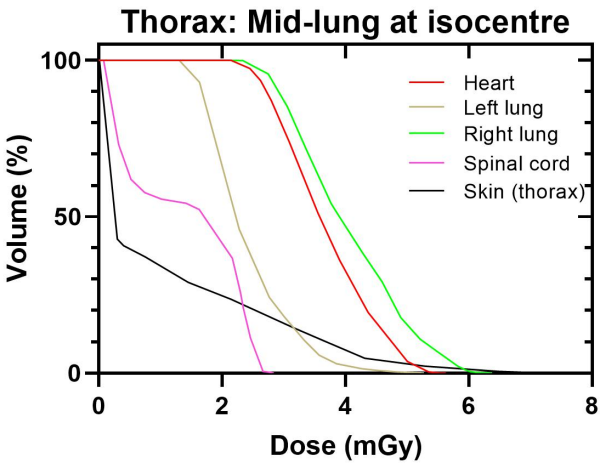

(c) Mid-lung scan DVH

Organ	$D_{50\%}$ (mGy)	$D_{10\%}$ (mGy)
Heart	3.58	4.85
Right lung	3.89	5.27
Left lung	2.22	3.59
Spinal cord	1.70	2.48
Skin	0.285	3.62

(d) Mid-lung scan dose statistics

Figure 5.4: Dose-volume histograms (DVHs) (a,c) and tabulated dose metrics (b,d) for radiosensitive organs from XI CBCT imaging. (a,b) Thorax CBCT imaging is performed with the left lung at the isocentre. (c,d) Thorax CBCT imaging is performed with the mid-lung at the isocentre

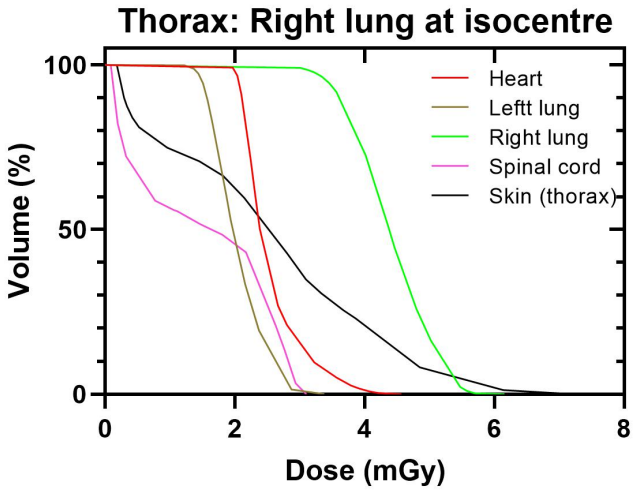

(a) Right lung scan DVH

Organ	$D_{50\%}$ (mGy)	$D_{10\%}$ (mGy)
Heart	2.39	3.21
Right lung	4.51	5.22
Left lung	1.97	2.63
Spinal cord	1.64	2.82
Skin	2.52	4.73

(b) Right lung scan dose statistics

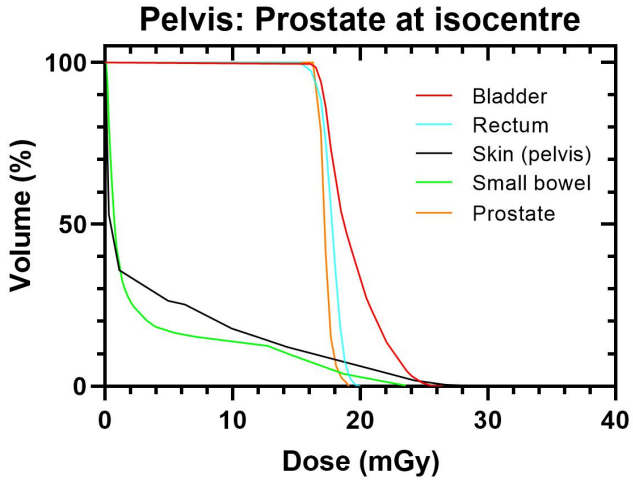

(c) Prostate DVH

Organ	$D_{50\%}$ (mGy)	$D_{10\%}$ (mGy)
Prostate	17.2	17.9
Bladder	18.7	22.4
Bowel	0.714	14.4
Rectum	17.8	18.7
Skin	0.429	16.3

(d) Prostate scan dose statistics

Figure 5.5: Dose-volume histograms (DVHs) (a,c) and tabulated dose metrics (b,d) for radiosensitive organs from XI CBCT imaging. (a,b) Thorax CBCT imaging is performed with the right lung at the isocentre. (c,d) Pelvis CBCT imaging is performed with the prostate at the isocentre

6 Discussion

There have been several studies carried out to quantify dosimetry from CBCT imaging.[17,37,40] These studies report on a variety of direct and indirect measures to quantify dose from different CBCT scanners.[30,33,57,74,87,88]
This thesis work uses Monte Carlo (MC) methods to quantify patient dosimetry from CBCT imaging using the Varian XI scanner. As of this work, there is a scarce amount of directly measured dosimetry data available for this scanner.[31,58] Additionally, no studies have evaluated organ dose-volume histograms for the scan protocols used by the XI system.

6.1 Validation and calibration of the GATE CBCT model

Validation of the MC model started with verifying the x-ray spectra simulated. X-ray spectra were simulated in GATE by modelling the GS-1542 x-ray tube according to manufacturer documents. 2.7 mm aluminium filtration was applied to the tube to simulate the spectra. The initial validation was provided by matching simulated and experimental depth dose results, with no additional filtration, in a 10 cm x 10 cm field (figure 4.1). The agreement in these PDDs was 3%. Once PDDs were verified with no additional filtration, simulations were performed for the Varian XI scan protocols.

The method used for simulating and validating x-ray spectra did not provide consistent accuracy for both beam models. The full experimental validation results show that the spectrum simulated for the 125 kVp beam model was more accurate than the 100 kVp beam model. Both relative dosimetry and absolute dosimetry measurements yielded better agreement with the 125 kVp spectra.

6.1.1 Relative dosimetry

Relative dosimetry comparisons were made between simulated and experimental results. For the scan protocols examined comparison of PDDs showed good agreement and matched within 2% for the differing field sizes and filtration conditions examined.

Simulated and experimental profiles matched within 10% of each other. It is seen in figure 4.4 that the best match is seen in the x-axis with no bowtie filter in place. These profiles match within 4% (outside of the penumbra region). When the bowtie filter is added results match within 4% for the body scan protocol and 10% for the head scan protocol.

In figure 4.4 it is shown that the experimentally measured profiles in the Y-axis display an asymmetry across the direction of the beam measurement. The measured profile shows higher deposition towards the cathode side of the profile. This trend is due to self-attenuation in the anode or the "heel effect". The heel effect occurs due to the increased travel length through the anode material for photons emitted towards the anode side of the tube (figure 4.6). Increasing travel distance through the tungsten anode leads to greater probability of photon attenuation. This results in an x-ray beam with less intensity towards anode side of the x-ray tube. The simulated results do not replicate the heel effect. The voxelised source input in GATE does not allow the modelling of this intensity distribution across the source.

Marchant and Joshi proposed a method for modelling the heel effect using a voxelised source input.[40] Their method involved generating a tungsten medium in their simulation and positioning the source below the surface of the anode. The source is placed at the mean depth of interaction (which is a few microns deep). From there the source can be rotated to replicate the differential travel path length of x-rays generated in the anode. Problematically, this will modify the energy distribution the of x-ray spectrum due to attenuation in the anode. It will also reduce simulation efficiencies from extra CPU time spent tracking photons inside the anode volume.

It was decided that as the experimental and simulated y-axis profiles matched within 10%, comparable to the x-axis profiles, no further action would be taken to model the heel effect. To simulate the heel effect for future work it is recommended that a phase space type file should be used instead of the voxelised source input.

6.1.2 Absolute dose calibration

6.1.2.1 TLD Rando study

TLDs were calibrated under 100 kVp and 125 kVp beams at a point 2 cm deep in water. The TLDs were placed in the anthropomorphic head and pelvis RANDO phantom. The measured doses varied between 15.5 mGy and 25.3 mGy

A study conducted by Hauri et al. examined pelvic imaging doses from the XI system in the RANDO phantom.[58] Their findings show good agreement with the ones found in this study. The mean dose from found from 37 in-field measurements was 20.5 mGy±5% in Hauri et al. compared to 21.3 mGy±3% in this study. This study measured these values based on 6 points.

The response of the TLDs was corrected only for batch sensitivity and energy dependent calibration. The response of the TLDs were not depth corrected. Studies have shown there is expected to be a variation in TLD response with depth.[89,90] A study by Mail et al. introduce a correction factor that compensates the response of luminescent dosimeters at depth.[89] The depth correction factor was given as a ratio of the dose measured by ionisation chamber to that of the uncorrected dosimeter as a function of depth. The ratio varied TLD response by a maximum of 2%. The energy response of TLDs at depth was not considered on the TLD study conducted in this work. This could be incorporated into future work. Another study found that spectral changes at depths between 1 cm and 10 cm under a 6 MV beam resulted in an 8.5 % variation in energy correction factors.

6.1.2.2 Monte Carlo calibration factor

The CT image studies for both phantoms were imported into GATE. Dose distributions were simulated for both phantoms. On the simulated dose grid measurements were performed at the TLD locations shown in figure 4.13. A calibration factor was applied to the simulated doses to analyse the suitability of the factor. The calibrated simulated results and TLD measurements showed expected agreement (Table 4.4). The average difference with experimental measurements was 13.7% for pelvis CBCT and 6.4% for head CBCT. The maximum difference for both protocols was 48.5% and 10.1%, respectively.

From table 4.4 it can be seen the simulated result at point P1 in the pelvis phantom showed a large difference with its corresponding experimental value. The simulated dose was 48.5% higher than its corresponding experimental measurement. This difference is due to the HU value from the CT image. TLD measuremenets were performed at Point P1 was measured in the femoral spongiosa. The surrounding bony anatomy resulted in an increased HU value at this point which changed the material conversion applied when using the Schneider conversion table. The remaining TLD location There are limitations in using grayscale to material definition conversions. grayscale value for a given material can vary depending on the CT system used and how a scan is parameterised. Segmentation of the RANDO phantom may have ensured more consistency in the grayscale conversion for the specified materials.[85]

The biggest discrepancy for the pelvis phantom comparison was in the measurement at the centre of the phantom. The calibrated MC dose underestimated the dose to this point by -25.1%. It is thought that this is due to a weighting bias in determining the calibration factor in this study. From observing figure 4.13b.

For the head phantom measurements the largest discrepancy is seen for TLD measurements in the inferior and superior portions of the phantom. This is due to the absence of the heel effect in the simulated dose distribution (see y-axis profiles in figure 4.4). The superior and inferior measurements are separated in the y-axis of the imaging field. In

the superior position the TLD dose is underestimated 9.2% by the simulated result. In the inferior portion of the beam it is overestimated 10.1% by the simulated result.

Using relative benchmarks for absolute calibration is not as robust as an absolute comparison. The relative benchmark measurements used here are made worse by the use of TLD detectors. Repeat TLD-100 measurements typically vary between 2% and 10%.[25] By performing 3 to 4 measurements the type A uncertainty did not exceed 5%. The total combined uncertainty did not exceed 10% for any of the measurements. The influence quantities for the combined uncertainty evaluation are seen in Appendix **??**.
There was a limited number of TLD-100 dosimeters available for use in this study as many were also required for clinical use. The number of sites measured was acceptable for evaluating the dose due to imaging but insufficient for calibrating a MC beam model. By increasing the number of measurement sites a MC calibration factor could be more accurately determined. To improve the calculation of the MC calibration factor it is recommended that more measurement locations be used both in-field and out-of-field.

6.2 Population dose calculations

There are three CBCT image acquisition modes used by the XI scanner. This study examines the dosimetry for all three imaging modes. The ICRP phantom was used to provide a computational phantom that is anatomically representative of a cohort of radiation therapy patients. The organs in the phantom are consistent with the anatomical parameters given in ICRP report 89 allowing the analysis of organ and effective dose.[91]

6.2.1 Organ dose and effective dose

The effective dose is a weighted risk estimate for low dose procedures. The absorbed dose received by a number of organs around the body are weighted. The limitation of scoring dose in out-of-field organs should be considered. Due to low photon scoring in these organs the uncertainty in their dose measurement is higher than doses scored in the scanning field. The uncertainties in each organ are factored in to the combined uncer-

tainty for the effective dose.

Organ and effective doses were calculated using the ICRP phantom dose grids. The results in table 5.1 are comparable to those found in a study by Pyone et al. (table 2.1). In their study they used the ImPACT CT dosimetry software to calculate effective doses for the three XI CBCT protocols. For the head, thorax and scan protocols they calculated total effective doses of 0.1 mSv, 2.4 mSv, and 4.9 mSv. The ImPACT software calculates organ and effective doses that are higher than those dound in this study for the head CBCT imaging protocol. the difference between the ImPACT calculator and MC lower than those found by MC methods here. The difference in effective dose for head, thorax, and pelvis CBCT imaging is -65.4%, -14.0% and -10.5%, respectively. This appears to agree with the observation made in chapter 4 regarding excessive beam hardening of the spectra from the beam model. It must also be noted that the ImPACT software calculates non-isocentre specific organ doses from CTDI measurments and therefore a true comparison is difficult to establish.

The effective dose calculated by Hauri et al. shows good agreement with the doses calculated here. Only the dose received by the gonads was estimated due to the limitations of available measurement points in their RANDO phantom. Although their study arrived at the same calculated effective dose there are a number of discrepancies between the absorbed doses measured in their work and this study.
The measured skin dose in Hauri et al. greatly exceeds the one calculated in this study. The skin dose measured for pelvis scanning in their study is 458% higher than the calculated dose in this study. The difference in skin dose is due to two factors. Firstly, only 5 measurement points were taken for the whole body skin dose in Hauri et al. This will skew the dose response towards teh dose response in the in-field measurements. TLDs have been used in many radiation therapy studies and are known to

Effective dose for evaluating radiation-induced cancer risk for low doses is a useful descriptor. Especially in the case that there is no available epidemiology studies. However,

it is important to not put too much emphasis on effective dose values as they are intended as a rough estimate of dose detriment for patients. The radiation and tissue weighting factors are based on current, limited understanding of radiation risks. They are simple values with large uncertainties associated. For example, using the radiation weighting factor for x-rays a given organ dose from a 100 kV and a 6 MV source would be weighted equally for biological damage. Tissue weighting factors are age- and sex-averaged values that do not reflect the likelihood of cancer development in different subjects, regardless of age or gender. A study on the uncertainties in effective dose calculation was preformed by Martin.[92] In his studies experimental, empirical, and Monte Carlo methods for determining effective dose. The study finds that for a given phantom the uncertainties in calculating effective dose can reach 40%.

It is important to note that organ and tissue radiobiological sensitivities are not consistent with age and gender. It is desirable that weighting factors set by the ICRP can be used dose-risk correlation for patients of differing age and gender.

These scans are not isocentre specific. In a study by Martin the uncertainties associated with effective dose calculation are analysed. The study finds that even for population-based phantoms uncertainties in calculating effective dose may reach 40%.[92]

Effective dose calculations are heavily weighted towards the thorax region of human anatomy. There are many structures in this region that the effective dose is calculated for. Therefore accurate dose scoring in the thoraz region will provide a better estimate of effective dose. Due to the absence of the heel effect in the beam model the effective doses calculated varied for out-of-field organs. For the head scanning protocol, the simulated results overestimated the absorbded dose to organs in the inferior portion of the phantom, lead to an overall increase in effective dose. For pelvis CBCT imaging the absorbed doses to superior organs were underestimated, resulting in a smaller value for effective dose. Thorax CBCT imaging is the least biased by not modelling the heel effect in the beam model.

Offset in scan centre had a small impact on effective dose. The uncertainty is lower for pelvis scanning than thorax or head scans. This is due to the scanned region being more central in the voxelised phantom. A head scan occurs at the superior end of the phantom. So particle scoring at the inferior end of the phantom is significantly less. The effective dose takes account of dose from organs throughout the body. Using this information it can be inferred that the uncertainty for pelvis scan effective dose is less than other scanning methods when using MC methods. Although effective dose calculations tend to be weighted towards the upper half of the body. Simulated pelvis imaging doses are more accurate for 'whole body organs' such as skin, muscle, bone, lymph vessels, and marrow.

For the purposes of radiotherapy planning dose is usually given as dose to water. This is a quantity that can be more easily tied to radiobiological effect. All doses in this study were given in dose to medium. GATE allows a user to convert dose in medium into dose to water for conventional dose actors. For seTLE dose scoring such as in the seTLE dose actor dose to water conversion is not available.

Previous effective dose estimates have been performed using the TrueBeam XI system.[93] This study used a physical phantom and performed measurements at one discrete point within each organ. This estimate is limited in that it does not consider the dose over the entire organ. Exclusion of the periphery organ dose will lead to considerable uncertainty. It should be noted that for each scan, out-of-field organ dose have significantly more noise than in-field organs. This is due to the lower number of photons scored out-of-field. Despite this the effective dose values from repeat simulations were found to be reproducible to within .

From observing Figure 4.7 it is clear that the GATE model underestimates the off-axis ratios with the full bowtie filter in place. The discrepancy between central axis and peripheral field doses is therefore expected to be overestimated in simulated doses.

MC doses for pelvis, thorax and head scans were converted using calibration factors

determined at nominal exposure values. Due to fluctuations in the tube current the total mAs delivered during a scan may be reduced by as much as 20 mAs. The sensitivity of the Monte Carlo conversion factor (equation **??**)was tested for a range of delivered exposures from both the pelvis and head scan protocols. The factor varied by as much as 2.5%. Due to TLD dose calculations being averaged over repeat measurements the fluctuations. It is worth noting that the range of variations in exposure had negligible effect on the dose analysis.

6.2.2 Treatment planning dose summary

A dose-volume histogram (DVH) graphically summarises the the dose distribution within a volume of interest for plan evaluation. DVHs for organs at risk (OARs) can be used to estimate normal tissue complication probability. In this study DVHs for OARs from CBCT imaging were quantified. This data can be used in addition to DVHs for therapeutic radiation deliveries to more accurately assess clincal endpoints. Doses are presented in dose to medium due to the inability to simulate dose-to-water when using the seTLE variacne reduction dose actor. If performed on a more computationally powerful computing cluster it would be desirable to use conventional dose actors and also enable dose scoring to water.

From observing figures 5.4a, 5.5a, and 5.4c the variation in organ dose from thorax CBCT can be observed. There is negligible dose sparing of the right lung when the scan centre is moved from the midlung to the left lung. The only benefit conveyed by shifting isocentre to the left lung is reducing dose to the spinal cord. As expected the heart dose is greatly reduced when the isocentre is moved to the right lung.

Obviously DVHs will vary depending on the size of the volume and to what extent the volume is contoured. The values given in this work are intended to provide estimates for absorbed dose to different organs due to CBCT imaging. The MC model used here could also be applied to DVH analysis in actual patient cohorts. The analysis would most likely be retrospective due to the long computation times from these simulations.

Head and neck regions contain many critical organs. It has been shown in a study by Ding et al. that acquiring a 200 degree head scan through the posterior of a patient will decrease the absorbed dose by the eyes while increasing the spinal cord dose.[94] The maximum dose received by the eyes when treating through the anterior portion of the face for the Varian OBI (v 1.4) was found to be 0.7 cGy per scan. When performed with the XI head scan protocol the maximum dose to the left and right eyes was 0.6 cGy.

It is is shown that pelvis CBCT imaging consistently delivers the highest doses to radiosensitive organs. The protocol delivers a higher total exposure than the other protocols and completes a full rotation around the patient volume. When the prostate is at the isocentre of the scan it is shown in figure 5.5c that the dose received by the OARs in the field receive a relatively uniform dose across their volumes. The $D_{50\%}$ and $D_{10\%}$.

Generally pelvis CBCT are performed on a daily basis for tumour verification. From the results presented the average doses for the bladder, rectum, and gonads are 19.4 mGy, 17.8 mGy, and 24.6 mGy, respectively. For a conventional prostate treatment, depending on the risk of the tumour, daily imaging would amount from at least 37 scans to 45 scans. This would result in a maximum absorbed dose of 0.71 Gy - 0.87 Gy for the bladder, 0.66 Gy - 0.80 Gy to the rectum, and 0.91 Gy - 1.11 Gy for the gonads. For some fractions multiple CBCTs may be acquired in a single session, further escalating the possible dose. Obviously DVHs will vary depending on the size of the volume and to what extent the volume is contoured. The values given in this work are intended to provide estimates for absorbed dose to different organs due to CBCT imaging. The MC model used here could also be applied to DVH analysis in actual patient cohorts. The analysis would most likely be retrospective due to the long computation times from these simulations.

The effect of the treatment planning couch on CBCT dose was examined using the previously acquired RANDO pelvis simulated dose grid. By monitoring the air-to-entrance

dose on the posterior and anterior side of teh phantom it was seen that the impact of the carbon fibre CT couch was negligible.

7 Conclusion and Future Work

There were two objectives in this study: 1) To use the GATE Monte Carlo (MC) toolkit to construct and validate a Monte Carlo model for CBCT dose calculation and 2) To perform Monte Carlo dose calculations for site-specific CBCT imaging protocols.

A MC model was constructed of the Varian XI scanner. The x-ray spectra were simulated for the 100 kVp and 125 kVp beams used for CBCT acquisition. The simulated spectra were used to parameterise a voxelised source input for the XI beam model. The remaining components of the beam model were included according to manufacturer documentation.

The results simulated from the GATE model were compared against experimental measurements. PDDs and profiles were compared to assess the dose accuracy of the GATE model. PDDs matched within 2% while profiles match within 10%. The match for the head scan protocol seemed to be due to a mismatch between the simulated and experimental spectra. Therefore, extra validation should be required for verifying energy spectra. The voxelised source input was unable to model the spatial intensity of photons across the anode volume or the 'heel effect'.

TLD measurements were performed in the anthropomorphic RANDO phantom to provide a calibration factor to convert MC dose calculations into absorbed dose. The TLD dose measurements used in deriving the calibration showed an average difference with simulated results of 13.7% for pelvis CBCT and 6.4% for head CBCT.

The second part of the study involved calculating population doses within an ICRP phantom. The phantom was imported into the beam model and simulations were performed using the three XI scan protocols at different isocentres of the phantom. The dose grids scored over the phantom volume were subsequently analysed for effective dose calculations

are construction of dose-volume histograms (DVH).

The effective dose given for the head, thorax, and pelvis CBCT imaging was 0.289 mSv ± 0.020 mSv, 1.72 mSv ± 0.07 mSv, and 3.91 mSv ± 0.11 mSv, respectively. Based on organ and effective dose data it was shown that the absorbed dose was overestimated using the head CBCT imaging beam model. While thorax and pelvis CBCT imaging showed good accuracy in calculating in-field organ doses there was less accuracy in determining out of field organ doses. This was due to the reduction in photon scoring statistics outside of the field and the discrepancy in the modelling of the heel effect.

DVHs were evaluated for six different sites using the CBCT scan protocols. The $D_{50\%}$ and $D_{10\%}$ were calculated for radiosensitive OARs. For pelvis CBCT bladder ($D_{50\%}$=18.7 mGy, $D_{10\%}$=22.4 mGy), rectum ($D_{50\%}$=17.8 mGy, $D_{10\%}$=18.7 mGy) recieved near the highest organ doses in the volume
There was a significant difference in organ doses during thorax CBCT when the isocenter was moved between the left lung, mid-lung, and right lung. When moving from midlung to the right lung the heart dose decreased significantly across the volume. This isocentre shift also caused a decrease in low dose skin sparring. Shifting between left lung and mid-lung provided no additional benefit for the heart DVH.
The intention of this component of the study was to provide treatment planning data for CBCT imaging in common treatment sites. The doses determined were given as the dose per scan and can be used to estimate the additional dose received by a radiotherapy patient from imaging

7.1 Recommendations

- Manufacturers should provide published data on x-ray tube spectra for a range of tube potentials. This would provide a more suitable benchmark for approximating the spectral distribution from an x-ray tube.
- To address the problems found when modelling the heel effect, it is recommended

that a phase space be used instead of a voxelised source input. This approach could be better used to model the spatial intensity of photons across the anode compared to the voxelised source input.

- To increase the accuracy in simulated results in the anthropomorphic phantom it is recommended segmentation is used to override the HU values of the water-equivalent plugs placed in bony anatomy. When surrounded by high Z material HU value of these plugs will increase. By assigning the correct HU the HU to material conversion will provide a more accurate dose calculation.

- To improve the tabulated dose statistics given in this study more data needs to be gathered. By repeating these scans using phantoms of varying size and gender will enable more accurate reporting for population-based dose statistics.

- As always the limitations of employing a MC model for routine CBCT dose analysis remain due to the extensive computation time. Even through the use of variance reduction techniques that greatly improve simulation efficiency, on a standard CPU simulation times are still extensive. To extend the use of CBCT dose calculations for patient-specific treatment planning the use of computing clusters and further VRT efficiencies are required. Currently GATE remains a tool for retrospective dose analysis.

References

[1] Pavel, T. *et al.* Feasibility of magnetic resonance imaging-based radiation therapy for brain tumour treatment (2017).

[2] Nunan, C. S. Multileaf collimator and compensator for radiotherapy machines (1989). US Patent 4,868,843.

[3] Hill, R., Kuncic, Z. & Baldock, C. The water equivalence of solid phantoms for low energy photon beams. *Med Phys* **37**, 4355–4363 (2010).

[4] Ma, C. M. Aapm tg-61 report on kilovoltage x-ray dosimetry: formalisms and applications. In *Proceedings of the 22nd Annual International Conference of the IEEE Engineering in Medicine and Biology Society (Cat. No.00CH37143)*, vol. 3, 2308–2312 vol.3 (2000).

[5] Sykes, J. R., Lindsay, R., Iball, G. & Thwaites, D. I. Dosimetry of cbct: methods, doses and clinical consequences. *Journal of Physics: Conference Series* **444**, 12017 (2013).

[6] Pawlowski, J. M. & Ding, G. X. An algorithm for kilovoltage x-ray dose calculations with applications in kv-cbct scans and 2d planar projected radiographs. *Physics in medicine and biology* **59**, 2041–2058 (2014).

[7] Alaei, P. & Spezi, E. Commissioning kilovoltage cone-beam ct beams in a radiation therapy treatment planning system. *Journal of applied clinical medical physics* **13**, 19–33 (2012).

[8] Wang, C. . C. The progress of radiobiological models in modern radiotherapy with emphasis on the uncertainty issue. *Mutation Research-Reviews in Mutation Research* **704**, 175–181 (2010).

[9] Niemierko, A. Radiobiological models of tissue response to radiation in treatment planning systems. *Tumori* **84**, 140 (1998).

[10] Wedenberg, M. *From cell survival to dose response: modeling biological effects in radiation therapy* (Inst för onkologi-patologi/Dept of Oncology-Pathology, 2013).

[11] Zeman, E. M., Schreiber, E. C. & Tepper, J. E. Basics of radiation therapy. In *Abeloff's Clinical Oncology*, 431–460 (Elsevier, 2020).

[12] Podgoršak, E. B. *et al. Radiation physics for medical physicists* (Springer, 2006).

[13] Hargrave, C. E. *The development of a clinical decision making framework for image guided radiotherapy.* Ph.D. thesis, Queensland University of Technology (2018).

[14] Oliver, M., Ansbacher, W. & Beckham, W. A. Comparing planning time, delivery time and plan quality for imrt, rapidarc and tomotherapy. *Journal of applied clinical medical physics* **10**, 117–131 (2009).

[15] Kalender, W. A. *Computed tomography: fundamentals, system technology, image quality, applications* (John Wiley & Sons, 2011).

[16] Wen, N. *et al.* Dose delivered from varian's cbct to patients receiving imrt for prostate cancer. *Physics in Medicine & Biology* **52**, 2267 (2007).

[17] Ding, G. X., Duggan, D. M. & Coffey, C. W. Accurate patient dosimetry of kilovoltage cone-beam ct in radiation therapy. *Medical physics* **35**, 1135–1144 (2008).

[18] Mail, N., Moseley, D., Siewerdsen, J. & Jaffray, D. The influence of bowtie filtration on cone-beam ct image quality. *Medical physics* **36**, 22–32 (2009).

[19] Mayles, P., Nahum, A. E. & Rosenwald, J.-C. *Handbook of radiotherapy physics: theory and practice* (CRC Press, 2007).

[20] Sharma, R. *et al.* Radiation dose to patients from x-ray radiographic examinations using computed radiography imaging system. *Journal of Medical Physics* **40**, 29–37 (2015).

[21] Hill, R. *et al.* Advances in kilovoltage x-ray beam dosimetry. *Physics in medicine and biology* **59**, R183 (2014).

[22] Das, I. J. & Akber, S. F. Ion recombination and polarity effect of ionization chambers in kilovoltage x-ray exposure measurements. *Medical Physics* **25**, 1751–1757 (1998).

[23] Triolo, A., Brai, M., Bartolotta, A. & Marrale, M. Glow curve analysis of tld-100h irradiated with radiation of different let: Comparison between two theoretical method. *Nuclear Inst. and Methods in Physics Research, A* **560**, 413–417 (2006).

[24] Fairchild, R. G., Mattern, P. L., Lengweiler, K. & Levy, P. W. Thermoluminescence of lif tld-100: Glow-curve kinetics. *Journal of Applied Physics* **49**, 4523–4533 (1978).

[25] Del Sol Fernández, S. *et al.* Thermoluminescent dosimeters for low dose x-ray measurements. *Applied Radiation and Isotopes* **107**, 340–345 (2016).

[26] Spezi, P., Emiliano, Downes, P., Patrick, Jarvis, M., Richard, Radu, B., Emil & Staffurth, M., John. Patient-specific three-dimensional concomitant dose from cone beam computed tomography exposure in image-guided radiotherapy. *International Journal of Radiation Oncology, Biology, Physics* **83**, 419–426 (2012).

[27] Ding, G. X. *et al.* Image guidance doses delivered during radiotherapy: Quantification, management, and reduction: Report of the aapm therapy physics committee task group 180. *Medical physics* **45**, e84–e99 (2018).

[28] Islam, M. K. *et al.* Patient dose from kilovoltage cone beam computed tomography imaging in radiation therapy. *Medical physics* **33**, 1573–1582 (2006).

[29] Palm, Å., Nilsson, E. & Herrnsdorf, L. Absorbed dose and dose rate using the varian obi 1.3 and 1.4 cbct system. *Journal of applied clinical medical physics* **11**, 229–240 (2010).

[30] Hyer, D. E. & Hintenlang, D. E. Estimation of organ doses from kilovoltage cone-beam ct imaging used during radiotherapy patient position verification. *Medical Physics* **37**, 4620–4626 (2010).

[31] Kawahara, D. *et al.* Absorbed dose and image quality of varian truebeam cbct compared with obi cbct. *Physica Medica* **32**, 1628–1633 (2016).

[32] McCollough, C. H. *et al.* Ct dose index and patient dose: they are not the same thing. *Radiology* **259**, 311 (2011).

[33] Abuhaimed, A., J Martin, C., Sankaralingam, M., J Gentle, D. & McJury, M. An assessment of the efficiency of methods for measurement of the computed tomography dose index (ctdi) for cone beam (cbct) dosimetry by monte carlo simulation. *Physics in medicine and biology* **59**, 6307–6326 (2014).

[34] Amer, A., Marchant, T., Sykes, J., Czajka, J. & Moore, C. Imaging doses from the elekta synergy x-ray cone beam ct system. *The British journal of radiology* **80**, 476 (2007).

[35] Marinello, G., Mege, J., Besse, M., Kerneur, G. & Lagrange, J. Prostate radiation therapy: in vivo measurement of the dose delivered by kv-cbct. *Cancer radiotherapie: journal de la Societe francaise de radiotherapie oncologique* **13**, 353–357 (2009).

[36] Sykes, J. R., Amer, A., Czajka, J. & Moore, C. J. A feasibility study for image guided radiotherapy using low dose, high speed, cone beam x-ray volumetric imaging. *Radiotherapy and Oncology* **77**, 45–52 (2005).

[37] Ding, G. X., Duggan, D. M. & Coffey, C. W. Characteristics of kilovoltage x-ray beams used for cone-beam computed tomography in radiation therapy. *Physics in Medicine and Biology* **52**, 1595–1615 (2007).

[38] Song, W. Y. *et al.* A dose comparison study between xvi® and obi® cbct systems. *Medical Physics* **35**, 480–486 (2008).

[39] Atun, R. *et al.* Expanding global access to radiotherapy. *The Lancet. Oncology* **16**, 1153–1186 (2015).

[40] Marchant, T. E. & Joshi, K. D. Comprehensive monte carlo study of patient doses from cone-beam ct imaging in radiotherapy. *Journal of radiological protection : official journal of the Society for Radiological Protection* **37**, 13–30 (2017).

[41] Spezi, E., Downes, P., Radu, E. & Jarvis, R. Monte carlo simulation of an x-ray volume imaging cone beam ct unit. *Medical physics* **36**, 127–136 (2009).

[42] Downes, P., Jarvis, R., Radu, E., Kawrakow, I. & Spezi, E. Monte carlo simulation and patient dosimetry for a kilovoltage cone-beam ct unit. *Medical physics* **36**, 4156–4167 (2009).

[43] Pierce, D. A. & Preston, D. L. Radiation-related cancer risks at low doses among atomic bomb survivors. *Radiation research* **154**, 178–186 (2000).

[44] Preston, D. L., Shimizu, Y., Pierce, D. A., Suyama, A. & Mabuchi, K. Studies of mortality of atomic bomb survivors. report 13: Solid cancer and noncancer disease mortality: 1950–1997. *Radiation research* **160**, 381–407 (2003).

[45] Kaderka, R. *et al.* Out-of-field dose measurements in a water phantom using different radiotherapy modalities. *Physics in Medicine & Biology* **57**, 5059 (2012).

[46] De Vathaire, F. *et al.* Role of radiotherapy and chemotherapy in the risk of second malignant neoplasms after cancer in childhood. *British journal of cancer* **59**, 792 (1989).

[47] Dracham, C. B., Shankar, A. & Madan, R. Radiation induced secondary malignancies: a review article. *Radiation oncology journal* **36**, 85 (2018).

[48] Davis, E. J., Beebe-Dimmer, J. L., Yee, C. L. & Cooney, K. A. Risk of second primary tumors in men diagnosed with prostate cancer: a population-based cohort study. *Cancer* **120**, 2735–2741 (2014).

[49] Murray, L., Henry, A., Hoskin, P., Siebert, F.-A. & Venselaar, J. Second primary cancers after radiation for prostate cancer: a review of data from planning studies. *Radiation oncology* **8**, 172 (2013).

[50] Ng, J. & Shuryak, I. Minimizing second cancer risk following radiotherapy: current perspectives. *Cancer management and research* **7**, 1 (2015).

[51] Chaturvedi, A. K. *et al.* Second cancers among 104760 survivors of cervical cancer: evaluation of long-term risk. *Journal of the National Cancer Institute* **99**, 1634–1643 (2007).

[52] Brenner, D. J., Curtis, R. E., Hall, E. J. & Ron, E. Second malignancies in prostate carcinoma patients after radiotherapy compared with surgery. *Cancer: Interdisciplinary International Journal of the American Cancer Society* **88**, 398–406 (2000).

[53] Tubiana, M., Feinendegen, L. E., Yang, C. & Kaminski, J. M. The linear no-threshold relationship is inconsistent with radiation biologic and experimental data. *Radiology* **251**, 13–22 (2009).

[54] Boda-Heggemann, J., Lohr, F., Wenz, F., Flentje, M. & Guckenberger, M. kv cone-beam ct-based igrt. *Strahlentherapie und Onkologie* **187**, 284 (2011).

[55] Commission, I. E. *et al.* Medical electrical equipment—part 2-44: particular requirements for the basic safety and essential performance of x-ray equipment for computed tomography. *International Electrotechnical Commission (IEC)* 60601–2 (2010).

[56] Downes, P., Jarvis, R., Radu, E., Kawrakow, I. & Spezi, E. Monte carlo simulation and patient dosimetry for a kilovoltage cone-beam ct unit. *Medical Physics* **36**, 4156–4167 (2009).

[57] Pyone, Y. Y., Suriyapee, S., Sanghangthum, T., Oonsiri, S. & Tawonwong, T. Determination of effective doses in image-guided radiation therapy system. *Journal of Physics: Conference Series* **694**, 12007 (2016).

[58] Hauri, P., Hälg, R. A. & Schneider, U. No increase in effective dose from half compared to full rotation pelvis cone beam ct. *Journal of applied clinical medical physics* **18**, 364–368 (2017).

[59] Jones, D. Icru report 50—prescribing, recording and reporting photon beam therapy. *Medical physics* **21**, 833–834 (1994).

[60] Owen, A. B. *Monte Carlo theory, methods and examples* (2013).

[61] Seco, J. & Verhaegen, F. *Monte Carlo techniques in radiation therapy* (CRC press, 2013).

[62] Rogers, D. Monte carlo techniques in radiotherapy. *Physics in Canada* **58**, 63–71 (2002).

[63] Verhaegen, F. & Seuntjens, J. Monte carlo modelling of external radiotherapy photon beams. *Physics in medicine & biology* **48**, R107 (2003).

[64] Péraud, J.-P. M., Landon, C. D. & Hadjiconstantinou, N. G. Monte carlo methods for solving the boltzmann transport equation. *Annual Review of Heat Transfer* **17** (2014).

[65] Kim, S. *Cone beam computed tomography (CBCT) dosimetry: measurements and Monte Carlo simulations*. Ph.D. thesis, Dissertation, Duke University (2010).

[66] Lloyd, S. A. *Evaluation of a deterministic Boltzmann solver for radiation therapy dose calculations involving high-density hip prostheses*. Ph.D. thesis (2011).

[67] Santin, G. *et al.* Gate: a geant4-based simulation platform for pet and spect integrating movement and time management. *IEEE Transactions on Nuclear Science* **50**, 1516–1521 (2003).

[68] Sarrut, D. *et al.* A review of the use and potential of the gate monte carlo simulation code for radiation therapy and dosimetry applications. *Medical Physics* **41**, 064301–n/a (2014).

[69] Baldacci, F. *et al.* A track length estimator method for dose calculations in low-energy x-ray irradiations: implementation, properties and performance. *Zeitschrift fuer Medizinische Physik* **25**, 36–47 (2015).

[70] Visvikis, D. *et al.* Use of the gate monte carlo package for dosimetry applications. *Nuclear Instruments and Methods in Physics Research Section A: Accelerators, Spectrometers, Detectors and Associated Equipment* **569**, 335–340 (2006).

[71] Sarrut, D. *et al.* A review of the use and potential of the gate monte carlo simulation code for radiation therapy and dosimetry applications. *Medical Physics* **41**, 064301–n/a (2014).

[72] Hirayama, H. Lecture note on photon interactions and cross sections. *KEK, High Energy Accelerator Research Organization, Oho, Tsukuba, Ibaraki, Japan* (2000).

[73] on Airport Passenger Screening: Backscatter X-Ray Machines, C. *et al. Airport passenger screening using backscatter X-ray machines: Compliance with standards* (2016).

[74] Kawrakow, I. & Fippel, M. Investigation of variance reduction techniques for monte carlo photon dose calculation using xvmc. *Physics in Medicine and Biology* **45**, 2163–2183 (2000).

[75] Smekens, F. *et al.* Split exponential track length estimator for monte-carlo simulations of small-animal radiation therapy. *Physics in medicine and biology* **59**, 7703–7715 (2014).

[76] Williamson, J. F. Monte carlo evaluation of kerma at a point for photon transport problems. *Medical physics* **14**, 567 (1987).

[77] Kirkup, L. & Frenkel, B. *An introduction to uncertainty in measurement using the GUM (guide to the expression of uncertainty in measurement)* (Cambridge University Press, Cambridge, 2006).

[78] Basaglia, T. *et al.* Experimental quantification of geant4 physicslist recommendations: methods and results. *Journal of Physics: Conference Series* **664**, 72037 (2015).

[79] Guatelli, S., Mantero, A., Mascialino, B., Nieminen, P. & Pia, M. G. Geant4 atomic relaxation. *IEEE Transactions on Nuclear Science* **54**, 585–593 (2007).

[80] Matsumoto, M. & Nishimura, T. Mersenne twister: a 623-dimensionally equidistributed uniform pseudo-random number generator. *ACM Transactions on Modeling and Computer Simulation (TOMACS)* **8**, 3–30 (1998).

[81] Renner, F., Wulff, J., Kapsch, R.-P. & Zink, K. Uncertainties in monte carlo-based absorbed dose calculations for an experimental benchmark. *Physics in medicine and biology* **60**, 7637–7653 (2015).

[82] Mainegra-Hing, E. & Kawrakow, I. Efficient x-ray tube simulations. *Medical physics* **33**, 2683–2690 (2006).

[83] Ubrich, F., Wulff, J., Kranzer, R. & Zink, K. Thimble ionization chambers in medium-energy x-ray beams and the role of constructive details of the central electrode: Monte carlo simulations and measurements. *Physics in Medicine & Biology* **53**, 4893 (2008).

[84] Gershkevitsh, E. & Zolotuhhin, D. Su-f-j-16: Planar kv imaging dose reduction study. *Medical Physics* **43**, 3409–3409 (2016).

[85] Yuan, J. *et al.* Experimental validation of monte carlo simulations based on a virtual source model for tomotherapy in a rando phantom. *International Journal of Radiation Oncology, Biology, Physics* **93**, E608–E608 (2015).

[86] Schneider, W., Bortfeld, T. & Schlegel, W. Correlation between ct numbers and tissue parameters needed for monte carlo simulations of clinical dose distributions. *Physics in Medicine and Biology* **45**, 459–478 (2000).

[87] Abolaban, F. A. *On board cone beam ct for treatment planning in image guided radiotherapy.* Ph.D. thesis (2011).

[88] Hyer, D. E., Serago, C. F., Kim, S., Li, J. G. & Hintenlang, D. E. An organ and effective dose study of xvi and obi cone-beam ct systems. *Journal of Applied Clinical Medical Physics* **11**, 181–197 (2010).

[89] Mail, N. *et al.* A methodology for on-board cbct imaging dose using optically stimulated luminescence detectors. *Journal of Applied Clinical Medical Physics* **17**, 1–18 (2016).

[90] Haworth, A. *et al.* Comparison of tld calibration methods for 192ir dosimetry. *Journal of applied clinical medical physics* **14**, 258–272 (2013).

[91] Valentin, J. Basic anatomical and physiological data for use in radiological protection: reference values: Icrp publication 89. *Annals of the ICRP* **32**, 1–277 (2002).

[92] Martin, C. J. Effective dose: how should it be applied to medical exposures? *The British journal of radiology* **80**, 639 (2007).

[93] Uselmann, A. J. & Thomadsen, B. R. On effective dose for radiotherapy based on doses to nontarget organs and tissues: On effective dose for radiotherapy. *Medical Physics* **42**, 977–982 (2015).

[94] Ding, G. X., Munro, P., Pawlowski, J., Malcolm, A. & Coffey, C. W. Reducing radiation exposure to patients from kv-cbct imaging. *Radiotherapy and Oncology* **97**, 585–592 (2010).

Appendices

A Reference Dosimetry

A.1 AAPM TG-61 absorbed dose to water at 2 cm depth

The following worksheets are based on a worksheet given by: The American Association of Physicists in Medicine (AAPM) Task Group 61 (TG-61). Measurements were performed on 3 separate occasions against TLD-100s. The beam qualities examined were 100 kV, 7.4 mm Al and 125 kV, 8.0 mm Al. Recombination effects were less than 0.1%. They were decidely negligible and not considered in the calculation. Polarity correction is not applicable for the local reference chamber when the calibration polarity is used (-300 V).[22]

A.1.1 100 kV beam

C.2. TG-61 Worksheet: Calcaulating dose to water at 2 cm depth in water

Name: Luke Gilling **Date:** 21/02/2018

(1) **X-ray unit:** Truebeam XI, **Tube potential:** 100 kV, **HVL:** 7.4 mm Al, **SSD:** 100 cm, **Field size:** 10 x 10 cm^2

(2) **Ion chamber and electrometer calibration. Date of last calibration:** 2018

Ion chamber: IBA FC65-G SN:3681, **Calibration factor** N_k**:**=45.02 mGy/nC **Electrometer:** Fluke Biomedical Advanced Therapy Dosimeter, Model 35040, **Calibration factor** P_{elec}**:** 1 C/scale unit

(3) **Chamber signal:** = 1.02 nC

(4) **Temperature T** = 22.9 °C, **Pressure P** = 100.0 kPa

$P_{TP} = \frac{273.2+T[°C]}{295.2} \times \frac{101.33}{P[kPa]} = 1.02$

(5) **Total radiation exposure:** 1000 mAs

(6) **Recombination correction** = NA

(7) **Polarity correction** = NA

(8) **Corrected chamber reading** $M = M_{raw}P_{elec}P_{TP}P_{ion}P_{pol} = 1.05$ nC

(9) **Chamber correction factor (Table VIII, Fig. 4, Table IX):**

$$P_{Q,cham}P_{sheath} = 1.016$$

(10) **Conversion factor (TableVII, Fig. 3)**

$$\left[\left(\frac{\overline{\mu_{en}}}{\rho}\right)^{w}_{air}\right]_{water} = 1.039$$

(11) **Dose to water:**

$$D_w = M_{pl}N_kP_{Q,chamber}P_{sheath}\left[\left(\frac{\overline{\mu_{en}}}{\rho}\right)^{w}_{air}\right]_{water} = 49.74mGy$$

$\underline{= 50\ \mu\text{Gy/mAs}}$

A.1.2 125 kV beam

C.2. TG-61 Worksheet: Calcaulating dose to water at 2 cm depth in water

Name: Luke Gilling **Date:** 25/02/2018

(1) **X-ray unit:** Truebeam XI, **Tube potential:** 125 kV, **HVL:** 8.0 mm Al, **SSD:** 100 cm, **Field size:** 10 x 10 cm^2

(2) **Ion chamber and electrometer calibration. Date of last calibration:** 2018

Ion chamber: IBA FC65-G SN:3681, **Calibration factor** N_k**:**=44.95 mGy/nC **Electrometer:** Fluke Biomedical Advanced Therapy Dosimeter, Model 35040, **Calibration factor** P_{elec}**:** 1 C/scale unit

(3) **Chamber signal:** = 1.83 nC

(4) **Temperature T** = 23.4 °C, **Pressure P** = 100.0 kPa

$P_{TP} = \frac{273.2+T[^\circ C]}{295.2} \times \frac{101.33}{P[kPa]} = 1.03$

(5) **Total radiation exposure:** 1000 mAs

(6) **Recombination correction** = NA

(7) **Polarity correction** = NA

(8) **Corrected chamber reading** $M = M_{raw}P_{elec}P_{TP}P_{ion}P_{pol} = 1.88$ nC

(9) **Chamber correction factor (Table VIII, Fig. 4, Table IX):**

$$P_{Q,cham}P_{sheath} = 1.017$$

(10) **Conversion factor (TableVII, Fig. 3)**

$$\left[\left(\frac{\overline{\mu_{en}}}{\rho}\right)^{w}_{air}\right]_{water} = 1.045$$

(11) **Dose to water:**

$$D_w = M_{pl}N_kP_{Q,chamber}P_{sheath}\left[\left(\frac{\overline{\mu_{en}}}{\rho}\right)^{w}_{air}\right]_{water} = 89.68mGy$$

$\underline{= 90\ \mu\text{Gy/mAs}}$

B Uncertainties in experimental measurement

B.1 Relative dosimetry

B.1.1 PDD and profile measurements

Table B.1: The combined uncertainty in relative dosimetry measurements taken using the CC13 scanning thimble chamber[3]

Type of quantity or procedure	Uncertainty (%)
Repeatability of measurement	1.6
Central axis positioning	0.4
SSD and depth accuracy	0.2
Dose rate variations in x-ray output	2.8
Measurement equipment drift	0.3
Mass attenuation variation with depth	1.0
Combined uncertainty	2.7
Expanded uncertainty (k=2)	5.3

B.2 Absolute dosimetry

B.2.1 AAPM TG-61

Table B.2: The combined uncertainty present when using the AAPM TG-61 reference dosimetry protocol[4]

Type of quantity or procedure	Uncertainty (%)
Repeatability of measurement	0.2
N_k from standards laboratory	2.1
Chamber correction factor $P_{Q,cham}$	1.5
Chamber waterproofing sheath correction factor P_{sheath}	0.5
$[(\overline{\mu_{en}}/\rho)^{w}_{air}]_{air}$	1.5
Effect of beam quality difference between calibration and measurement	3.0
In-water measurement in the user's beam	2.0
Combined uncertainty	4.7
Expanded uncertainty (k=2)	9.4

C TLD calibration

The calibration work for the TLDs was performed for both 100 kV and 125 kV beams. TLD-100s were used to conduct the experiment. Sensitivty correction factors were calculated for each energy. The TLDs were then cross-calibrated with dose measured from an ion chamber using the AAPM TG61 reference protocol. The TLDs were then placed in the head and pelvis sections of the RANDO phantom from dose measurement. A summary of the work is seen below

Figure C.1: Sensitivity correction factors

01/02/2018 TLD-100 sensitivity correction factors (SCF)

SSD	100cm
Blade Field Size	50 x 50cm^2
Unit used	TrueBeam XI
Source configuration	Ti filter, no bowtie filter
mA	225
ms	4200
mAs	1000

		Wednesday, 7 February 2018		Thursday, 8 February 2018		Friday, 9 February 2018		Sunday, 18 February 2018		mean		SCF	SCF	Rel SD
	TLD	Reading (nC)	SCF	Reading (nC)	SCF	Reading (nC)	SCF	Reading (nC)	SCF	Reading (nC)		Mean	STDEV	(STDEV/Mean)
100kV	H1	417.8	**1.01**	412.9	**1.01**	428.9	**1.00**	419.8	**1.00**	419.8	**1.00**	**1.00**	0.006	0.60%
	H2	416.8	**1.01**	423.1	**0.99**	427.1	**1.00**	425.4	**0.99**	423.1	**1.00**	**1.00**	0.009	0.93%
	H3	411.2	**1.02**	410.6	**1.02**	416.6	**1.02**	422.3	**1.00**	415.2	**1.02**	**1.02**	0.011	1.09%
	H4	405.5	**1.04**	395.3	**1.06**	405.1	**1.05**	396.5	**1.06**	400.6	**1.05**	**1.05**	0.009	0.82%
	H5	410.9	**1.03**	416.7	**1.00**	421.3	**1.01**	418.1	**1.01**	416.8	**1.01**	**1.01**	0.009	0.85%
	H6	431.8	**0.98**	427.7	**0.98**	451.0	**0.95**	424.8	**0.99**	433.8	**0.97**	**0.97**	0.016	1.68%
	H7	418.4	**1.01**	422.1	**0.99**	439.7	**0.97**	423.2	**1.00**	425.9	**0.99**	**0.99**	0.013	1.32%
	H8	417.9	**1.01**	425.0	**0.98**	426.8	**1.00**	423.9	**0.99**	423.4	**1.00**	**1.00**	0.009	0.93%
	H9	418.9	**1.01**	417.7	**1.00**	423.8	**1.01**	425.3	**0.99**	421.4	**1.00**	**1.00**	0.007	0.65%
	H10	436.0	**0.97**	424.5	**0.98**	436.0	**0.98**	435.1	**0.97**	432.9	**0.97**	**0.97**	0.007	0.75%
	H11	430.1	**0.98**			419.9	**1.02**	425.9	**0.99**	425.3	**0.99**	**0.99**	0.016	1.59%
	H12	434.9	**0.97**	423.5	**0.99**	427.9	**1.00**	421.1	**1.00**	426.8	**0.99**	**0.99**	0.012	1.26%
	H13	426.2	**0.99**	411.0	**1.02**	424.9	**1.00**	415.0	**1.02**	419.3	**1.01**	**1.01**	0.011	1.10%
		421.3		417.5		426.9		421.3		421.9				
125kV	H14	708.7	**1.00**	721.9	**1.00**	709.0	**1.03**	700.9	**1.02**	710.1	**1.01**	**1.01**	0.012	1.18%
	H15	708.8	**1.00**	723.9	**1.00**	729.1	**1.00**	702.2	**1.01**	716.0	**1.00**	**1.00**	0.006	0.65%
	H16	721.4	**0.98**	740.5	**0.98**	740.7	**0.98**	725.6	**0.98**	732.1	**0.98**	**0.98**	0.003	0.34%
	H17	707.5	**1.00**	718.1	**1.01**	745.7	**0.98**	706.4	**1.01**	719.4	**1.00**	**1.00**	0.012	1.20%
	H18	735.4	**0.96**	772.1	**0.94**	779.3	**0.94**	749.0	**0.95**	758.9	**0.95**	**0.95**	0.012	1.22%
	H19	707.7	**1.00**	714.0	**1.01**	727.6	**1.00**	724.4	**0.98**	718.4	**1.00**	**1.00**	0.010	1.05%
	H20	684.9	**1.03**	701.2	**1.03**	703.3	**1.04**	684.8	**1.04**	693.6	**1.04**	**1.04**	0.004	0.34%
	H21	711.6	**1.00**	728.5	**0.99**	742.7	**0.98**	731.3	**0.97**	728.5	**0.99**	**0.99**	0.009	0.86%
	H22	697.2	**1.02**	704.3	**1.03**	709.6	**1.03**	695.5	**1.02**	701.7	**1.02**	**1.02**	0.004	0.43%
	H23	679.3	**1.04**	732.0	**0.99**	729.8	**1.00**	718.9	**0.99**	715.0	**1.00**	**1.00**	0.022	2.23%
	H24	713.0	**0.99**	716.1	**1.01**	724.9	**1.01**	708.0	**1.01**	715.5	**1.00**	**1.00**	0.006	0.58%
	H25	696.8	**1.02**	701.5	**1.03**	706.1	**1.03**	693.1	**1.03**	699.3	**1.03**	**1.03**	0.006	0.60%
	H26	736.5	**0.96**	716.2	**1.01**	733.4	**0.99**	715.6	**0.99**	725.4	**0.99**	**0.99**	0.017	1.74%
		708.4		722.3		729.3		712.0		718.0				

Figure C.2: TLD calibration factors

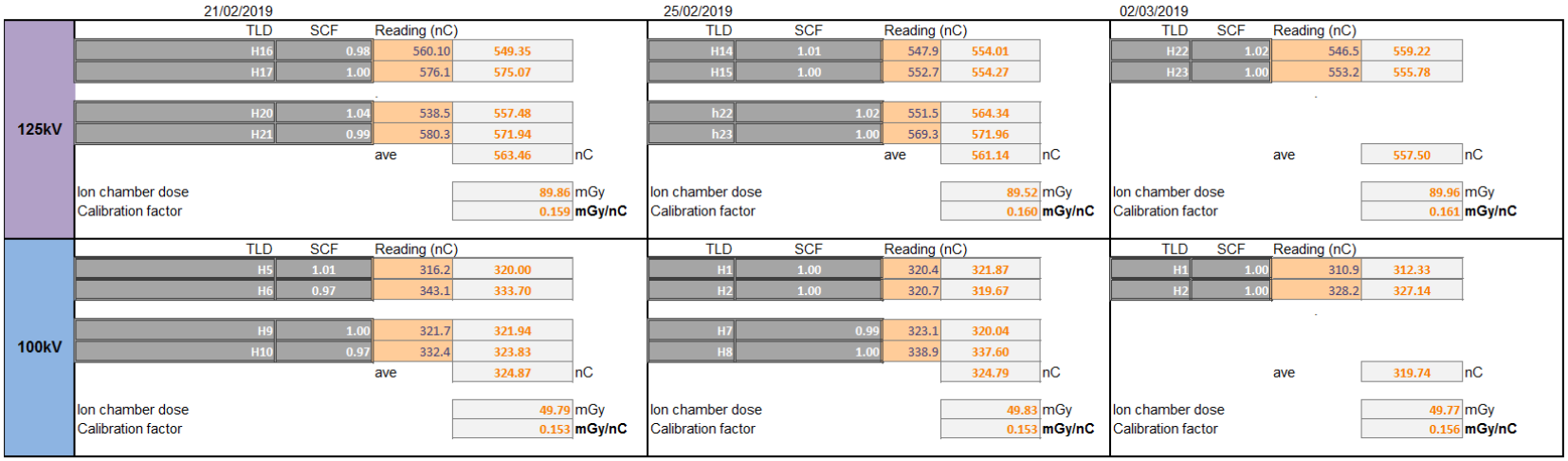

21/02/2019						25/02/2019						02/03/2019					
	TLD	SCF	Reading (nC)				TLD	SCF	Reading (nC)				TLD	SCF	Reading (nC)		
125kV	H16	0.98	560.10	549.35		125kV	H14	1.01	547.9	554.01		125kV	H22	1.02	546.5	559.22	
	H17	1.00	576.1	575.07			H15	1.00	552.7	554.27			H23	1.00	553.2	555.78	
	H20	1.04	538.5	557.48			h22	1.02	551.5	564.34							
	H21	0.99	580.3	571.94			h23	1.00	569.3	571.96							
			ave	563.46	nC				ave	561.14	nC				ave	557.50	nC
	Ion chamber dose			89.86	mGy		Ion chamber dose			89.52	mGy		Ion chamber dose			89.96	mGy
	Calibration factor			0.159	**mGy/nC**		Calibration factor			0.160	**mGy/nC**		Calibration factor			0.161	**mGy/nC**
	TLD	SCF	Reading (nC)				TLD	SCF	Reading (nC)				TLD	SCF	Reading (nC)		
100kV	H5	1.01	316.2	320.00		100kV	H1	1.00	320.4	321.87		100kV	H1	1.00	310.9	312.33	
	H6	0.97	343.1	333.70			H2	1.00	320.7	319.67			H2	1.00	328.2	327.14	
	H9	1.00	321.7	321.94			H7	0.99	323.1	320.04							
	H10	0.97	332.4	323.83			H8	1.00	338.9	337.60							
			ave	324.87	nC					324.79	nC				ave	319.74	nC
	Ion chamber dose			49.79	mGy		Ion chamber dose			49.83	mGy		Ion chamber dose			49.77	mGy
	Calibration factor			0.153	**mGy/nC**		Calibration factor			0.153	**mGy/nC**		Calibration factor			0.156	**mGy/nC**

Cal. Factor

kV	mGy/nC
100	0.1541
125	0.1601

Figure C.3: Summary of TLD dose measurements performed in the RANDO pelvis phantom

	Position	TLD	Mean dose (mGy)	STD DEV	rel SD
125kV	Right femoral head	H16			
		H17	15.2	0.7	4.9%
	Left Ischial Spine	H18			
		H19	17.5	0.8	4.6%
	Left femoral head	H20			
		H21	19.8	0.4	1.9%
	Right femoral artery	H22			
		H23	24.7	0.4	1.5%
	Sacrum	H24			
		H25	25.4	0.5	1.8%
	CENTRE	H14			
		H15	25.3	0.4	1.5%

Figure C.4: Summary of TLD dose measurements performed in the RANDO head phantom

	Position	TLD	Mean dose (mGy)	STD DEV	rel SD
100kV	Superior	H16			
		H17	3.1	0.1	3.2%
	Inferior	H18			
		H19	3.1	0.1	4.6%
	Right	H20			
		H21	2.8	0.1	2.1%
	Left	H22			
		H23	3.2	0.1	3.6%

D MC dose conversion factors

Figure D.1: 100 kVp, 7.4 mm Al MC calibration factor

	Position	Dexp (mGy)	Dexp (mGy/mAs)	DMC (Gy)	DMC (mGy/photon)	f (photons/mAs)
sup	H1	3.1	0.0206	1.53E-09	7.65E-14	2.70E+11
inf	H2	3.1	0.0210	1.89E-09	9.45E-14	2.22E+11
left	H3	2.8	0.0184	1.55E-09	7.75E-14	2.38E+11
right	H4	3.2	0.0210	1.65E-09	8.25E-14	2.55E+11
					mean	2.46E+11
					SD	2.06E+10
					rel SD	8.4%

Figure D.2: 125 kVp, 8.0 mm Al MC calibration factor

	Position	Dexp (mGy)	Dexp (mGy/mAs)	DMC (Gy)	DMC (mGy/photon)	f (photons/mAs)
Right femoral head	P1	15.2	0.0142	1.06E-09	5.32E-14	~~2.66E+11~~
Left Ischial Spine	P2	17.5	0.0163	7.20E-10	3.60E-14	4.52E+11
Left femoral head	P3	19.8	0.0184	9.14E-10	4.57E-14	4.03E+11
Right femoral artery	P4	24.7	0.0230	1.09E-09	5.43E-14	4.23E+11
Sacral bone	P5	25.4	0.0236	1.08E-09	5.41E-14	4.37E+11
Centre	P6	25.3	0.0236	8.94E-10	4.47E-14	~~5.27E+11~~
					mean	4.29E+11
					SD	2.12E+10
					rel SD	4.9%

E GATE macros

E.1 Main macro

main.mac

```
#------------------------timeslice-------------------------------------


# for static acquisitions
#/control/alias TIMESLICE "1 s"
#/control/alias TIMESTART "0.0 s"
#/control/alias TIMESTOP "1 s"
```

```
# for full rotation
/control/alias TIMESLICE "0.0372916667 s"
/control/alias TIMESTART "0.0 s"
/control/alias TIMESTOP "13.425 s"

# for 200 deg rotation
#/control/alias TIMESLICE "0.04097985 s"
#/control/alias TIMESTART "0.0 s"
#/control/alias TIMESTOP "7.458 s"



#-------------------------rotation---------------------------------------
/control/alias ROTATE "full_rotation.mac"
#/control/alias ROTATE "200_rotation.mac"
#/control/alias ROTATE "static.mac"

#-------------------------source angle-----------------------------------
#/control/alias THETA "10. deg"
/control/alias THETA "14. deg"

#-------------------------source-----------------------------------------
#/control/alias SOURCE "100kV.txt"
/control/alias SOURCE "125kV.txt"

#-------------------------blades-----------------------------------------
#/control/alias BLADES "blades_full_fan.mac"
/control/alias BLADES "blades_half_fan.mac"

#-------------------------fan--------------------------------------------
#/control/alias FAN "full_fan.mac"
```

```
/control/alias FAN "half_fan.mac"
#/control/alias FAN "no_fan.mac"

#------------------------phantom---------------------------------
/control/alias PHANTOM "randoPelvis.mac"
#/control/alias PHANTOM "randoHead.mac"

#------------------------actors----------------------------------
#/control/alias ANTHRO "anthro/randoPelvis.mac"
#/control/alias ANTHRO "anthro/randoHead.mac"
/control/alias ANTHRO "anthro/ICRP_setle.mac"

#------------------------primaries-------------------------------
#/control/alias PRIMARIES "1"
/control/alias PRIMARIES "1e7"
#/control/alias PRIMARIES "2e9"
#/control/alias PRIMARIES "5e8"
#/control/alias PRIMARIES "1e9"
#=====================================================
# VISUALISATION
#=====================================================
#/control/execute  visu.mac

#=====================================================
# WORLD
#=====================================================
/control/execute  geometry.mac

#=====================================================
# PHANTOM
#=====================================================
```

```
/control/execute phantom/{PHANTOM}

#=====================================================
# ROTATION
#=====================================================
/control/execute rotation/{ROTATE}

#=====================================================
# PHYSICS
#=====================================================

/gate/physics/addPhysicsList emlivermore
/gate/physics/addAtomDeexcitation

#=====================================================
# Additional processes
#=====================================================

/gate/physics/processList Enabled
/gate/physics/processList Initialized

#=====================================================
# OUTPUT ACTORS
#=====================================================

/control/execute actors/{ANTHRO}

/gate/actor/addActor SimulationStatisticActor stat
/gate/actor/stat/save output/stat.txt

#=====================================================
```

```
# VERBOSITY
#=====================================================

/control/execute verbose.mac

#=====================================================
# INITIALIZE
#=====================================================

/gate/run/initialize

#=====================================================
# SOURCE
#=====================================================
/control/execute source.mac

#=====================================================#
# START
#=====================================================

/gate/random/setEngineName MersenneTwister
/gate/random/setEngineSeed auto

/gate/application/setTimeSlice {TIMESLICE}
/gate/application/setTimeStart {TIMESTART}
/gate/application/setTimeStop {TIMESTOP}

/gate/application/setTotalNumberOfPrimaries {PRIMARIES}
/gate/application/start
```

E.2 Geometry

geometry.mac

```
/gate/geometry/setMaterialDatabase GateMaterials.db

/gate/world/geometry/setXLength 2. m
/gate/world/geometry/setYLength 2. m
/gate/world/geometry/setZLength 3.2 m
/gate/world/setMaterial Air
/gate/world/vis/forceWireframe

#--------------------------------------------------------------------------------
#kVs: head configuration
#--------------------------------------------------------------------------------


  /gate/world/daughters/name kVsBox
  /gate/world/daughters/insert box
  /gate/kVsBox/setMaterial Air
  #x length defines distance from source to polycarbonate window
  /gate/kVsBox/geometry/setXLength 300 mm
  /gate/kVsBox/geometry/setYLength 300 mm
  /gate/kVsBox/geometry/setZLength 500 mm
  /gate/kVsBox/placement/setTranslation 0 0 -123 cm

  /gate/kVsBox/vis/forceWireframe
  /gate/kVsBox/vis/setVisible 1
  /gate/kVsBox/vis/setColor magenta

  #--------------------------------------------------------------------
  #STARTING AT SOURCE AND MOVING DOWNSTREAM
```

```
#------------------------------------------------------------------------
/gate/kVsBox/daughters/name airSource
/gate/kVsBox/daughters/insert cylinder
/gate/airSource/setMaterial Air
/gate/airSource/geometry/setRmin  0 mm
/gate/airSource/geometry/setRmax   10.0 mm
/gate/airSource/geometry/setHeight  10.0 mm
/gate/airSource/placement/setTranslation 0 0 0 mm

#blades
/control/execute blades/{BLADES}

#Beam hardening filter
/gate/kVsBox/daughters/name TiFilter
/gate/kVsBox/daughters/insert box
/gate/TiFilter/setMaterial Titanium
/gate/TiFilter/geometry/setXLength 140 mm
/gate/TiFilter/geometry/setYLength 140 mm
/gate/TiFilter/geometry/setZLength .89 mm
/gate/TiFilter/placement/setTranslation 0 0 132.645 mm
/gate/TiFilter/vis/forceSolid

#Bowtie
/control/execute bowtie-filters/{FAN}

#PC cover
/gate/kVsBox/daughters/name detectCover
/gate/kVsBox/daughters/insert box
/gate/detectCover/setMaterial Polycarbonate
/gate/detectCover/geometry/setXLength 302 mm
/gate/detectCover/geometry/setYLength 302 mm
```

```
  /gate/detectCover/geometry/setZLength 2 mm
  /gate/detectCover/placement/setTranslation 0 0 225 mm
  /gate/detectCover/vis/forceSolid
  /gate/detectCover/vis/setColor yellow

/gate/world/daughters/name killActor
/gate/world/daughters/insert box
/gate/killActor/setMaterial Air
/gate/killActor/geometry/setXLength 2. m
/gate/killActor/geometry/setYLength 2. m
/gate/killActor/geometry/setZLength 10 cm
/gate/killActor/placement/setTranslation 0 0 90 cm

/gate/actor/addActor KillActor myKill
/gate/actor/myKill/save output/kill.txt
/gate/actor/myKill/attachTo killActor
```

E.3 Phantom

icrpPhantom.mac

```
#=====================================
# ICRP ROTATION VOLUME
#=====================================
/gate/world/daughters/name                rot_vol
/gate/world/daughters/insert              box
/gate/rot_vol/setMaterial Air
/gate/rot_vol/geometry/setXLength 80 cm
/gate/rot_vol/geometry/setYLength 80 cm
```

```
/gate/rot_vol/geometry/setZLength 80 cm

/gate/rot_vol/placement/setRotationAxis 1 0 0
/gate/rot_vol/placement/setRotationAngle 90 deg
/gate/rot_vol/placement/setTranslation 0 0 0 cm

/gate/rot_vol/vis/setColor red

#=====================================
# ICRP IMAGE SET
#=====================================
/gate/rot_vol/daughters/name                 icrp_phantom
/gate/rot_vol/daughters/insert               ImageNestedParametrisedVolume

#pelvis image measures 241.18x241.18x256 mm
/gate/icrp_phantom/geometry/setImage data/icrp.hdr
#/gate/icrp_phantom/placement/setOrigin -0.1 0 0 mm

/gate/icrp_phantom/geometry/setHUToMaterialFile phantom/icrp_dat2mat.txt
/gate/icrp_phantom/placement/setRotationAxis -1 0 0
/gate/icrp_phantom/placement/setRotationAngle 90 deg

/gate/icrp_phantom/vis/setColor cyan
```

E.4 Source

source.mac

```
/gate/source/addSource mySource gps
/gate/source/mySource/gps/particle gamma
```

```
#SPECTRUM
/gate/source/mySource/gps/energytype UserSpectrum
/gate/source/mySource/gps/setSpectrumFile {SOURCE} #125kV.txt or 100kV.txt

/gate/source/mySource/attachTo   airSource
/gate/source/mySource/gps/position  0 0 0 mm
/gate/source/mySource/gps/pos/type  Plane
/gate/source/mySource/gps/shape     Rectangle
/gate/source/mySource/gps/halfx     0.75 mm
/gate/source/mySource/gps/halfy      0.9 mm
/gate/source/mySource/gps/ang/type  iso
/gate/source/mySource/gps/mintheta 0. deg
/gate/source/mySource/gps/maxtheta {THETA}
/gate/source/mySource/gps/minphi 0. deg
/gate/source/mySource/gps/maxphi 360. deg
```

E.5 Collimators

bladesBodyScan.mac

```
#upper blades
/gate/kVsBox/daughters/name           upperBlades
/gate/kVsBox/daughters/insert         box
/gate/upperBlades/setMaterial            Lead
/gate/upperBlades/geometry/setXLength    300 mm
/gate/upperBlades/geometry/setYLength    300 mm
/gate/upperBlades/geometry/setZLength    3 mm
/gate/upperBlades/placement/setTranslation  0 0 92.4 mm
/gate/upperBlades/vis/setVisible         1
```

```
/gate/upperBlades/vis/forceWireframe
/gate/upperBlades/vis/setColor          blue

   #upper window
   /gate/upperBlades/daughters/name  upperApeture
   /gate/upperBlades/daughters/insert  box
   /gate/upperApeture/setMaterial          Air
   /gate/upperApeture/geometry/setXLength   300 mm
   /gate/upperApeture/geometry/setYLength   20 mm
   /gate/upperApeture/geometry/setZLength  3 mm
   /gate/upperApeture/placement/setTranslation  0 0 0 mm
   /gate/upperApeture/vis/setVisible       1
   /gate/upperApeture/vis/setColor         red

#lower blades
/gate/kVsBox/daughters/name          lowerBlades
/gate/kVsBox/daughters/insert        box
/gate/lowerBlades/setMaterial           Lead
/gate/lowerBlades/geometry/setXLength    300 mm
/gate/lowerBlades/geometry/setYLength    300 mm
/gate/lowerBlades/geometry/setZLength    3 mm
/gate/lowerBlades/placement/setTranslation  0 0 108.4 mm
/gate/lowerBlades/vis/setVisible        1
/gate/lowerBlades/vis/forceWireframe
/gate/lowerBlades/vis/setColor          blue

   # lower window
   /gate/lowerBlades/daughters/name  lowerApeture
   /gate/lowerBlades/daughters/insert  box
   /gate/lowerApeture/setMaterial     Air
   /gate/lowerApeture/geometry/setXLength   30.573 mm
```

```
/gate/lowerApeture/geometry/setYLength   300 mm
/gate/lowerApeture/geometry/setZLength   3 mm
/gate/lowerApeture/placement/setTranslation  0 0 0 mm
/gate/lowerApeture/vis/setVisible        1
/gate/lowerApeture/vis/setColor          red
```

E.6 Bowtie filter

halfBowtie.mac

```
# ------------------------------------------------
# half bowtie : 90 trapezoids
# ------------------------------------------------

/gate/kVsBox/daughters/name   btfRotation
/gate/kVsBox/daughters/insert    box
/gate/btfRotation/setMaterial          Air
/gate/btfRotation/geometry/setXLength  141 mm
/gate/btfRotation/geometry/setYLength  141 mm
/gate/btfRotation/geometry/setZLength  31 mm
/gate/btfRotation/placement/setRotationAxis 0 0 1
/gate/btfRotation/placement/setRotationAngle -90 deg
/gate/btfRotation/placement/setTranslation 0 0 162 mm
/gate/btfRotation/vis/setColor         gray
/gate/btfRotation/vis/setVisible       1

/gate/btfRotation/daughters/name           tb_btf
/gate/btfRotation/daughters/insert    box
/gate/tb_btf/setMaterial          Air
/gate/tb_btf/geometry/setXLength  30 mm
/gate/tb_btf/geometry/setYLength  140 mm
```

```
/gate/tb_btf/geometry/setZLength  140 mm
/gate/tb_btf/placement/alignToX
/gate/tb_btf/placement/setTranslation 0 .35 0 mm
/gate/tb_btf/vis/setColor         gray
/gate/tb_btf/vis/setVisible       1



/gate/tb_btf/daughters/name w1
/gate/tb_btf/daughters/insert wedge
/gate/w1/geometry/setXLength 25.952887 mm
/gate/w1/geometry/setNarrowerXLength 25.92 mm
/gate/w1/geometry/setYLength 1.00 mm
/gate/w1/geometry/setZLength 140.000 mm
/gate/w1/placement/setRotationAxis 0 0 1
/gate/w1/placement/setRotationAngle 180 deg
/gate/w1/placement/setTranslation 2.03177825 -69.5 0 mm
/gate/w1/setMaterial AC110
/gate/w1/vis/setColor magenta
/gate/w1/vis/forceSolid

/gate/TB_btf/daughters/name w2
/gate/TB_btf/daughters/insert wedge
/gate/w2/geometry/setXLength 25.985773 mm
/gate/w2/geometry/setNarrowerXLength 25.952887 mm
/gate/w2/geometry/setYLength 1.00 mm
/gate/w2/geometry/setZLength 140.000 mm
/gate/w2/placement/setRotationAxis 0 0 1
/gate/w2/placement/setRotationAngle 180 deg
/gate/w2/placement/setTranslation 2.015335 -68.5 0 mm
/gate/w2/setMaterial AC110
```

```
/gate/w2/vis/setColor magenta
/gate/w2/vis/forceSolid

.
.
.

/gate/TB_btf/daughters/name w90
/gate/TB_btf/daughters/insert wedge
/gate/w90/geometry/setXLength 25.943149 mm
/gate/w90/geometry/setNarrowerXLength 25.923417 mm
/gate/w90/geometry/setYLength 1.00 mm
/gate/w90/geometry/setZLength 140.000 mm
/gate/w90/placement/setRotationAxis 0 1 0
/gate/w90/placement/setRotationAngle 180 deg
/gate/w90/placement/setTranslation 2.0333585 69.5 0 mm
/gate/w90/setMaterial AC110
/gate/w90/vis/setColor magenta
/gate/w90/vis/forceSolid
```

Phantom/patient

rando.mac

```
#=====================================
# RANDO PHANTOM VOLUME
#=====================================
/gate/world/daughters/name                 phantom
/gate/world/daughters/insert               box
/gate/phantom/setMaterial Air
/gate/phantom/geometry/setXLength 80 cm  # make phantom volume extra big to
    allow for any translation
```

```
/gate/phantom/geometry/setYLength 80 cm
/gate/phantom/geometry/setZLength 80 cm

/gate/phantom/placement/setRotationAxis 1 0 0
/gate/phantom/placement/setRotationAngle 90 deg
/gate/phantom/placement/setTranslation 0 0 0 cm

/gate/phantom/vis/setColor red

#=====================================
# RANDO pelvis phantom
#=====================================
/gate/phantom/daughters/name                 rando
/gate/phantom/daughters/insert               ImageNestedParametrisedVolume

#pelvis image measures 241.18x241.18x256 mm
/gate/rando/geometry/setImage  data/mhd/randopelvis/randoPelvis.mhd
#/gate/rando/placement/setOrigin -0.1 0 0 mm

/gate/rando/geometry/setHUToMaterialFile  phantom/rando_dat2mat.txt
/gate/rando/placement/setRotationAxis -1 0 0
/gate/rando/placement/setRotationAngle 90 deg

/gate/rando/vis/setColor cyan
```

E.7 Dose actors

ICRPsetle.mac

```
#=====================================================
# Dose actor - matches icrp image set
```

```
#=========================================================
/gate/actor/addActor SETLEDoseActor dosegrid
/gate/actor/dosegrid/attachTo      icrp_phantom
/gate/actor/dosegrid/stepHitType         random
/gate/actor/dosegrid/setPosition  0 0 0 cm
/gate/actor/dosegrid/setSize           38.656 38.656 24.2 cm
/gate/actor/dosegrid/setVoxelSize  0.151 0.151 0.4 cm

/gate/actor/dosegrid/enableHybridino           true
/gate/actor/dosegrid/setPrimaryMultiplicity    200
/gate/actor/dosegrid/setSecondaryMultiplicity  400
/gate/actor/dosegrid/enableDose        true
/gate/actor/dosegrid/enableUncertaintyDose true
/gate/actor/dosegrid/save output/rando/icrpDoseGrid.mhd
/gate/actor/dosegrid/saveEveryNSeconds 300
```

F Additional data

Figure F.1: Simulated and experimental results for profiles at 1 cm and 5 cm using the body scan protocol. Not included in the body of the report due to noise in the experimental data